An ARGO and XBT observing system for the Atlantic Meridional Overturning Circulation and Meridional Heat Transport (AXMOC) at 22.5ºS

Ivenis Pita[1], Marlos Pereira Goes[2], Denis L. Volkov[3], Shenfu Dong[4], Gustavo J. Goni[4], and Mauro Cirano[5]

[1]Rosenstiel School, University of Miami
[2]University of Miami/CIMAS and NOAA/AOML
[3]University of Miami / AOML
[4]NOAA/AOML
[5]Universidade Federal do Rio de Janeiro

June 1, 2023

Abstract

Changes in the Atlantic Meridional Overturning Circulation (AMOC) and associated Meridional Heat Transport (MHT) can affect climate and weather patterns, regional sea levels, and ecosystems. However, despite its importance, direct observations of the AMOC are still limited spatially and temporally, particularly in the South Atlantic. The main goal of this study is to implement a cost-effective trans-basin section to estimate for the first time the AMOC at 22.5°S, using only sustained ocean observations. For this, an optimal mapping method that minimizes the difference between surface in-situ dynamic height and satellite altimetry was developed to retrieve monthly temperature and salinity profiles from Argo and XBT data along the 22.5°S section. The mean AMOC and MHT for 22.5°S were estimated as 15.55±2.81 Sv and 0.68±0.18 PW, respectively, and are stronger during austral fall/winter and weaker in spring. The high-resolution XBT data available at the western boundary are vital for capturing the highly variable Brazil Current, and our section shows a significant improvement when compared to Argo database. The mean values, interannual and seasonal time series of AMOC and MHT were compared with other products. At 22.5S the North Atlantic Deep Water is divided into two cores that flow along both western and eastern boundaries near 2500 m depth. Our results suggest a greater influence of western boundary system on the AMOC variability at 22.5°S; highlight the importance of high resolution in situ data for AMOC estimations; and contribute for a better understanding of AMOC and MHT variability in the South Atlantic.

An ARGO and XBT observing system for the Atlantic Meridional Overturning Circulation and Meridional Heat Transport (AXMOC) at 22.5ºS

I. Pita[1,2,3], M. Goes[2,3], D. L. Volkov[2,3], S. Dong[3], G. Goni[3] and M. Cirano[4]

[1]Rosenstiel School, University of Miami, Miami, FL, United States of America.

[2]Cooperative Institute for Marine and Atmospheric Studies, University of Miami, Miami, FL, United States of America.

[3]Atlantic Oceanographic and Meteorological Laboratory, NOAA, United States of America.

[4]Department of Meteorology, Institute of Geosciences, Federal University of Rio de Janeiro (UFRJ), Brazil

Corresponding author: Ivenis Pita (ivenis.pita@noaa.gov)

Key Points:

- First in situ based Atlantic Meridional Overturning Circulation and Meridional Heat Transport time series estimation at 22.5ºS
- Mapping methodology used is robust and captures the climatological pattern for Atlantic Meridional Overturning Circulation
- Western boundary system drives interannual Atlantic Meridional Overturning Circulation variability, followed by eastern boundary system

Abstract

Changes in the Atlantic Meridional Overturning Circulation (AMOC) and associated Meridional Heat Transport (MHT) can affect climate and weather patterns, regional sea levels, and ecosystems. However, despite its importance, direct observations of the AMOC are still limited spatially and temporally, particularly in the South Atlantic. The main goal of this study is to implement a cost-effective trans-basin section to estimate for the first time the AMOC at 22.5°S, using only sustained ocean observations. For this, an optimal mapping method that minimizes the difference between surface in-situ dynamic height and satellite altimetry was developed to retrieve monthly temperature and salinity profiles from Argo and XBT data along the 22.5°S section. The mean AMOC and MHT for 22.5°S were estimated as 15.55±2.81 Sv and 0.68±0.18 PW, respectively, and are stronger during austral fall/winter and weaker in spring. The high-resolution XBT data available at the western boundary are vital for capturing the highly variable Brazil Current, and our section shows a significant improvement when compared to Argo database. The mean values, interannual and seasonal time series of AMOC and MHT were compared with other products. At 22.5S the North Atlantic Deep Water is divided into two cores that flow along both western and eastern boundaries near 2500 m depth. Our results suggest a greater influence of western boundary system on the AMOC variability at 22.5°S; highlight the importance of high resolution in situ data for AMOC estimations; and contribute for a better understanding of AMOC and MHT variability in the South Atlantic.

Plain Language Summary

The Atlantic Meridional Overturning Circulation (AMOC) is an ocean currents system associated with large-scale meridional transport of heat (MHT) and nutrients that can modulate climate, weather and ecosystems globally. In-situ measurements of the AMOC are still limited in space and time, particularly in the South Atlantic. Previous studies used synthetic methodologies based on statistical relationships between satellite sea surface height and in-situ temperature and salinity profiles to calculate AMOC in different latitudes. However, these methodologies are constrained by how good and stable these relationships are. Our new methodology obtains monthly AMOC and MHT estimates at 22.5°S by gridding scattered profiles along a reference section using optimal mapping parameters based on a sea level comparison to satellite data. The methodology can resolve the western boundary current, westward propagating sea level features and near coastal sea level variability. At 22.5°S the North Atlantic Deep Water is divided into two southward cores along the western and eastern boundaries near 2500 m depth. The AMOC is stronger during austral fall/winter and weaker in spring, and its interannual variability is linked primarily to the western boundary current changes. This work provides evidence that an AMOC monitoring section can be achieved by using solely sustained observations.

1 Introduction

The Atlantic Meridional Overturning Circulation (AMOC) is the zonal integral of the complex three-dimensional circulation, characterized by an upper cell connected to the deep convection in the North Atlantic subpolar region, and a lower or abyssal cell originated in the marginal seas off Antarctica (Broeker, 2003; Buckley and Marshall, 2016). The AMOC controls the distribution of heat and energy, tracers, and nutrients across the basin and links the timescales of heat uptake and carbon storage (Conway et al., 2018; Collins et al., 2019; Todd et al., 2019). The IPCC projections for the 21st century predict a significant weakening of the AMOC, which if it happens, will result in global and regional impacts on climate, weather, sea level, and ecosystems (Collins et al., 2019; Fox-Kemper et al., 2021; Lee et al., 2021). Theoretical and climate models suggest that the stability of the AMOC is dependent on the oceanic freshwater budget in the South Atlantic (de Vries & Weber, 2005; Stommel, 1961; Weijer et al., 2019). Depending on the sign of the freshwater transport into the South Atlantic, the AMOC may present a hysteresis behavior, in which a collapsed AMOC could be sustained even without an anomalous freshwater forcing (Rahmstorf et al., 1996; Stommel, 1961). Because the net freshwater transport across 35°S in the South Atlantic is southward (Garzoli et al., 2013), a weakening of the AMOC would increase the freshwater transport into the Atlantic, causing negative feedback to the AMOC recovery (Goes et al., 2019b). In addition, the AMOC is one of the main sources of uncertainties in climate model projections (Bellomo et al., 2021), which highlights the importance of sustained observational data for a more robust AMOC predictability. Therefore, the monitoring, hindcasting, and future projections of the AMOC variability are crucial for a better understanding of the Earth system dynamics.

Despite its importance, observations of the AMOC are still limited spatially and temporally, particularly in the South Atlantic (Rhein, 2019). There are only two in situ observing arrays of the AMOC in the South Atlantic: the TSAA/Tropical Atlantic Circulation and Overturning - TRACOS (11°S; Hummels et al., 2015; Herrford et al., 2021) and the South AMOC Basin-wide Array - SAMBA (35°S; Meinen et al., 2018; Kersalé et al., 2020). TRACOS uses a total of 5 bottom pressure stations to capture boundary variability on both boundaries of the Atlantic basin, combined with altimetry data to obtain AMOC anomalies at 11°S. Hummels et al. (2015) detected a salinity increase of up to 0.1 psu per decade from the surface to intermediate layers at 5°S and 11°S near the western boundary by comparing observations from two periods, 2013-2014 and 2000-2004. Using reanalysis data, Goes et al. (2014) associated the increase in salinity at intermediate depths to the increase of the salty Agulhas Leakage into the Atlantic, due to the strengthening of the westerlies associated to the Southern Annular Mode, similar to the mechanism described in Durgadoo et al. (2013). Herrford et al. (2021) observed an important seasonal cycle in the AMOC variability, where in the upper 300 m the eastern boundary forcing dominates the AMOC variability, but both eastern and western forcings are important from 300 to 500 m depth.

At 35°S, SAMBA array has been in place since 2009, in the beginning with six PIES, and over the years reaching more than twenty moorings, including two tall moorings deployed in December 2022. This array revealed strong variability on both upper and abyssal cells of the AMOC (Kersalé et al., 2020). The AMOC variability at 35°S is greatly influenced by the eastern boundary forcing at an interannual time scale, but the western boundary contributions are still significant (Meinen et al., 2018). The influence of the western boundary is greater on the AMOC variability at semiannual or shorter time scales (Meinen et al., 2018). These results suggest a greater influence of both boundaries on the AMOC dynamics in the South Atlantic when compared to the North Atlantic.

Recent studies have stressed the need for understanding the meridional coherence of the AMOC (e.g., Frajka-Williams, 2019; McCarthy et al., 2020). Anomalous signals from the South Atlantic can propagate towards the subpolar North Atlantic and affect deep water formation (Biastoch et al., 2009; Desbruyeres et al., 2021). The AMOC-induced heat and freshwater convergences and divergences drive changes in regional heat and freshwater contents and in sea level (Little et al., 2017; Volkov et al., 2019), which can impact the climate locally (Chang et al., 2008) and remotely (Lopez et al., 2016).

Building an AMOC observing system at 22.5°S will bridge the two existing observing systems located at the edges of the South Atlantic subtropical gyre, and provide estimates that can be compared to the historical cross-basin hydrographic programs such as WOCE and GO-SHIP occurring since the early 1990s. However, building new, sustainable observing systems can be a daunting task due to the operational and financial costs associated with it (Chidichimo et al., 2023). Therefore, an AMOC observing system that can rely on existing sustained observations at no additional costs is a strategic opportunity that will enhance our understanding of this vital climate component.

Although there are altimetry-based AMOC reconstructions at a few locations in the South Atlantic (e.g., Dong et al., 2021, Schmid et al., 2018), these estimates rely on linear regression between altimetry and in situ data, which are dependent on the reliability of these relationships. However, between 11°S and 35°S, an AMOC estimate which relies solely on sustained hydrographic data has not been attempted previously. At 22°S, the existing AX97 XBT high-density transect, which to date accounts for nearly 100 sections, can be a reliable constraint of the variability of the western boundary current, which is known to have a great influence on the AMOC variability in other locations (e.g., Gulf Stream). In addition, according to Dong et al. (2021), the AMOC time series at 35°S is not correlated with 20°S, which suggests a different regime than the current existing arrays, thus the 22°S estimate can serve as a benchmark for the AMOC variability in this latitude.

With that said, we implement a cost-effective transbasin section at 22.5°S to estimate the AMOC and its seasonal and interannual variability over 2007-2020 by merging available in situ observations and reanalysis products.

This paper is organized as follows: the in situ and reanalysis data used in this study are presented in Section 2, as well as the methodology to construct the referenced transect and its AMOC estimation. Section 3 consists in evaluating the methodology. Section 4 presents the AMOC and Meridional Heat Transport (MHT) time series, and their different components from the reference section and from other products available in the region. Section 5 gives a summary of the present study.

2 Data and Methods

2.1 In-situ profile data

Observational data from three high density expendable bathythermograph (XBT) transects (AX08, AX18 and AX97) and Argo profiling floats in the South Atlantic Ocean are used to build a transbasin transect near 22.5°S (Figure 1). The XBT probes measure temperature

(T) along fixed transects from surface to depths of about 800 m, and Argo floats measure T and salinity (S) down to 2000 m. The AX08 transect crosses the Atlantic Ocean from Cape Town (South Africa) to New York (USA), spanning through the eastern part of the South Atlantic subtropical gyre. The AX18 transect monitors the AMOC and MHT with two cross-basin zonal transects at approximately 34.5°S, and some of its realizations go further north to ~24°S in the western side of the basin depending on the availability of merchant ships. The AX97 monitors the BC at 22°S from Rio de Janeiro (Brazil) to Trindade Island (~30°W). The average temporal sampling frequency of AX08 and AX18 transects is 3 months/year and 2 months/year for the AX97. The average horizontal resolution ranges from 18 to 27 km. T data from XBT probes are obtained from the NOAA/AOML database. S profiles are derived from XBT-based T profiles using a seasonal regression method proposed by Goes et al. (2018). Delayed mode Argo profile data (Argo 2020) are used from the Global Argo Data Repository of the National Centers for Environmental Information (NCEI). Only Argo T-S profiles flagged as good or potentially good are used. The disparity found in some profiles, for which the available S data were fewer than the T data, was circumvented by applying the same regression methodology to estimate S for the XBT profiles.

To complete the profiles for the full water column, i.e., below 800 m for XBT data and below 2000 m for Argo data, the 0.25º horizontal resolution NCEI World Ocean Atlas 2018 (WOA18) T-S climatology is used, at monthly averages between 800 and 1500 m, and seasonal averages below 1500 m (Garcia et al., 2019; Locarnini et al., 2018; Zweng et al., 2018). Monthly WOA18 data have 57 vertical levels from 0 to 1500 m, and seasonal data have 112 vertical levels from 0 to 5500 m. Sensitivity tests performed with Argo data showed that the effect of padding from 800-1600 m is negligible relative to uncertainties that arise from the sampling strategies and from the methodologies of heat and volume transports calculation.

Each T-S profile is linearly interpolated to 140 pre-defined depths, starting from 5 m at 10 m intervals until 750 m, 50 m intervals until 2000 m, and 100 m intervals until a maximum depth of 6000 m.

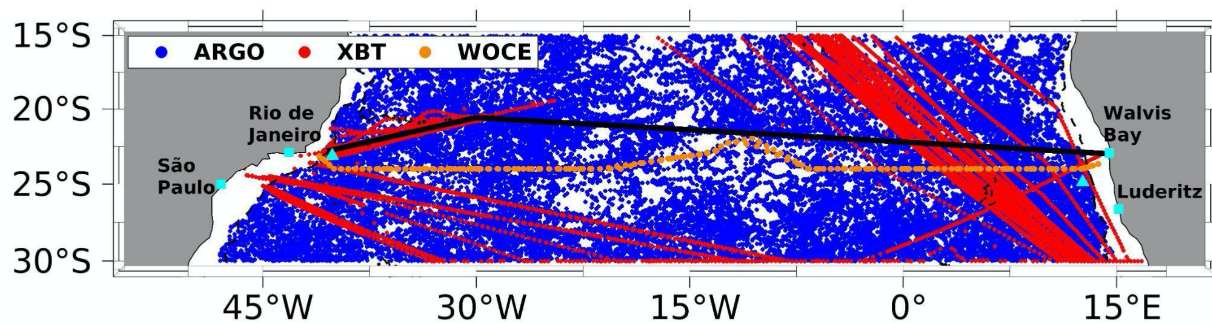

Figure 1. Spatial distribution of in situ data used in this work. Location of Argo (XBT) profilers are represented by blue (red) dots, and yellow dots represent the location of T-S profilers acquired at WOCE cruises in 2009 and 2018. The reference transect is represented by the black line. The location of coastal tide gauges is represented by cyan squares. Cyan triangles represent

the coordinates of sea level data from altimetry dataset compared to AXMOC data at the boundaries. Dashed black lines represent the 1000 m isobath.

2.2 Auxiliary data

To estimate the Ekman component of the AMOC, we use the monthly zonal wind stress from the ERA5 atmospheric reanalysis (Hersbach et al., 2020), which is available at a 0.25º horizontal grid since 1979. We linearly interpolated ERA5 wind stress to the reference section for the period 2007-2020.

For data validation, comparison, and water mass analysis, we used the Argo T-S 0.5° x 0.5° gridded monthly climatology (RG Argo- Roemmich & Gilson, 2009) from 2007-2020, and the World Ocean Circulation Experiment (WOCE) hydrographic profiles (Koltermann et al., 2011). The WOCE T-S data from transect A9.5 located close to 24°S from South America to Africa were acquired by two different scientific cruise surveys in 2009 and 2018 (740H20090307 and 740H20180228, respectively). A total of 238 CTD/O_2 stations were collected in those 2 periods, and 214 of those stations were used in this study (Figure 1). WOCE data are interpolated to the same 140 pre-defined depths used in the XBT and Argo profiles. WOCE data are used as independent measurements to evaluate the methodology adopted by this study in obtaining high-resolution T-S sections at 22.5°S. We also used the T-S from ECCO version 4 release 4 (ECCOv4r4), covering the period 1992-2017 at a 0.5° x 0.5° horizontal resolution. This product is an updated edition to that described by Forget et al. (2015). Finally, for the in situ profile data mapping calibration and validation, we use monthly gridded sea level anomaly (SLA) from January 1993 to December 2020 from a multi-satellite altimetry mission, processed and distributed by the Copernicus Marine and Environment Monitoring Service (CMEMS). The SLA maps are filtered, bias corrected, and corrected for atmospheric pressure effects and tides using the method of Pujol et al. (2016). Monthly maps of a 20-yr mean dynamic topography (Rio et al., 2011) are added to SLA to obtain the sea surface height (SSH) fields. The global mean sea level rose on a rate of 3.35±0.4 $mm\ yr^{-1}$ from 1993 to 2017 (Ablain et al., 2019), which was ~1.95 $mm\ yr^{-1}$ higher than the calculated in situ dynamic height (DH) trends. To avoid time varying biases during the mapping optimization phase, linear trends are removed from the fields at each longitude of the reference transect.

2.3 High-Resolution T-S Reference Section mapping methodology

A high-resolution reference section based on Argo and XBT data at 22.5°S, hereafter AXMOC, was defined in order to maximize the data availability along the section. Therefore, on the western side of the basin, the section follows the AX97 XBT transect from Rio de Janeiro to Trindade Island (~30°W), and from 30°W to Walvis Bay in Namibia. Long-record tide gauges are located on both ends of the reference transect (Figure 1). Data from two other XBT transects, the AX08 and AX18 are used to improve data coverage locally along their tracks. The coverage of Argo profiles is greater where bathymetry is deeper than 1000 m, and it has improved after 2007 in the South Atlantic following the initial spinup of the program since 2004 (Roemmich et al., 2009).

The mapping methodology used to reconstruct the reference section consists in weighted averages (Goes et al., 2010; Goes et al., 2020) using a normalized separable exponential function in space and time, given by:

$$W = exp\left(-\frac{\sqrt{x^2+y^2}}{\Delta R}\right) * \exp\left(-\frac{\delta t^2}{\Delta t}\right) \qquad (1),$$

where ΔR is a spatial radius, Δt is a time window, δt is the time difference between the profile and the reference time (15th of each month), and x and y are the zonal and meridional distance between the profile location and the referenced coordinate position, respectively. A set of 20 reference sections is generated considering a combination of weight values obtained varying ΔR (0.25°, 0.50°, 1°, 3° and 5° radius) and Δt (30, 60, 90 and 180 days). The search radius at the boundaries (<30°W and >0°) are enlarged in the y-direction by a factor of 3 with a cut off of 5° in order to minimize data gaps, assuming the features are more coherent along the boundaries than across.

The optimal T-S section is obtained by optimizing the mapping parameters ΔR and Δt locally by reducing the root mean squared error (RMSE; used as a cost function) between absolute DH and the SSH data interpolated to the reference section (Figure 2). The absolute DH of each parameter subset is referenced to 1000 m, and the absolute geopotential field from a blended Argo/altimetry climatology product is added to the reference level, similar to Goes et al. (2019). During calibration, both data are detrended in time to avoid misfits due to the mass and barotropic components of the variability in altimetry data.

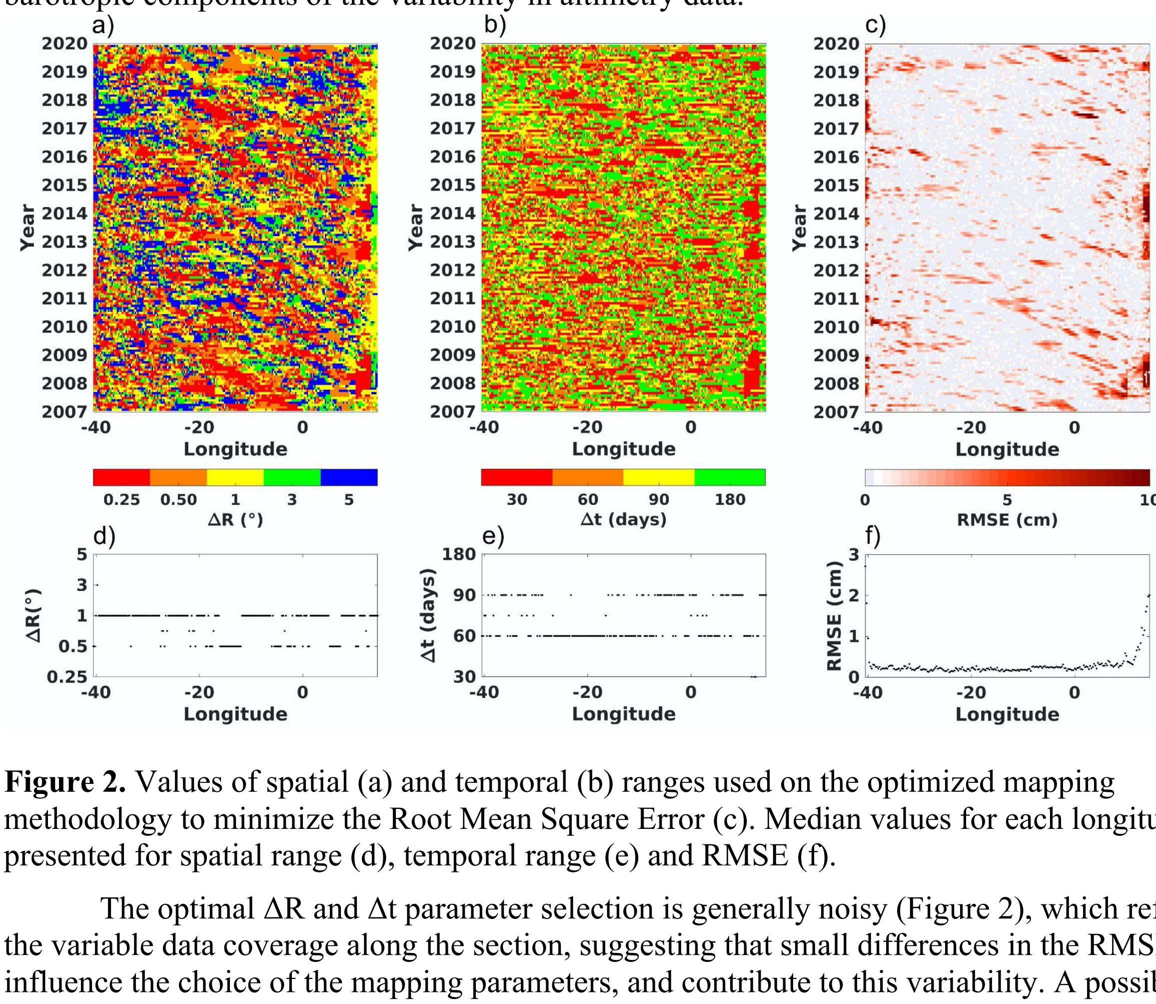

Figure 2. Values of spatial (a) and temporal (b) ranges used on the optimized mapping methodology to minimize the Root Mean Square Error (c). Median values for each longitude are presented for spatial range (d), temporal range (e) and RMSE (f).

The optimal ΔR and Δt parameter selection is generally noisy (Figure 2), which reflects the variable data coverage along the section, suggesting that small differences in the RMSE can influence the choice of the mapping parameters, and contribute to this variability. A possible solution to this issue is to include a prior probability distribution in the parameters to prioritize ΔR and Δt with higher resolution when RMSE variability is small among the different parameters (e.g., Goes et al., 2010). From sensitivity experiments, the impact of this approach in the final AMOC and MHT time series is small, even for higher ΔR and Δt values, since our methodology guarantees that greater weight is given to data closer in time and space to the referenced transect at a given time (Equation 1). The median ΔR (Δt) values fall between 0.50° and 1° (60 and 90 days) for every point of latitude (Figure 2d-e). Therefore, the median RMSE value between absolute HD and SSH is 0.79±1.40 cm, and increases to ~2 cm in the eastern boundary (Figure 2f). These values fall well within previously published RMSE values of 6.2 cm for areas between 5°S and 15°S, and up to 14 cm at the boundaries (Arnault et al., 1992; Strub et al., 2015).

2.4 AMOC and MHT time series

The AMOC and MHT across the reference section are calculated following published methodologies for the South Atlantic (e.g., Dong et al., 2015, 2021; Goes et al., 2015, 2020). The AMOC and MHT are divided into geostrophic and Ekman components. The geostrophic velocity field is computed from the gridded T-S data, using 3700 m as reference level, since it is approximately the depth of the neutral density γ=28.1 kg/m3, usually considered as the boundary between North Atlantic Deep Water (NADW) and Antarctic Bottom Water (AABW) at 22.5°S (see Section 3.3). This reference depth is similar to the one defined for 34.5°S (Goes et al., 2015). A zero net volume transport constraint is applied to the section at each month by adjusting the velocity field with a constant, calculated from the integrated transport across the section divided by the area of the section. The geostrophic AMOC streamfunction is estimated from the adjusted velocities, and its strength is defined as the maximum streamfunction at each timestep. The geostrophic time series is smoothed with a 3-month low-pass gaussian filter in order to remove high-frequency signals. The Ekman component, estimated using the ERA5 reanalysis, is integrated to the depth of the Ekman layer, which is considered to be 50 m deep. Both the AMOC and MHT represent the sum of Ekman end geostrophic components. The time series of the AMOC and MHT span from 2007 to 2020, since the AX97 transect started in 2004 and the Argo data has been more widely available across the South Atlantic basin after 2007.

3 Results

In this section, sea level, boundary currents, and water mass characterization are presented to evaluate the AXMOC product. The AMOC and MHT time series are decomposed into the seasonal, interannual (low-pass filtered with a 13-month Gaussian), as well as Ekman and geostrophic components.

3.1 Sea level

Here, the SLA calculated along the AXMOC transect from 2007 to 2020 is compared with the ones obtained from satellite altimetry and from the RG Argo data (Figure 3). Westward propagating signals are observed in satellite altimetry. These signals take between 2 to 4 years to cross the basin from east to west, generally without significant energy loss along their path, showing the importance of wave generation near the eastern boundary. An average phase speed of 5.9 ± 1.6 km/day is estimated for these propagations following the method of Barron et al. (2009), which corresponds to the period of the 1st baroclinic Rossby wave mode near 22.5°S (Polito and Liu, 2003). This westward propagation is not seen in the RG Argo product due to a rather coarse spatial and temporal mapping resolution. Nevertheless, our optimized mapping methodology calibrated to the SLA altimetry data allows detecting these propagation patterns reliably, in a good agreement with satellite altimetry data (Figure 3a, b).

A basin-wide, multi-year SLA pattern is observed in all three products, characterized by positive anomalies from 2007 to Jun/2010, negative between Jun/2010 and Apr/2015, and again positive from Apr/2015 to Dec/2020. As this variability pattern is characteristic for the entire basin, it could be linked to large-scale climate modes.

The proposed mapping methodology (AXMOC) also adequately reproduces the strong SLA variability near the boundaries, particularly near the western boundary due to the higher density of XBT data in the region. Near the eastern boundary, both satellite altimetry and AXMOC products capture some strong SLA signals, such as the negative anomalies in 2012-2013 and the positive anomalies in 2008-2009, 2017 and 2018-2019.

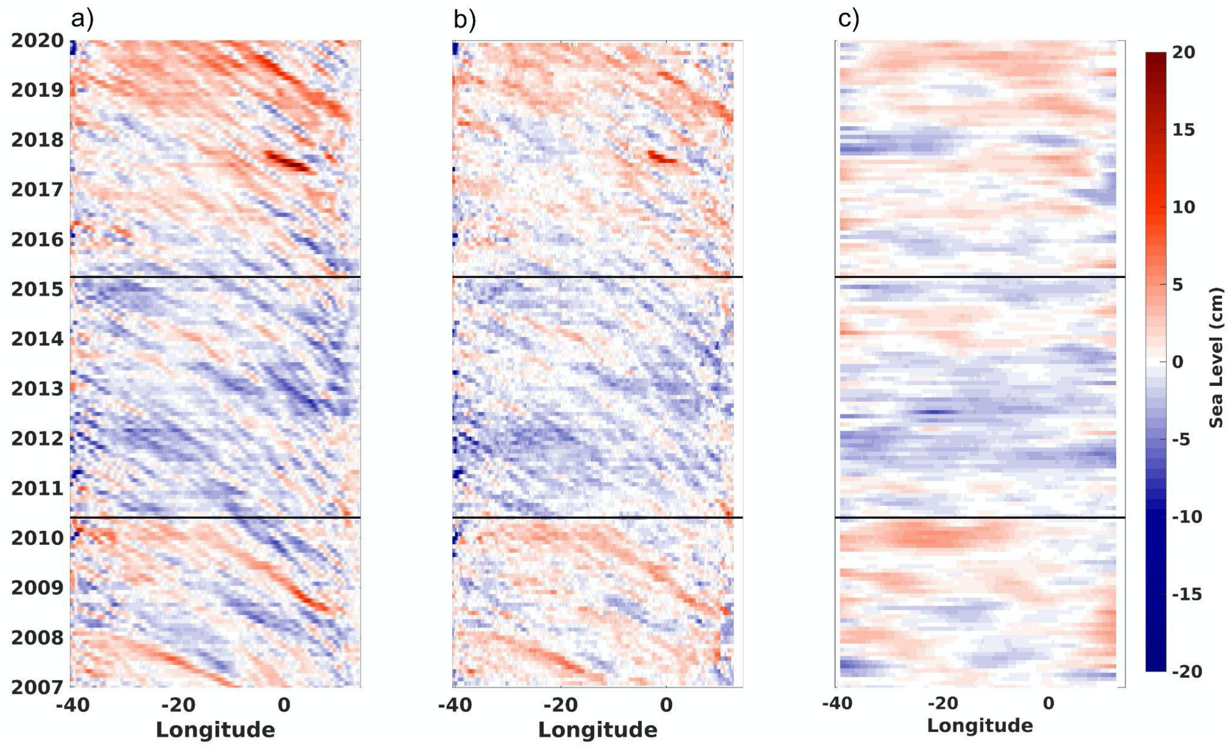

Figure 3. Hovmoller plot of the sea level obtained by altimetry (a), AXMOC (b) and RG Argo (c) datasets. Black horizontal lines indicate dates of 06/2010 and 04/2015. All datasets are de-seasoned and detrended to focus on the interannual variability.

The comparison of SLA time series from satellite altimetry and the AXMOC data near the western (40°W) and eastern boundaries (12.5°E) also validates the proposed methodology and provides valuable insight of the boundary currents variability (Figure 4). Since satellite SSH has other contributions than steric sea level, particularly in coastal areas, we selected for the boundary sea level height comparison with AXMOC the location of the satellite altimetry time series with higher correlation within 3° from the boundaries. The selected locations for the altimetry product are 40.12°W, 23.12°S (western boundary), and 12.62°E 24.87°S (eastern boundary), shown in light blue triangles in Figure 1. Overall, the region near the western boundary has greater variability compared to the eastern boundary (Figure 4). The standard deviation (used as a proxy of variability) of the SSH near the western boundary was 5.7 cm

(Figure 4a), and 3.4 cm (Figure 4b) near the eastern boundary. The AXMOC data show similar values to SSH near the western (4.9 cm) and eastern (3.1 cm) boundaries.

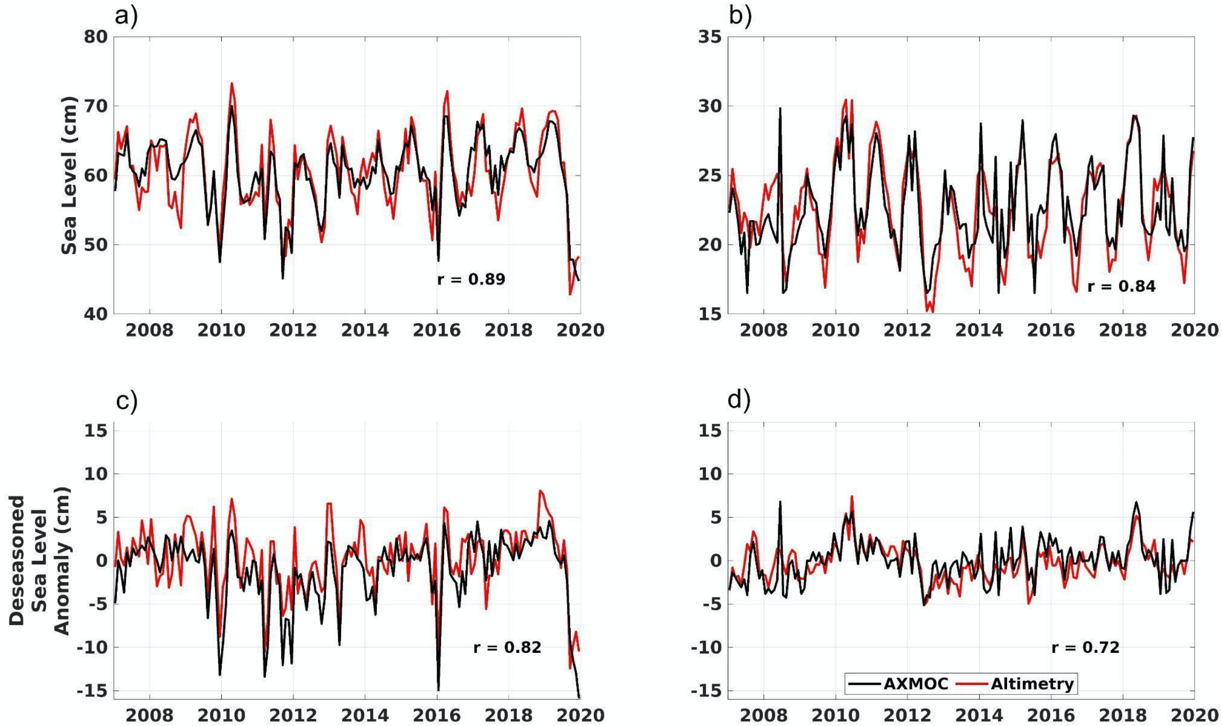

Figure 4. Absolute (a and b) and de-seasoned (c and d) SSH at the western (a and c) and eastern (b and d) boundaries of the section. Red is for altimetry data, and black is for the AXMOC estimates. The associated correlation values are shown in each panel.

A good correlation of sea level from AXMOC with altimetry data was obtained at both boundaries (0.89 at the western and 0.84 at the eastern boundary). When considering the de-seasoned sea level anomaly, the correlation at both boundaries remained robust (0.82 for the western and 0.72 for the eastern boundary). Most of the SLA extreme events that arise in the altimetry data also appeared in the AXMOC data (e.g., extreme values at the end of 2009, 2011, 2016, and end of 2019 at the western boundary, and the extreme values early 2010, mid 2012 and mid 2018 at the eastern boundary). The robust correlations observed on both ends of the section, even though the western boundary is densely sampled by XBTs and the eastern boundary is only sparsely sampled by Argo floats, indicate that the use of a sea level-oriented mapping methodology is appropriate to monitor the evolution of near-coastal features.

3.2 Boundary currents

Here, we compare boundary currents derived from the AXMOC with those derived from the RG Argo and simulated by the ECCOv4r4 state estimate. At 22.5°S, the BC is a shallow and narrow southward flow along the Brazilian coast placed on top of the northward inflow of the Intermediate Western Boundary Current (Calado et al., 2008). In the AXMOC data, the mean BC is located west of 39°W in the top 500 m (Figure 5). In the RG Argo, the BC is constrained to the west of 39.75°W, and a strong northward core appears east of 39.75°W, which is an artifact caused by the reverse DH gradient created from the lack of in situ data near the western boundary (Goes et al., 2020). In ECCOv4r4, the BC appears shallower and wider (west of 38°W) than in the AXMOC data. To analyze its volume transport in the three data products, we define the BC as the southward flow in the upper 500 m between the western boundary and 38°W. The 10-year (2007 to 2017) averaged and standard deviation of the volume transport is higher (-3.74±1.92 Sv) for the AXMOC, compared to -1.95±0.62 Sv for the RG Argo and -3.23±1.03 Sv for the ECCOv4r4. The mean BC core speed is also higher in the AXMOC data (-0.19±0.10 $m\ s^{-1}$) than in the RG Argo (-0.15±0.04 $m\ s^{-1}$) and ECCOv4r4 data (-0.10±0.02 $m\ s^{-1}$). The BC transport mean and standard deviation are better represented by AXMOC data when compared to previous regional studies (e.g., da Silveira et al. 2008; Lima et al., 2016; Mata et al., 2012; Pereira et al., 2014; Pita et al., 2020). This increased variance of the AXMOC is caused by a stronger BC interannual variability, which captures the strong event in the summer of 2009/2010, analyzed in Goes et al. (2019), as well as other events such as 2014 and 2016 which were also observed in that study. This interannual variability is dampened in the other two products.

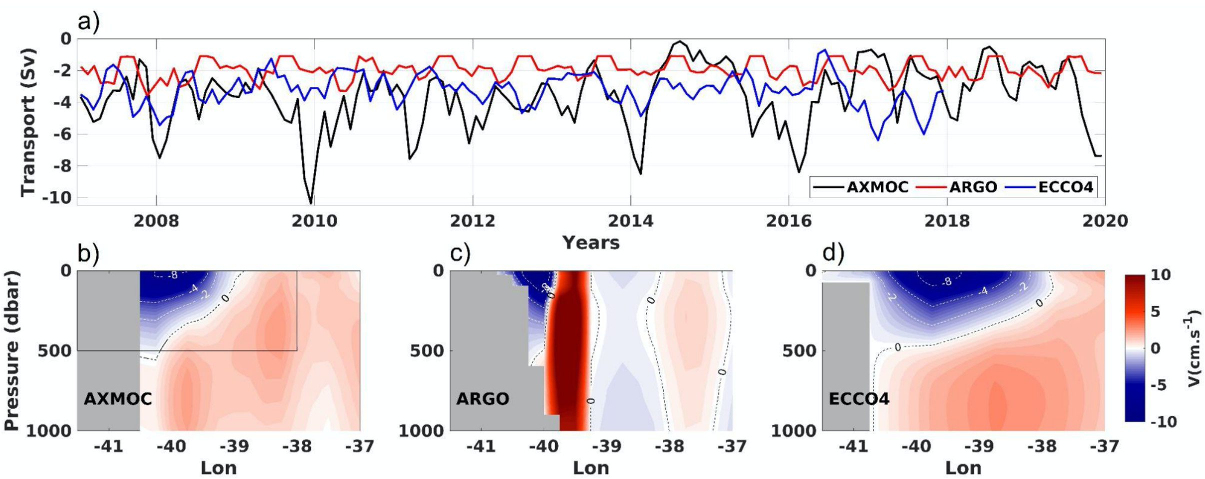

Figure 5. Evolution of the Brazil Current (BC) transport from 3 different data (a): AXMOC (black line), RG Argo (red line) and ECCOv4r4 (blue line). Mean velocity section focused on western boundary is shown for AXMOC (b), RG Argo (c) and ECCOv4r4 (d) datasets. The black rectangle indicates the region where the BC transport is being calculated.

Close to 22°S, the Benguela Current (BeC) is the eastern boundary current, which flows equatorward between the coast to 3°E, limited by the Walvis ridge (Garzoli et al., 1996; Majumder and Schmid, 2018). The AXMOC data capture the BeC as an equatorward flow from surface down to 500 m with a core located between 10 and 12°E (Figure 6). The poleward flow east of 12°E is the expression of the Poleward Undercurrent (PU), an ocean current derived from the sinking of the Angola Current at the Angola Benguela Frontal Zone (ABFZ - Berger et al., 1998). On the other hand, the RG Argo data shows a strong equatorward flow along the edge of continental shelf, due to the lack of data near the coast. The BeC transport of 12.57±2.58 Sv observed in AXMOC is greater than the ones in the RG Argo (9.99±1.95 Sv) and ECCOv4r4 data (3.43±0.68 Sv). AXMOC data perceive a more intense and variable BeC if compared to other products. The ECCOv4r4 estimate of BeC transport is lower than the AXMOC and RG Argo data. The ECCOv4r4 data capture a smoother BeC, with smaller interannual variability. The AXMOC results are in accordance with Majumder and Schmid (2018), which also reported a decreasing mean BeC volume transport on lower latitudes, varying from 23 Sv at 31°S to approximately 9 Sv at 25°S.

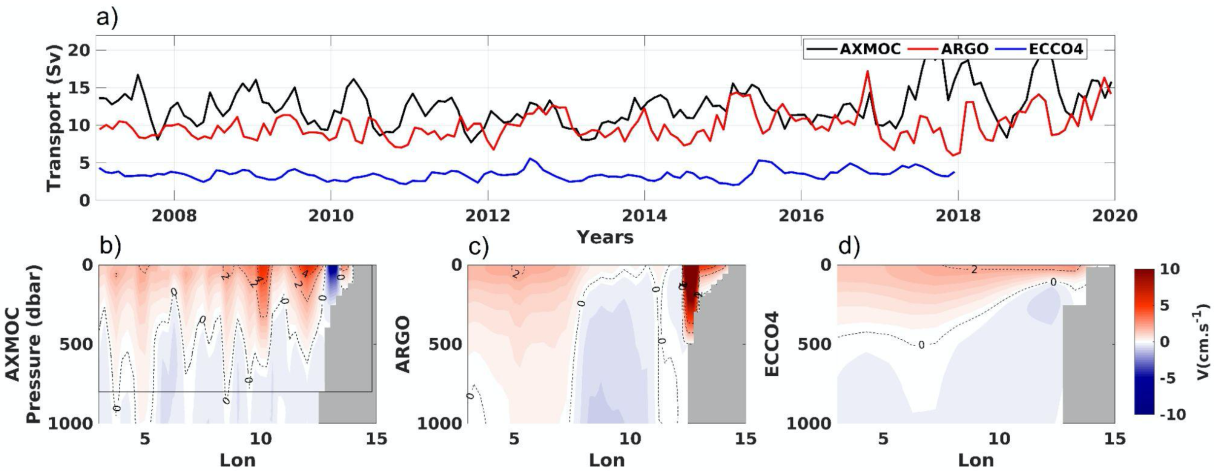

Figure 6. Evolution of the Benguela Current (BeC) transport from 3 different data (a): AXMOC (black line), RG Argo (red line) and ECCOv4r4 (blue line). Mean velocity section focused on the eastern boundary is shown for AXMOC (b), RG Argo (c) and ECCOv4r4 (d) datasets. The black rectangle indicates the region where the BeC transport is being calculated.

3.3 Water masses

This subsection covers the water masses captured by the AXMOC data and compares its results with alternative independent in situ data from WOCE. The transbasin section at 22.5°S is characterized by more intense circulation on both boundaries in comparison to the interior of the section (Figure 7). Most of the variability along the section is concentrated in the upper ocean and near the boundaries (Figure 7b).

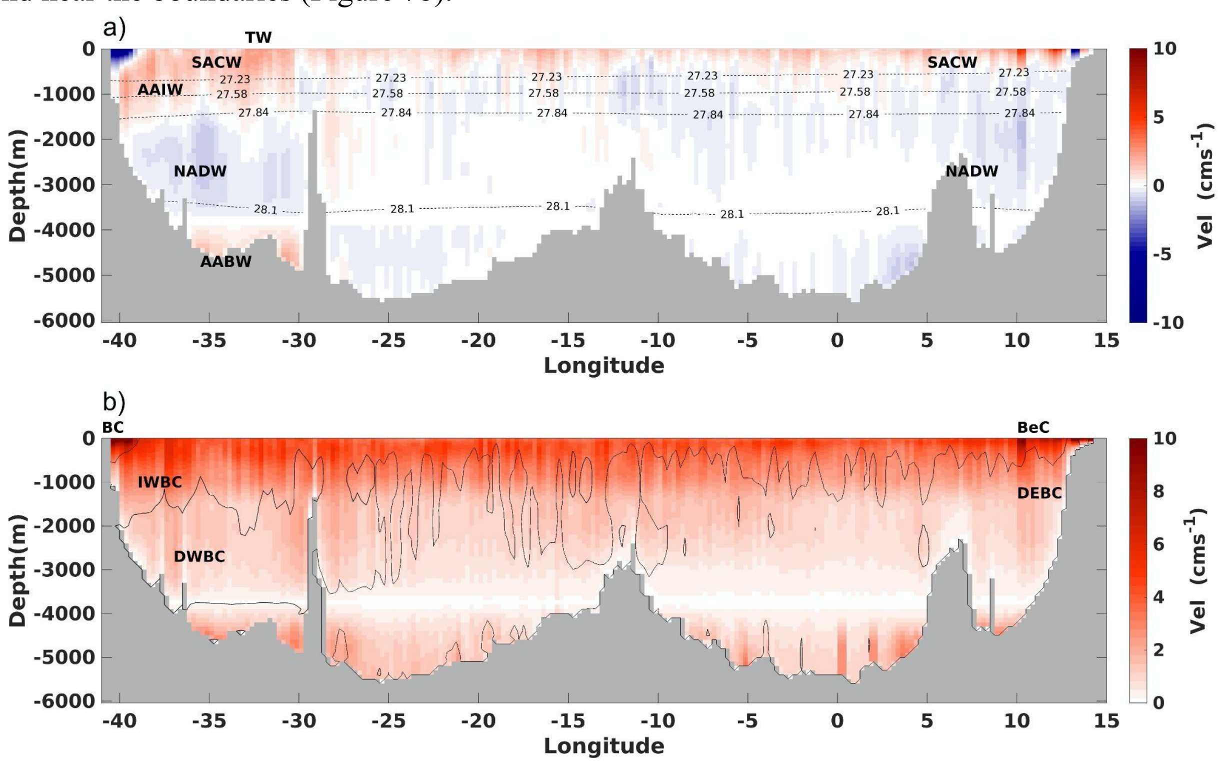

Figure 7. Mean northward velocity (a) and its standard deviation (b) computed from the AXMOC data. Main water masses (a) and ocean currents (b) are indicated: Tropical Water (TW), South Atlantic Central Water (SACW), Antarctic Intermediate Water (AAIW), North Atlantic Deep Water (NADW), Antarctic Bottom Water (AABW), Brazil Current (BC), Benguela Current (BeC), Intermediate Western Boundary Current (IWBC), Deep Western Boundary Current (DWBC) and Deep Eastern Boundary Current (DEBC). Neutral density isopycnals are represented by dashed lines (a). Solid lines indicate contour of no meridional velocity (b).

The AABW is the deep equatorward flow (>4000 m) confined in the western boundary west of 30°W, constrained by the Trindade Island topography, and its mean flow reaches speeds of 0.02 ± 0.01 $m\ s^{-1}$ at 22.5°S (Figure 7). The AABW is characterized by T < 2°C, S < 34.8 and reduced dissolved oxygen levels ($O_2 \simeq 220\ \mu mol\ kg^{-1}$) relative to NADW (Figures 8 and S1), which is in agreement with Reid et al. (1989). Between 50°S and the equator, the AABW flows along neutral density lines $\boldsymbol{\gamma}$> 28.10 $kg\ m^{-3}$ (Liu & Tanhua, 20219).

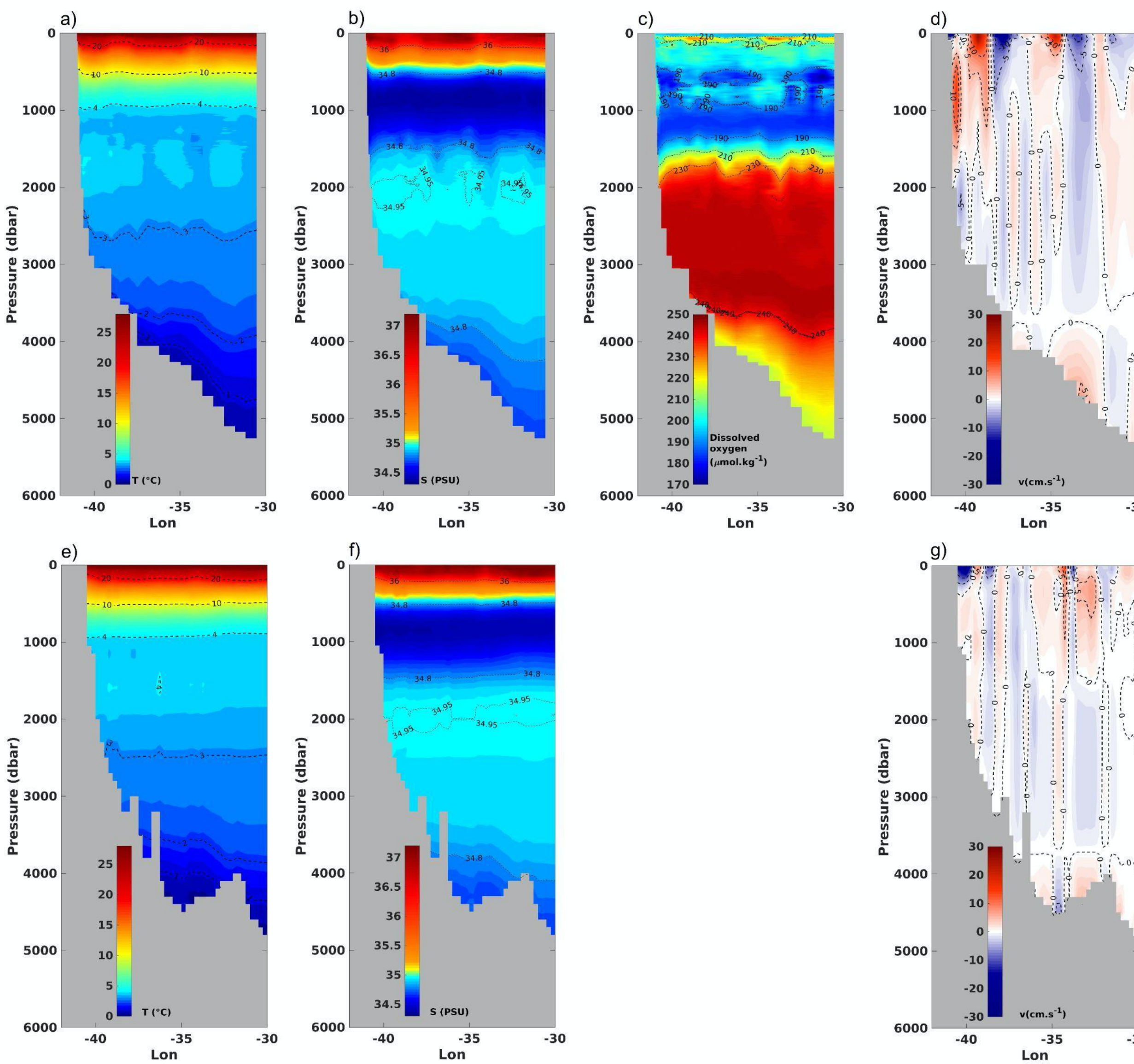

Figure 8. Ocean tracers and velocity section focused on western boundary for April 2009 at 24 and 22.5°S. A-d (e-g) panels represent WOCE (AXMOC) dataset. Temperature (T), salinity (S), dissolved oxygen and velocity (v) are shown between western boundary and 30°W.

Similar to the AABW, the NADW is also confined by local topography near the western boundary. Near the eastern boundary (Figure 7), a secondary southward NADW branch is also visible. Indeed, the NADW has been reported to split into two branches before crossing 22°S: one branch remains flowing southward near the western boundary and another branch flows eastward along the equator (Talley, 2011). Both branches are located between 1700 and 3600 m and the western branch is more intense, reaching up to -0.01 ± 0.01 $m\ s^{-1}$ at 22.5°S (Figure 7). In the tropics, the NADW is usually divided vertically into the upper (uNADW) and lower NADW (lNADW - Talley 2011) cores. As it flows southward, vertical mixing slowly merges this two-lobed water mass into one main core flowing between neutral density surfaces of 27.84 and 28.10 $kg\ m^{-3}$ (e.g., Hernandez-Guerra et al., 2019; Liu & Tanhua, 2021; Stramma et al., 2004). This single core signal is observed on both branches of the NADW (Figure 7), which is characterized by a local maximum in salinity (S >34.85) and a maximum in dissolved oxygen (O_2 > 240 $\mu mol\ kg^{-1}$) near the western boundary (Figure 8).

The Upper Circumpolar Deep Water (UCDW) is defined as a fresh (core S around 34.6), low oxygen water mass with neutral density between 27.58 and 27.84 $kg\ m^{-3}$ and located between 1150 and 1550 m deep (e.g., Hernandez-Guerra et al., 2019). It is characterized by low salinity (S<34.8) and poor oxygen levels (O_2 < 190 $\mu mol\ kg^{-1}$; Figure 8). Located above the UCDW, at depths varying from 700 and 1150 m, the Antarctic Intermediate Water (AAIW) is characterized by a minimum salinity at its core (S < 34.5) located around 800 m, and relatively high oxygen levels, flowing along neutral densities between 27.23 and 27.58 $kg\ m^{-3}$. Both UCDW and AAIW form the Intermediate Western Boundary Current system (IWBC) at 22.5°S (Figure 7), which is characterized by an equatorward flow near 38°W between about 600 and 1700 m depth (Figure 7).

The isolines of T, S and dissolved oxygen in the AXMOC and WOCE data are located at similar depths (Figure 8 and S1). The isolines of the WOCE data are more variable, while the AXMOC isolines are smoother because of the time and space averaging applied during the mapping procedure. The WOCE data is based on CTD casts, and has not been smoothed.

A direct comparison of volume transport per neutral density intervals is an important step to evaluate the mapping methodology applied here (Figure 9). While AXMOC and WOCE estimations are calculated from their respective T-S profiles, Cainzos et al. (2022) employ an inverse box model to compute decadal AMOC estimates from WOCE transects. The top layer (from surface to $\boldsymbol{\gamma}$= 26.45 $kg\ m^{-3}$) is composed by the geostrophic transport and the Ekman transport, while the remaining intervals are composed solely by the geostrophic transport. A good agreement exists between AXMOC and WOCE volume transport estimates in the upper 1000 m, characterized by $\boldsymbol{\gamma}$< 27.58 $kg\ m^{-3}$. The AXMOC data show a transport of 20.60 Sv and 20.48 Sv for Apr/2009 and Mar/2018, respectively. The volume transports in the WOCE data are 22.78 Sv and 18.95 Sv for Apr/2009 and Mar/2018, respectively. The difference between the WOCE and the AXMOC data in the upper ocean ($\boldsymbol{\gamma}$< 27.58 $kg\ m^{-3}$) is generally within the uncertainty interval estimated by Cainzos et al. (2022).

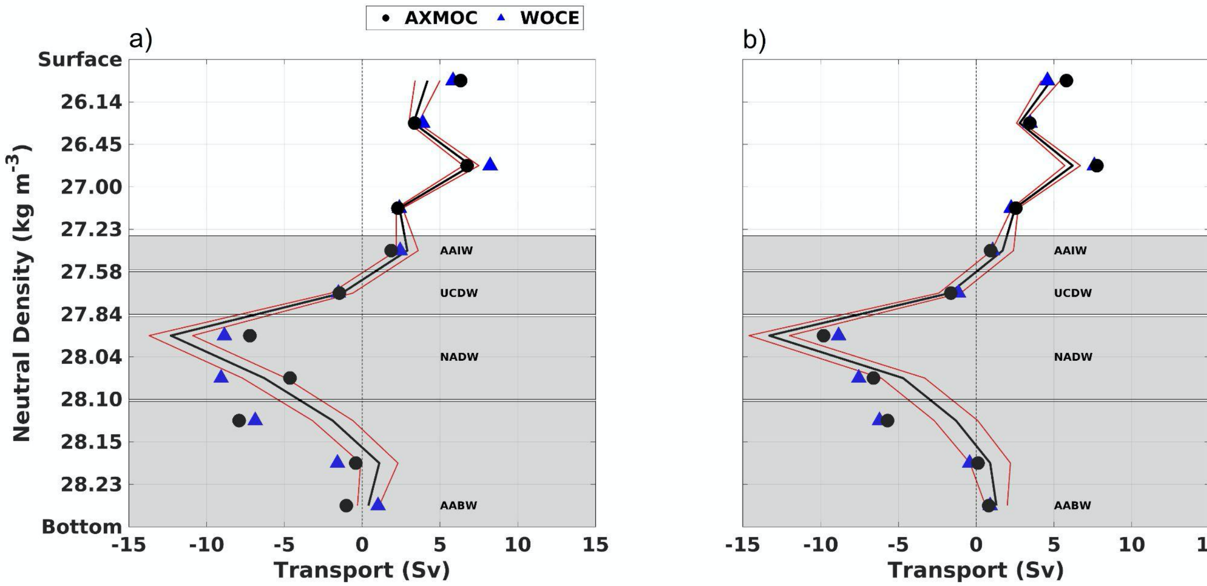

Figure 9. Volume transport at different neutral density levels for two different months: Apr/2009 (left panel) and Mar/2018 (right panel). AXMOC data is represented by black circles and WOCE data by blue triangles. Black line and red lines represent the volume transport and its uncertainties estimated by the inverse model of Cainzos et al. (2022) for the decades of (left) 2000s and (right) 2010s decades. The gray areas represent the density ranges of the main water masses across the section: Antarctic Intermediate Water (AAIW), Upper Circumpolar Deep Water (uCDW), North Atlantic Deep Water (NADW) and Antarctic Bottom Water (AABW).

The area encompassing upper layer boundary currents ($\boldsymbol{\gamma}$ < 27.23 $kg\ m^{-3}$), i.e., BC and BeC, has a positive net volume transport of 18.74 Sv and 19.55 Sv for Apr/2009 and Mar/2018, respectively (Figure 9). For WOCE data, the volume transports are 20.34 Sv and 17.89 Sv for Apr/2009 and Mar/2018, respectively. AXMOC and WOCE results are similar in every level for both periods analyzed (Apr/2009 and Mar/2018), and this similarity is also observed with the decadal results from Cainzos et al. (2022). At 22.5°S, the upper AMOC cell is located from surface to $\boldsymbol{\gamma}$=27.58 $kg\ m^{-3}$, and the lower AMOC cell is located from $\boldsymbol{\gamma}$=27.58 $kg\ m^{-3}$ to the bottom. Considering the layer encompassing the UCDW, the resulting AXMOC-based transport is slightly negative of -1.47 Sv and –1.62 Sv for Apr/2009 and Mar/2018, respectively (Figure 9), because the more intense intermediate equatorward currents are limited to the western boundary, while the interior and eastern boundary have poleward flow (Figure 7). In both periods analyzed, the NADW is the main conduit of the lower AMOC cell from neutral density of 27.84 to 28.10 $kg\ m^{-3}$ (Figure 9). Finally, the resulting transport on the layer encompassing the AABW turns back poleward mainly because of the influence of the deep western boundary current. The mapping methodology is robust considering that most of its estimates fall within 2 times the uncertainty levels of the independent study performed by Cainzos et al. (2022), especially in the upper ocean. It is important to highlight that both sections, AXMOC and WOCE (also used as reference in Cainzos et al., 2022), are not located at the same latitude. WOCE section is located around 24°S and AXMOC transect location varies between 20.5 and 23°S. Greater differences from AXMOC, WOCE and Cainzos et al. (2022) are observed in areas with $\boldsymbol{\gamma}$ > 27.84 $kg\ m^{-3}$, because of uncertainties inherent in the methodology and use of WOA18 climatology data on the AXMOC section in areas without XB and Argo observations.

3.4 AMOC and MHT time series

In this subsection, the newly produced AMOC and MHT time series from AXMOC data are presented along with their contributions from geostrophic and Ekman components. The correlations of AMOC and MHT with each component and with estimates from other datasets are also discussed and presented in the supplementary material (Figures S2-S4). Finally, the influence of western and eastern boundaries, and the interior region of the ocean is addressed.

3.4.1 Mean and Seasonal cycle

The estimated mean AMOC (MHT) transport from AXMOC data is 16.34±3.20 Sv (0.73±0.20 PW) between 2007 and 2020. The total AMOC (MHT) transport from AXMOC is composed by an intense equatorward geostrophic transport of 21.74±2.85 Sv (1.15±0.17 PW) and a significant poleward AMOC (MHT) Ekman component of -5.41±1.49 Sv (-0.43±0.11 PW - Figure 10 and Table 1). On a seasonal time scale, the AMOC is stronger in June and weaker in September, and the MHT is more intense in May and weaker in September (Figure 10).

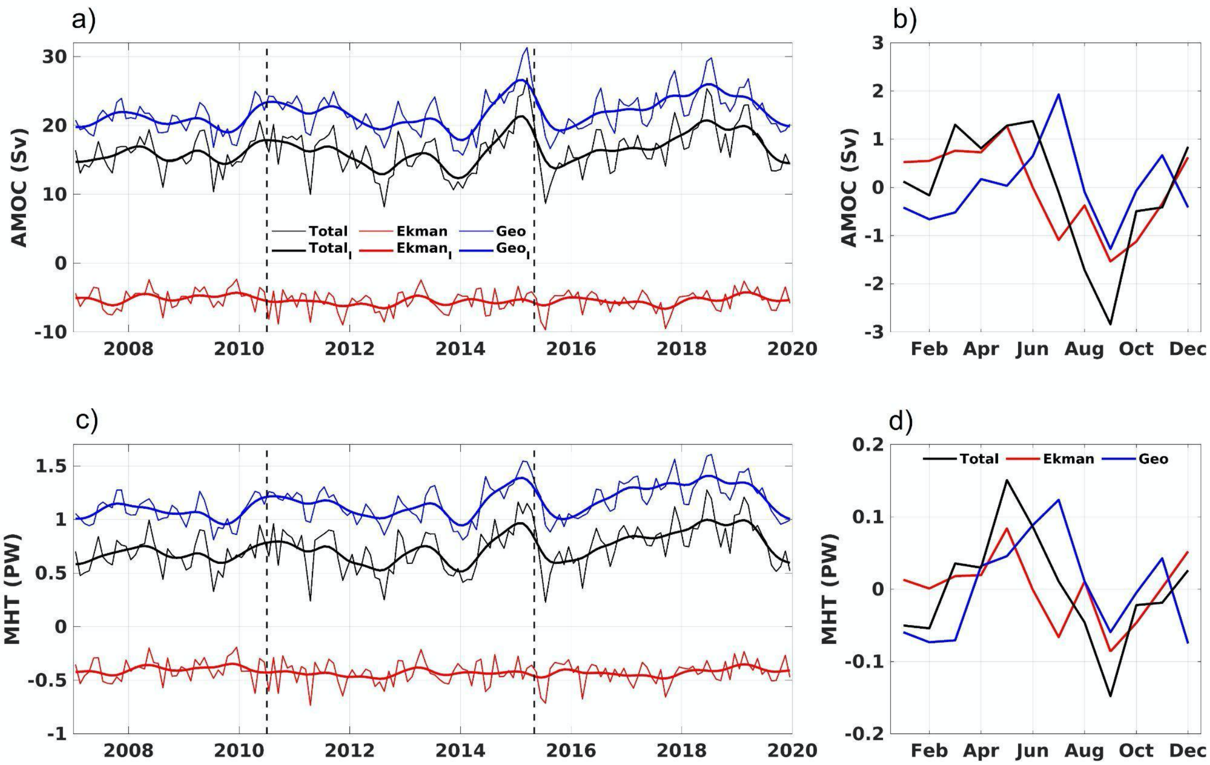

Figure 10. AMOC and MHT time series (left) and associated seasonal cycles (right). AMOC (a, c) and MHT (d, f) time series are divided into Geostrophic (blue lines), Ekman (red lines) and total components (black lines). Solid lines represent the 13-month gaussian filtered component of AMOC and MHT (a and c, respectively). Vertical black dashed lines indicate dates of 06/2010 and 04/2015.

	Total	Geostrophic	Ekman

	AMOC	MHT	AMOC	MHT	AMOC	MHT
AXMOC	**16.34±3.20**	**0.72±0.20**	**21.74±2.85**	**1.15±0.17**	**-5.41±1.49**	**-0.42±0.10**
Dong - 20°S	**16.45±2.13**	**0.62±0.17**	**22.70±1.49**	**1.20±0.09**	**-6.26±1.66**	**-0.58±0.14**
Dong - 25°S	**19.30±2.20**	**0.68±0.17**	**23.00±1.64**	**1.01±0.12**	**-3.70±1.42**	**-0.33±0.13**
ECCOv4r4	**14.11±2.55**	**0.48±0.16**	**19.13±1.84**	**0.87±0.10**	**-5.01±1.38**	**-0.39±0.10**

Table 1. Mean and std values for AMOC (Sv) and MHT (PW) between 2007 and 2019. Total, geostrophic and Ekman components are represented in separated columns.

A comparison of the AMOC (MHT) from AXMOC with that from Dong et al. (2021) synthetic product and the ECCOv4r4 state estimate is shown in the Supplementary Material (Figures S2-S4). The seasonal variations in the AMOC and MHT also have similar patterns to other products which present positive values from April until July and negative values between August and October (Figure S3). Overall, the mean values from AXMOC are within the uncertainty ranges of the other products for both AMOC and MHT (Table 1 and Figure S2). Correlations between AXMOC and individual products are higher for the MHT than for the AMOC: r=0.40 (Dong et al., 2021 - 20°S), r= 0.35 (Dong et al., 2021 - 25°S), and r=0.29 (ECCOv4r4) for the AMOC and r=0.59 (Dong et al., 2021 - 20°S), r= 0.51 (Dong et al., 2021 - 25°S) and r=0.44 (ECCOv4r4) for the MHT. This relatively low correlation between the AXMOC and the other datasets can be related to the amount of variance explained by the geostrophic component of the AMOC/MHT. The variance explained by the geostrophic and Ekman components of the AMOC are similar in Dong et al. (2021) and in the ECCOv4r4 data, approximately 40-60% for each component (Table 2). For the AXMOC, however, the geostrophic component is responsible for most (83%) of the total transport variance. The geostrophic component can also explain the stronger variability of the AMOC/MHT in the AXMOC time series (Table 1).

	AXMOC	Dong - 20°S	Dong - 25°S	ECCOv4r4
Geostrophic	**0.83 (0.77)**	**0.41 (0.33)**	**0.60 (0.44)**	**0.51 (0.58)**
Ekman	**0.17 (0.23)**	**0.59 (0.67)**	**0.40 (0.56)**	**0.49 (0.42)**

Table 2. AMOC variance explained by its geostrophic/Ekman components. The MHT variance explained by its geostrophic/Ekman components are presented in parenthesis.

3.4.2 Interannual variability

The low-pass filtered geostrophic component shows a strong correlation with the total component for both AMOC and MHT (r=0.96 and r=0.97, respectively), thus most of the AMOC and MHT variability in the interannual band is explained by the geostrophic transport (Figure 10). The AMOC decreases significantly when there are intense BC events (Figure 4), as observed during years 2011, 2014, 2015 and 2019. Previous studies indicate that the dominance of geostrophic and Ekman components on the AMOC varies at different latitudes in the South Atlantic. At 35°S, the relative dominance of Ekman and geostrophic components on AMOC and

MHT alternates throughout the time (Dong et al., 2015, 2021). Ekman dominance is also observed at 20°S, but a greater contribution of the geostrophic component is reported at 25°S (Dong et al., 2015). Results from the AXMOC transect corroborate with Dong et al. (2015, 2021) 25°S estimates on the overall dominance of the geostrophic component (correlations of 0.94/0.92) over the Ekman contribution (correlations of 0.15/0.21) for AMOC/MHT transports. In addition, high correlations ($r > 0.95$) are observed between the total AMOC and MHT time series at 22.5°S, as well as for the geostrophic and Ekman components. Other studies have also observed high correlations between the AMOC and MHT time series at various latitudes in both the North and South Atlantic (Dong et al., 2009, 2015, 2021; Johns et al., 2011), showing the dominance of velocity variability over temperature variability in the MHT time series.

The variability observed in the AXMOC time series appears to have changed since 2014, when the interannual to decadal variability strengthened, driving an increase in the AMOC by approximately 2 Sv (Figure 10). Dong et al. (2021) also observed a moderate interannual AMOC increase at 25°S on both total and geostrophic transports but only after 2017 (Figure S4). Due to the short extent of our time series we cannot draw any conclusion about the long term changes of the AMOC. Next, we will compare AXMOC time series with the decadal estimates of Cainzos et al. (2022), Dong et al. (2021) and ECCOv4r4, analyze it in the context of decadal variability.

3.4.3 Decadal variability

We estimated the AMOC transport using the WOCE/GO-SHIP data applying the same methodology used in the AXMOC. For the two WOCE sections of Apr/2009 and Mar/2018, the AMOC strength was 22.00 Sv and 18.59 Sv, respectively. The corresponding AMOC transports from the AXMOC data are 24.8 Sv and 19.96 Sv. The AXMOC estimates differ from WOCE estimates by +2.80 Sv and -0.63 Sv, respectively. Therefore, we estimate the error due to spatial mapping and data availability to be of ~ 2 Sv. To compare the decadal variability of AXMOC and other products, we used the 2010-2019 mean AMOC. The AXMOC mean of 2010-2019 AMOC value is 16.58±3.41 Sv, in comparison to 16.29±2.14 Sv (20°S) and 19.26±2.30 Sv (25°S) for Dong et al. (2021) and significantly smaller value for ECCOv4r4 of 13.75±2.39 Sv. Relative to the previous decade, Dong et al. (2021) observed contrasting changes such as a slight increase (0.19 Sv) in 25°S and a slight decrease (-0.58 Sv) in 20°S, while ECCOv4r4 showed an AMOC decrease of 1.19 Sv between the two periods.

Results from the Cainzos et al. (2022) adjoint model show a mean AMOC decrease of ~ 1.6 Sv from 2000-2009 to 2010-2019, 19.70±1.20 Sv to 18.10±1.10 Sv, respectively, which falls within the uncertainties of the methodology applied. The difference from Cainzos et al. (2022) and the AXMOC decadal means is also within 2 Sv. In addition, Cainzos et al. (2022) estimated a slightly higher mean AMOC of 19.80±1.00 Sv for the 1990-1999 decade. Therefore, our results corroborate to the conclusions drawn by Cainzos et al. (2022) that no significant changes were observed in the AMOC near 22.5S in the past three decades.

3.4.4 Boundary and Interior contributions

Finally, to understand if the specific areas of the AXMOC transect influence the AMOC at 22.5°S, we compare its geostrophic component to the transport in the upper 1000 m near the western boundary (from western coast to 38°W), interior of the section (from 39°W to 3°E), and near the eastern boundary (from 3°E to eastern coast). The AMOC geostrophic transport has a higher correlation with the western ($r=0.69$) than with the eastern boundary ($r=0.41$) (Figure 11).

This is different to what was observed at 34.5°S, where the eastern boundary contributes more to the AMOC variability than the western boundary (Meinen et al., 2018). A possible explanation for this difference is the increased influence of the Agulhas leakage in the eastern boundary close to 34.5°S. In addition, the interior and eastern boundary transports show a significant inverse relationship (r= -0.62) and compensation between the two regions (Figure 10). The anomalous strengthening of the AMOC in 2015 (Figure 10a), where the geostrophic contribution reached values close to 25 Sv, is due to a concurrent intensification of equatorward circulation on both boundaries (Figure 11). Apart from that, most of the AMOC anomalous intensification events are caused by the changes in only one of the boundaries.

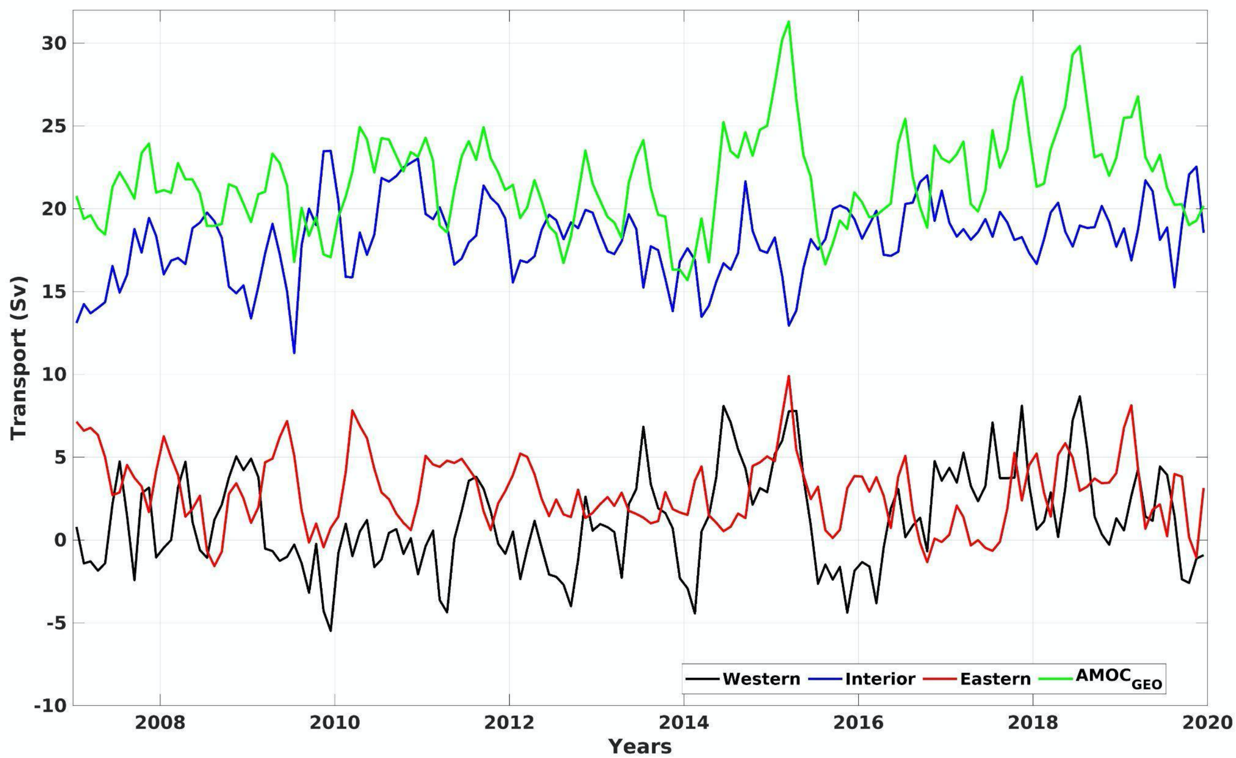

Figure 11. Upper 1000 m volume transport for western boundary (black), eastern boundary (red) and interior (blue) from the AXMOC data. The geostrophic AMOC transport is shown by a green line.

4 Conclusions

We use a combination of Argo and XBT data to produce the first estimate of the AMOC and MHT at 22.5°S. The current in situ coverage composed by Argo and XBT data is sufficient for the calculation of AMOC and MHT at 22.5°S from 2007 onwards. The altimetry optimized mapping methodology proved to be efficient in capturing westward wave propagation, boundary currents, AMOC and MHT. Near the western boundary, the first continuous long-term monthly transport of the highly variable BC was produced due to the good coverage by the high-density XBT transect implemented since 2004. BC volume transport anomalies observed in 2009/2010 are consistent with Goes et al. (2019). These and other BC anomalies (e.g., 2014 and 2016) are captured by AXMOC data and observed in the SLA time series at the western boundary.

Some physical properties (T, S and $\boldsymbol{\gamma}$) of the main water masses in the South Atlantic were also analyzed here, and are consistent with earlier studies (Hernandez-Guerra et al., 2019; Liu & Tanhua, 2021; Stramma et al., 2004 and Talley, 2011). The AABW is limited by neutral density lines $\boldsymbol{\gamma}> 28.10\ kg\ m^{-3}$, while the NADW flows between 27.84 and 28.10 $kg\ m^{-3}$. At 22.5°S, both AABW and NADW are constrained west of 30°W by local topography and the latter is divided into two cores flowing along the western and eastern boundaries near depths of 2500 m. In the uppermost isopycnal layer ($\boldsymbol{\gamma} < 27.23\ kg\ m^{-3}$), an important area for AMOC variability, AXMOC and WOCE data have a good agreement. The AXMOC data yields volume transports of 18.74 Sv and 19.55 Sv for Apr/2009 and Mar/2018, respectively, while WOCE data yields volume transports of 20.34 Sv and 17.89 Sv for the same period, respectively. The integrated isopycnal transport obtained by AXMOC is robust and an uncertainty of ~2 Sv in the AMOC transport due to the mapping errors is estimated from independent observations.

Seasonality in the AMOC and MHT time series shows a good agreement between all the products considered, with annual amplitudes of 4 Sv and 0.3 PW, respectively. Stronger AMOC/MHT values are observed in Jan-Jul and weaker values are observed in Aug-Dec. The geostrophic and Ekman contributions are in-phase and reinforce this variability. The interannual variability in the geostrophic component of the AMOC from AXMOC is more intense than those from other products, probably because of the improved resolution near the western boundary. The western boundary currents appear to have the largest contribution to the AMOC/MHT variability (r=0.62). Our results show sharp declines in the AMOC and MHT during positive BC anomalies (intense southward transport), such as in 2014, end of 2015 and 2019. Also, a period of more frequent negative values of total and geostrophic transports in both AMOC and MHT is observed between 2010 and 2015. Further analysis is needed, but the basin wide extent of this event suggests that they are related to large scale modes of variability in the South Atlantic. Finally, AXMOC data could also be used to assess freshwater flux anomalies in the South Atlantic and link it to a possible bi-stability of the AMOC (Rahmstorf et al., 1996; Stommel, 1961).

The observed AMOC (MHT) mean transport was 16.34±3.20 Sv (0.73±0.20 PW) between 2007 and 2020, and positive anomalies became more frequent after 2015 (Figures 10 and S4), although this trend was not statistically significant given the uncertainty of our estimates. The AMOC is projected to weaken according to the IPCC projections for the 21st century (Collins et al., 2019; Fox-Kemper et al., 2021; Lee et al., 2021). The future AMOC weakening has been linked to a BC intensification (Marcello et al., 2023), and our results corroborate with this link between the BC and the AMOC at 22.5°S, thus the continuation of this monitoring effort at 22.5°S might provide early evidence for changes in the AMOC in the Northern Hemisphere.

The availability of multi-decadal data of tide gauges on both sides of the basin can in the future be used to complement, validate, and extend the DH field on the boundaries. Deep Argo profilers and/or PIES stations have the potential to improve data availability in the South Atlantic deep ocean (>2000 m), and could replace climatological data in the deep ocean, since their spatial and temporal coverage has been increasing significantly. The proposed methodology can be replicated to include other latitudes in the Atlantic basin where the Argo and XBT coverage would permit a long term AMOC and MHT estimations. This expansion to other latitudes would be beneficial for the scientific community once an integrated assessment of the long-term variability of AMOC and MHT can be performed using a single methodology. Currently, the

AMOC has been monitored at different latitudes, however, each program has different limitations and uncertainties, which impacts the comparison and integration of different time series (Chidichimo et al., 2023). In addition, our methodology allows more frequent updates of the AMOC since Argo and XBT data are publicly available in near-real time, as opposed to mooring data from existing AMOC arrays. Therefore, our methodology, if expanded in time and space, could positively impact the prediction capability of different events (e.g., coastal sea level and hurricane season outlook).

Acknowledgments

This research was carried out in part under the auspices of the Cooperative Institute for Marine and Atmospheric Studies, a cooperative institute of the University of Miami and the National Oceanic and Atmospheric Administration (NOAA), cooperative agreement NA 20OAR4320472, and was supported by the Ocean Observing and Monitoring Division of the NOAA Climate Program Office and by NOAA's Atlantic Oceanographic and Meteorological Laboratory (AOML). MG and DLV were also supported by the National Oceanic and Atmospheric Administration (NOAA) Climate Variability and Predictability program (grant number NA20OAR4310407).

Open Research

The following data used for this study can be downloaded from: XBT transect data (http://www.aoml.noaa.gov/phod/hdenxbt/); Argo profile data (https://www.nodc.noaa.gov/argo/ and https://www.seanoe.org/data/00311/42182/ - http://doi.org/10.17882/42182); Argo/altimetry climatological ADT product (http://apdrc.soest.hawaii.edu/projects/argo/); the delayed-time satellite altimetry maps (http://marine.copernicus.eu); ERA5 atmospheric reanalysis (https://cds.climate.copernicus.eu); MOC and MHT synthetic time series (https://www.aoml.noaa.gov/phod/samoc_argo_altimetry/data_moc.php); WOA18 (https://www.ncei.noaa.gov/access/world-ocean-atlas-2018/); RG Argo (https://sio-argo.ucsd.edu/RG_Climatology.htm); ECCOv4r4 (https://www.ecco-group.org/products-ECCO-V4r4.html); WOCE (https://cchdo.ucsd.edu) for cruises A095 in 2009 (https://cchdo.ucsd.edu/cruise/740H20090307) and in 2018 (https://cchdo.ucsd.edu/cruise/740H20180228).

References

Ablain, M., Meyssignac, B., Zawadzki, L., Jugier, R., Ribes, A., Spada, G., et al. (2019). Uncertainty in satellite estimates of global mean sea-level changes, trend and acceleration. *Earth Syst. Sci. Data*, 11, 1189–1202. doi:10.5194/essd-11-1189-2019.

Argo (2020). Argo float data and metadata from Global Data Assembly Centre (Argo GDAC). SEANOE. doi:10.17882/42182

Arnault, S., Gourdeau, L., & Menard, Y. (1992). Comparison of the altimetric signal with in situ measurements in the tropical Atlantic Ocean. Deep Sea Research Part A. Oceanographic Research Papers, 39(3-4), 481-499. doi:10.1016/0198-0149(92)90084-7

Barron, C. N., Kara, A. B., & Jacobs, G. A. (2009). Objective estimates of westward Rossby wave and eddy propagation from sea surface height analyses. Journal of Geophysical Research Oceans, 114(C3), 496-510. doi:10.1029/2008JC005044

Bellomo, K., Angeloni, M., Corti, S., & von Hardenberg, J. (2021). Future climate change shaped by inter-model differences in Atlantic meridional overturning circulation response. Nature Communications, 12(1), 1-10. doi:10.1038/s41467-021-24015-w

Berger, W. H., Wefer, G., Richter, C., Lange, C. B., Giraudeau, J., Hermelin, O., & Party, S. S. (1998). 17. The Angola-Benguela upwelling system: Paleoceanographic synthesis of shipboard results from leg 1751. In Proceedings Ocean Drilling Program, Initial Reports (Vol. 175, pp. 505-531). doi:10.2973/odp.proc.ir.175.117.1998

Biastoch, A., Böning, C. W., Schwarzkopf, F. U. & Lutjeharms, J. R. E. (2009), Increase in Agulhas leakage due to poleward shift of Southern Hemisphere westerlies, Nature, 462(7272), 495-498. doi:10.1038/nature08519.

Broecker, W. S. (2003). Does the trigger for abrupt climate change reside in the ocean or in the atmosphere? Science, 300(5625), 1519-1522. doi:10.1126/science.1083797

Buckley, M. W., & Marshall, J. (2016). Observations, inferences, and mechanisms of the Atlantic Meridional Overturning Circulation: A review. Reviews of Geophysics, 54(1), 5-63. doi:10.1002/2015RG000493

Caínzos, V., Hernández-Guerra, A., McCarthy, G. D., McDonagh, E. L., Cubas Armas, M., & Pérez-Hernández, M. D. (2022). Thirty years of GOSHIP and WOCE data: Atlantic overturning of mass, heat, and freshwater transport. Geophysical Research Letters, 49(4), e2021GL096527. doi:10.1029/2021GL096527

Calado, L., Gangopadhyay, A., & Da Silveira, I. C. A. (2008). Feature-oriented regional modeling and simulations (FORMS) for the western South Atlantic: Southeastern Brazil region. Ocean Modelling, 25(1-2), 48-64. doi:10.1016/j.ocemod.2008.06.007

Chang, P., Zhang, R., Hazeleger, W., Wen, C., Wan, X., Ji, L., et al. (2008), Oceanic link between abrupt changes in the North Atlantic Ocean and the African monsoon, Nature Geoscience, 1(7), 444-448. doi:10.1038/ngeo218.

Chidichimo, M.P., Perez, R.C., Speich, S., Kersalé, M., Sprintall, J., Dong, S., et al. (2023), Energetic overturning flows, dynamic interocean exchanges, and ocean warming observed in the South Atlantic. Communications Earth Environment 4, 10. doi:.1038/s43247-022-00644-x

Collins, M., Sutherland, M., Bouwer L., Cheong, S. M., Frölicher, T., Jacot Des Combes, H., et al. (2019). Extremes, Abrupt Changes and Managing Risk. In Pörtner H. O., Roberts, D. C., Masson-Delmotte, V., Zhai, P., Tignor, M., Poloczanska, E., et al. (eds.), IPCC Special Report on the Ocean and Cryosphere in a Changing Climate. Cambridge University Press, Cambridge, UK and New York, NY, pp. 589-655. doi:10.1017/9781009157964.008.

Conway, T. M., Palter, J. B., & de Souza, G. F. (2018). Gulf Stream rings as a source of iron to the North Atlantic subtropical gyre. Nature Geoscience, 11(8), 594-598. doi:10.1038/s41561-018-0162-0

Da Silveira, I. C. A., Lima, J. A. M., Schmidt, A. C. K., Ceccopieri, W., Sartori, A., Francisco, C. P. F., & Fontes, R. F. C. (2008). Is the meander growth in the Brazil Current system off Southeast Brazil due to baroclinic instability? Dynamics of Atmospheres and Oceans, 45(3-4), 187-207. doi:10.1016/j.dynatmoce.2008.01.002

Desbruyères, D., Chafik, L. & Maze, G. (2021). A shift in the ocean circulation has warmed the subpolar North Atlantic Ocean since 2016. Commun Earth Environ 2, 48. doi:/10.1038/s43247-021-00120-y.

de Vries, P., & Weber, S. L. (2005). The Atlantic freshwater budget as a diagnostic for the existence of a stable shut down of the meridional overturning circulation. Geophysical Research Letters, 32(9), L09606. doi:10.1029/2004GL021450

Dong, S., Garzoli, S., Baringer, M., Meinen, C., & Goni, G. (2009). Interannual variations in the Atlantic meridional overturning circulation and its relationship with the net northward heat transport in the South Atlantic. Geophysical Research Letters, 36(20). doi: 10.1029/2009GL039356

Dong, S., Goni, G., & Bringas, F. (2015). Temporal variability of the South Atlantic meridional overturning circulation between 20 S and 35 S. Geophysical Research Letters, 42(18), 7655-7662. doi:10.1002/2015GL065603

Dong, S., Goni, G., Domingues, R., Bringas, F., Goes, M., Christophersen, J., & Baringer, M. (2021). Synergy of in situ and satellite ocean observations in determining meridional heat transport in the Atlantic Ocean. Journal of Geophysical Research: Oceans, 126(4). doi: 10.1029/2020JC017073

Durgadoo, J. V., Loveday, B. R., Reason, C. J., Penven, P. & Biastoch, A. (2013), Agulhas leakage predominantly responds to the Southern Hemisphere westerlies, Journal of Physical Oceanography, 43(10), 2113-2131. doi:10.1175/JPO-D-13-047.1.

Forget, G., Campin, J.-M., Heimbach, P., Hill, C. N., Ponte, R. M. & Wunsch, C. (2015). ECCO version 4: An integrated framework for non-linear inverse modeling and global ocean state estimation. Geoscientific Model Development, 8. 3071-3104. doi:10.5194/gmd-8-3071-2015

Fox-Kemper, B., Hewitt, H.T., Xiao, C., Aðalgeirsdóttir, G., Drijfhout, S.S., Edwards, T.L., et al. (2021). Ocean, Cryosphere and Sea Level Change. In Masson-Delmotte, V., P. Zhai, A. Pirani, S.L. Connors, C. Péan, S. Berger, et al. (eds.), Climate Change 2021: The Physical Science Basis. Contribution of Working Group I to the Sixth Assessment Report of the Intergovernmental Panel on Climate Change. Cambridge University Press, Cambridge, United Kingdom and New York, NY, USA, pp. 1211–1362. doi:10.1017/9781009157896.011

Frajka-Williams, E., Ansorge, I. J., Baehr, J., Bryden, H. L., Chidichimo, M. P., Cunningham, S. A., et al. (2019), Atlantic Meridional Overturning Circulation: Observed Transport and Variability, Frontiers in Marine Science, 6(260). doi:10.3389/fmars.2019.00260.

Garcia H.E., Boyer, T.P., Baranova, O.K., Locarnini, R.A., Mishonov, A.V., Grodsky, A., et al. (2019). World Ocean Atlas 2018: Product Documentation. A. Mishonov, Technical Editor. Retrieved from https://www.ncei.noaa.gov/sites/default/files/2020-04/woa18documentation.pdf

Garzoli, S. L., & Gordon, A. L. (1996). Origins and variability of the Benguela Current. Journal of Geophysical Research: Oceans, 101(C1), 897-906. doi:10.1029/95JC03221

Garzoli, S., Baringer, M., Dong, S., Perez, R. & Yao, Q. (2013), South Atlantic meridional fluxes, Deep Sea Res., Part I, 71, 21–32. doi:10.1016/ j.dsr.2012.09.003

Goes, M., Urban, N. M., Tonkonojenkov, R., Haran, M., Schmittner, A., & Keller, K. (2010). What is the skill of ocean tracers in reducing uncertainties about ocean diapycnal mixing and projections of the Atlantic Meridional Overturning Circulation? Journal of Geophysical Research: Oceans, 115(C12). doi:10.1029/2010JC006407

Goes, M., Wainer, I. & Signorelli, N. (2014). Investigation of the causes of historical changes in the subsurface salinity minimum of the South Atlantic. Journal of Geophysical Research-Oceans, 119(9), 5654-5675. doi:10.1002/2014JC009812.

Goes, M., Goni, G., & Dong, S. (2015). An optimal XBT-based monitoring system for the South Atlantic meridional overturning circulation at 34° S. Journal of Geophysical Research: Oceans, 120(1), 161-181. doi:10.1002/2014JC010202

Goes, M., Christophersen, J., Dong, S., Goni, G., & Baringer, M. O. (2018). An updated estimate of salinity for the Atlantic ocean sector using temperature–salinity relationships. Journal of Atmospheric and Oceanic Technology, 35(9), 1771-1784. doi:10.1175/JTECH-D-18-0029.1

Goes, M., Cirano, M., Mata, M. M., & Majumder, S. (2019). Long-Term Monitoring of the Brazil Current Transport at 22° S From XBT and Altimetry Data: Seasonal, Interannual, and Extreme Variability. Journal of Geophysical Research: Oceans, 124(6), 3645-3663. doi:10.1029/2018JC014809

Goes, M., Murphy, L. N. & Clement, A.C. (2019b). The stability of the AMOC during Heinrich events is not dependent on the AMOC strength in an Intermediate Complexity Earth System model ensemble. Paleoceanography and Paleoclimatology, 34(8),1359-1374. doi:10.1029/2019PA003580.

Goes, M., Goni, G., Dong, S., Boyer, T., & Baringer, M. (2020). The complementary value of XBT and Argo observations to monitor ocean boundary currents and meridional heat and volume transports: A case study in the Atlantic Ocean. Journal of Atmospheric and Oceanic Technology, 37(12), 2267-2282. doi:10.1175/JTECH-D-20-0027.1

Hernández-Guerra, A., Talley, L. D., Pelegrí, J. L., Vélez-Belchí, P., Baringer, M. O., Macdonald, A. M., & McDonagh, E. L. (2019). The upper, deep, abyssal and overturning circulation in the Atlantic Ocean at 30 S in 2003 and 2011. Progress in Oceanography, 176, 102136. doi:10.1016/j.pocean.2019.102136

Herrford, J., Brandt, P., Kanzow, T., Hummels, R., Araujo, M., & Durgadoo, J. V. (2021). Seasonal variability of the Atlantic Meridional Overturning Circulation at 11 S inferred from bottom pressure measurements. Ocean Science, 17(1), 265-284. doi:10.5194/os-17-265-2021

Hersbach, H, Bell, B, Berrisford, P, et al. (2020). The ERA5 global reanalysis, Q J R Meteorol Soc., 146, 1999– 2049. doi:10.1002/qj.3803

Hummels, R., Brandt, P., Dengler, M., Fischer, J., Araujo, M., Veleda, D. & Durgadoo, J. V. (2015), Interannual to decadal changes in the western boundary circulation in the Atlantic at 11°S, Geophysical Research Letters, 42(18), 7615-7622. doi:10.1002/2015GL065254.

Johns, W. E., Baringer, M. O., Beal, L. M., Cunningham, S. A., Kanzow, T., Bryden, H. L., ... & Curry, R. (2011). Continuous, array-based estimates of Atlantic Ocean heat transport at 26.5 N. Journal of Climate, 24(10), 2429-2449. doi:10.1175/2010JCLI3997.1

Kersalé, M., Meinen, C. S., Perez, R. C., Le Henaff, M., Valla, D., Lamont, T., et al. (2020). Highly Variable Upper and Abyssal Overturning Cells in the South Atlantic, Science Advances, 6(32). doi:10.1126/sciadv.aba7573.

Koltermann, K.P., Gouretski, V.V. & Jancke, K. (2011). Hydrographic Atlas of the World Ocean Circulation Experiment (WOCE). Volume 3: Atlantic Ocean (eds. M. Sparrow, P. Chapman and J. Gould). International WOCE Project Office, Southampton, UK, ISBN 090417557X.

Koseki, S., Giordani, H., & Goubanova, K. (2019). Frontogenesis of the Angola–Benguela frontal zone. Ocean Science, 15(1), 83-96. doi:10.5194/os-15-83-2019

Lee, J.-Y., Marotzke, J., Bala, G., Cao, L., Corti, S., Dunne, J.P., et al. (2021). Future Global Climate: Scenario-Based Projections and Near- Term Information. In Masson-Delmotte, V., Zhai, P., Pirani, A., Connors, S.L., Péan, C., Berger, S., et al. (eds.), Climate Change 2021: The Physical Science Basis. Contribution of Working Group I to the Sixth Assessment Report of the Intergovernmental Panel on Climate Change. Cambridge University Press, Cambridge, United Kingdom and New York, NY, USA, pp. 553–672. doi:10.1017/9781009157896.006

Lima, M. O., Cirano, M., Mata, M. M., Goes, M., Goni, G., & Baringer, M. (2016). An assessment of the Brazil Current baroclinic structure and variability near 22° S in Distinct Ocean Forecasting and Analysis Systems. Ocean Dynamics, 66(6), 893-916. doi:10.1007/s10236-016-0959-6

Little, C. M., Piecuch, C. G., & Ponte, R. M. (2017), On the relationship between the meridional overturning circulation, alongshore wind stress, and United States East Coast sea level in the Community Earth System Model Large Ensemble. J. Geophys. Res., 112, 4554–4568. doi:10.1002/2017JC012713

Liu, M., & Tanhua, T. (2021). Water masses in the Atlantic Ocean: characteristics and distributions. Ocean Science, 17(2), 463-486. doi:10.5194/os-17-463-2021

Locarnini, M. M., Mishonov, A. V., Baranova, O. K., Boyer, T. P., Zweng, M. M., Garcia, H. E., et al. (2018). World ocean atlas 2018, volume 1: Temperature. A. Mishonov, Technical Editor.

NOAA Atlas NESDIS 81, 52pp. Retrieved from https://www.ncei.noaa.gov/sites/default/files/2020-04/woa18_vol1.pdf

Lopez, H., Dong, S., Lee, S.-K., & Goni, G. (2016). Decadal Modulations of Interhemispheric Global Atmospheric Circulations and Monsoons by the South Atlantic Meridional Overturning Circulation. J. Clim., 29(5), 1831-1851. doi:10.1175/JCLI-D-15-0491.1

Majumder, S., & Schmid, C. (2018). A study of the variability in the Benguela Current volume transport, Ocean Sci., 14, 273–283. doi:10.5194/os-14-273-2018.

Marcello, F., Tonelli, M., Ferrero, B., & Wainer, I. (2023). Projected Atlantic overturning slow-down is to be compensated by a strengthened South Atlantic subtropical gyre. Commun Earth Environ. 4, 92. doi:10.1038/s43247-023-00750-4

Mata, M. M., Cirano, M., Caspel, M. R. V., Fonteles, C. S., Gõni, G., & Baringer, M. (2012). Observations of Brazil Current baroclinic transport near 22 S: variability from the AX97 XBT transect. Exchanges, 58, 5-10.

McCarthy, G. D., Brown, P. J., Flagg, C. N., Goni, G., Houpert, L., Hughes, C. W., et al. (2020), Sustainable Observations of the AMOC: Methodology and Technology, Reviews of Geophysics, 58(1). doi:10.1029/2019RG000654.

Meinen, C. S., Speich, S., Piola, A. R., Ansorge, I., Campos, E., Kersalé, M., et al. (2018). Meridional overturning circulation transport variability at 34.5 S during 2009–2017: Baroclinic and barotropic flows and the dueling influence of the boundaries. Geophysical Research Letters, 45, 4180-4188. doi:10.1029/2018GL077408

Pereira, J., Gabioux, M., Almeida, M. M., Cirano, M., Paiva, A. M., & Aguiar, A. L. (2014). The bifurcation of the western boundary current system of the South Atlantic Ocean. Brazilian Journal of Geophysics, 32(2), 241-257. doi:10.22564/rbgf.v32i2.456

Pita, I. I., Cirano, M., & Mata, M. M. (2020). An assessment of Brazil Current surface velocity and associated transport near 22° S: XBT and altimetry data. Regional Studies in Marine Science, 35, 101197. doi:10.1016/j.rsma.2020.101197

Polito, P. S., & Liu, W. T. (2003). Global characterization of Rossby waves at several spectral bands. Journal of Geophysical Research: Oceans, 108(C1). doi:10.1029/2000JC000607

Pujol, M. I., Faugère, Y., Taburet, G., Dupuy, S., Pelloquin, C., Ablain, M., & Picot, N. (2016). DUACS DT2014: the new multi-mission altimeter data set reprocessed over 20 years. Ocean Science, 12(5), 1067-1090. doi:10.5194/os-12-1067-2016

Rahmstorf, S. (1996). On the freshwater forcing and transport of the Atlantic thermohaline circulation. Climate Dynamics, 12(12), 799–811. doi:10.1007/s003820050144

Reid, J.L., 1989. On the total geostrophic circulation of the South Atlantic Ocean: Flow patterns, tracers, and transports. Prog. Oceanogr. 23, 149–244. doi:10.1016/0079-6611(89)90001-3

Rhein, M. (2019). Taking a close look at ocean circulation. Science, 363(6426), 456-457. doi:10.1126/science.aaw3111

Roemmich, D. & Gilson, J. (2009) The 2004-2008 mean and annual cycle of temperature, salinity, and steric height in the global ocean from the Argo Program. Progress in Oceanography, 82, 81-100. doi:10.1016/j.pocean.2009.03.004

Roemmich, D., Johnson, G.C., Riser, S., Davis, R., Gilson, J., Owens, W.B., Garzoli, S.L., Schmid, C., & Ignaszewski, M. (2009). The Argo Program: Observing the global ocean with profiling floats. Oceanography, 22(2), 34–43. doi:10.5670/oceanog.2009.36.

Stommel, H. (1961), Thermohaline Convection with Two Stable Regimes of Flow, Tellus, 13(2), 224-230. doi:10.1111/j.2153-3490.1961.tb00079.x.

Stramma, L., & England, M. (1999). On the water masses and mean circulation of the South Atlantic Ocean. Journal of Geophysical Research: Oceans, 104(C9), 20863-20883. doi:10.1029/1999JC900139

Stramma, L., Kieke, D., Rhein, M., Schott, F., Yashayaev, I., & Koltermann, K. P. (2004). Deep water changes at the western boundary of the subpolar North Atlantic during 1996 to 2001, Deep Sea Res., 51, 1033–1056. doi:10.1016/j.dsr.2004.04.001

Strub, P. T., James, C., Combes, V., Matano, R. P., Piola, A. R., Palma, E. D., et al. (2015). Altimeter-derived seasonal circulation on the southwest Atlantic shelf: 27°–43° S. Journal of Geophysical Research: Oceans, 120(5), 3391-3418. doi:10.1002/2015JC010769.

Talley, L. D. (2011). Descriptive physical oceanography: an introduction. Academic press. 6th ed, pp. 560.

Todd, R. E., Chavez, F. P., Clayton, S., Cravatte, S., Goes, M., Graco, M., et al. (2019). Global perspectives on observing ocean boundary current systems. Frontiers in Marine Science, 6(423). doi: 10.3389/fmars.2019.00423.

Veitch, J. A., Florenchie, P., & Shillington, F. A. (2006). Seasonal and interannual fluctuations of the Angola–Benguela Frontal Zone (ABFZ) using 4.5 km resolution satellite imagery from 1982 to 1999. International Journal of Remote Sensing, 27(05), 987-998. doi:10.1080/01431160500127914

Volkov, D. L., Baringer, M., Smeed, D., Johns, W., & Landerer, F. W. (2019). Teleconnection between the Atlantic meridional overturning circulation and sea level in the Mediterranean Sea. Journal of climate, 32(3), 935-955. doi:10.1175/JCLI-D-18-0474.1

Weijer, W., Cheng, W., Drijfhout, S. S., Fedorov, A. V., Hu, A., Jackson, L. C., et al. (2019). Stability of the Atlantic meridional overturning circulation: A review and synthesis. Journal of Geophysical Research: Oceans, 124(8), 5336–5375. doi:10.1029/2019JC015083

Zweng, M. M., Seidov, D., Boyer, T. P., Locarnini, M., Garcia, H. E., Mishonov, A. V., et al. (2019). World ocean atlas 2018, volume 2: Salinity. A. Mishonov, Technical Editor, NOAA Atlas NESDIS 82, 50pp. Retrieved from https://www.ncei.noaa.gov/sites/default/files/2022-06/woa18_vol2.pdf

An ARGO and XBT observing system for the Atlantic Meridional Overturning Circulation and Meridional Heat Transport (AXMOC) at 22.5ºS

I. Pita[1,2,3], M. Goes[2,3], D. L. Volkov[2,3], S. Dong[3], G. Goni[3] and M. Cirano[4]

[1]Rosenstiel School, University of Miami, Miami, FL, United States of America.

[2]Cooperative Institute for Marine and Atmospheric Studies, University of Miami, Miami, FL, United States of America.

[3]Atlantic Oceanographic and Meteorological Laboratory, NOAA, United States of America.

[4]Department of Meteorology, Institute of Geosciences, Federal University of Rio de Janeiro (UFRJ), Brazil

Corresponding author: Ivenis Pita (ivenis.pita@noaa.gov)

Key Points:

- First in situ based Atlantic Meridional Overturning Circulation and Meridional Heat Transport time series estimation at 22.5ºS
- Mapping methodology used is robust and captures the climatological pattern for Atlantic Meridional Overturning Circulation
- Western boundary system drives interannual Atlantic Meridional Overturning Circulation variability, followed by eastern boundary system

Abstract

Changes in the Atlantic Meridional Overturning Circulation (AMOC) and associated Meridional Heat Transport (MHT) can affect climate and weather patterns, regional sea levels, and ecosystems. However, despite its importance, direct observations of the AMOC are still limited spatially and temporally, particularly in the South Atlantic. The main goal of this study is to implement a cost-effective trans-basin section to estimate for the first time the AMOC at 22.5°S, using only sustained ocean observations. For this, an optimal mapping method that minimizes the difference between surface in-situ dynamic height and satellite altimetry was developed to retrieve monthly temperature and salinity profiles from Argo and XBT data along the 22.5°S section. The mean AMOC and MHT for 22.5°S were estimated as 15.55±2.81 Sv and 0.68±0.18 PW, respectively, and are stronger during austral fall/winter and weaker in spring. The high-resolution XBT data available at the western boundary are vital for capturing the highly variable Brazil Current, and our section shows a significant improvement when compared to Argo database. The mean values, interannual and seasonal time series of AMOC and MHT were compared with other products. At 22.5S the North Atlantic Deep Water is divided into two cores that flow along both western and eastern boundaries near 2500 m depth. Our results suggest a greater influence of western boundary system on the AMOC variability at 22.5°S; highlight the importance of high resolution in situ data for AMOC estimations; and contribute for a better understanding of AMOC and MHT variability in the South Atlantic.

Plain Language Summary

The Atlantic Meridional Overturning Circulation (AMOC) is an ocean currents system associated with large-scale meridional transport of heat (MHT) and nutrients that can modulate climate, weather and ecosystems globally. In-situ measurements of the AMOC are still limited in space and time, particularly in the South Atlantic. Previous studies used synthetic methodologies based on statistical relationships between satellite sea surface height and in-situ temperature and salinity profiles to calculate AMOC in different latitudes. However, these methodologies are constrained by how good and stable these relationships are. Our new methodology obtains monthly AMOC and MHT estimates at 22.5°S by gridding scattered profiles along a reference section using optimal mapping parameters based on a sea level comparison to satellite data. The methodology can resolve the western boundary current, westward propagating sea level features and near coastal sea level variability. At 22.5°S the North Atlantic Deep Water is divided into two southward cores along the western and eastern boundaries near 2500 m depth. The AMOC is stronger during austral fall/winter and weaker in spring, and its interannual variability is linked primarily to the western boundary current changes. This work provides evidence that an AMOC monitoring section can be achieved by using solely sustained observations.

1 Introduction

The Atlantic Meridional Overturning Circulation (AMOC) is the zonal integral of the complex three-dimensional circulation, characterized by an upper cell connected to the deep convection in the North Atlantic subpolar region, and a lower or abyssal cell originated in the marginal seas off Antarctica (Broeker, 2003; Buckley and Marshall, 2016). The AMOC controls the distribution of heat and energy, tracers, and nutrients across the basin and links the timescales of heat uptake and carbon storage (Conway et al., 2018; Collins et al., 2019; Todd et al., 2019). The IPCC projections for the 21st century predict a significant weakening of the AMOC, which if it happens, will result in global and regional impacts on climate, weather, sea level, and ecosystems (Collins et al., 2019; Fox-Kemper et al., 2021; Lee et al., 2021). Theoretical and climate models suggest that the stability of the AMOC is dependent on the oceanic freshwater budget in the South Atlantic (de Vries & Weber, 2005; Stommel, 1961; Weijer et al., 2019). Depending on the sign of the freshwater transport into the South Atlantic, the AMOC may present a hysteresis behavior, in which a collapsed AMOC could be sustained even without an anomalous freshwater forcing (Rahmstorf et al., 1996; Stommel, 1961). Because the net freshwater transport across 35°S in the South Atlantic is southward (Garzoli et al., 2013), a weakening of the AMOC would increase the freshwater transport into the Atlantic, causing negative feedback to the AMOC recovery (Goes et al., 2019b). In addition, the AMOC is one of the main sources of uncertainties in climate model projections (Bellomo et al., 2021), which highlights the importance of sustained observational data for a more robust AMOC predictability. Therefore, the monitoring, hindcasting, and future projections of the AMOC variability are crucial for a better understanding of the Earth system dynamics.

Despite its importance, observations of the AMOC are still limited spatially and temporally, particularly in the South Atlantic (Rhein, 2019). There are only two in situ observing arrays of the AMOC in the South Atlantic: the TSAA/Tropical Atlantic Circulation and Overturning - TRACOS (11°S; Hummels et al., 2015; Herrford et al., 2021) and the South AMOC Basin-wide Array - SAMBA (35°S; Meinen et al., 2018; Kersalé et al., 2020). TRACOS uses a total of 5 bottom pressure stations to capture boundary variability on both boundaries of the Atlantic basin, combined with altimetry data to obtain AMOC anomalies at 11°S. Hummels et al. (2015) detected a salinity increase of up to 0.1 psu per decade from the surface to intermediate layers at 5°S and 11°S near the western boundary by comparing observations from two periods, 2013-2014 and 2000-2004. Using reanalysis data, Goes et al. (2014) associated the increase in salinity at intermediate depths to the increase of the salty Agulhas Leakage into the Atlantic, due to the strengthening of the westerlies associated to the Southern Annular Mode, similar to the mechanism described in Durgadoo et al. (2013). Herrford et al. (2021) observed an important seasonal cycle in the AMOC variability, where in the upper 300 m the eastern boundary forcing dominates the AMOC variability, but both eastern and western forcings are important from 300 to 500 m depth.

At 35°S, SAMBA array has been in place since 2009, in the beginning with six PIES, and over the years reaching more than twenty moorings, including two tall moorings deployed in December 2022. This array revealed strong variability on both upper and abyssal cells of the AMOC (Kersalé et al., 2020). The AMOC variability at 35°S is greatly influenced by the eastern boundary forcing at an interannual time scale, but the western boundary contributions are still significant (Meinen et al., 2018). The influence of the western boundary is greater on the AMOC variability at semiannual or shorter time scales (Meinen et al., 2018). These results suggest a greater influence of both boundaries on the AMOC dynamics in the South Atlantic when compared to the North Atlantic.

Recent studies have stressed the need for understanding the meridional coherence of the AMOC (e.g., Frajka-Williams, 2019; McCarthy et al., 2020). Anomalous signals from the South Atlantic can propagate towards the subpolar North Atlantic and affect deep water formation (Biastoch et al., 2009; Desbruyeres et al., 2021). The AMOC-induced heat and freshwater convergences and divergences drive changes in regional heat and freshwater contents and in sea level (Little et al., 2017; Volkov et al., 2019), which can impact the climate locally (Chang et al., 2008) and remotely (Lopez et al., 2016).

Building an AMOC observing system at 22.5°S will bridge the two existing observing systems located at the edges of the South Atlantic subtropical gyre, and provide estimates that can be compared to the historical cross-basin hydrographic programs such as WOCE and GO-SHIP occurring since the early 1990s. However, building new, sustainable observing systems can be a daunting task due to the operational and financial costs associated with it (Chidichimo et al., 2023). Therefore, an AMOC observing system that can rely on existing sustained observations at no additional costs is a strategic opportunity that will enhance our understanding of this vital climate component.

Although there are altimetry-based AMOC reconstructions at a few locations in the South Atlantic (e.g., Dong et al., 2021, Schmid et al., 2018), these estimates rely on linear regression between altimetry and in situ data, which are dependent on the reliability of these relationships. However, between 11°S and 35°S, an AMOC estimate which relies solely on sustained hydrographic data has not been attempted previously. At 22°S, the existing AX97 XBT high-density transect, which to date accounts for nearly 100 sections, can be a reliable constraint of the variability of the western boundary current, which is known to have a great influence on the AMOC variability in other locations (e.g., Gulf Stream). In addition, according to Dong et al. (2021), the AMOC time series at 35°S is not correlated with 20°S, which suggests a different regime than the current existing arrays, thus the 22°S estimate can serve as a benchmark for the AMOC variability in this latitude.

With that said, we implement a cost-effective transbasin section at 22.5°S to estimate the AMOC and its seasonal and interannual variability over 2007-2020 by merging available in situ observations and reanalysis products.

This paper is organized as follows: the in situ and reanalysis data used in this study are presented in Section 2, as well as the methodology to construct the referenced transect and its AMOC estimation. Section 3 consists in evaluating the methodology. Section 4 presents the AMOC and Meridional Heat Transport (MHT) time series, and their different components from the reference section and from other products available in the region. Section 5 gives a summary of the present study.

2 Data and Methods

2.1 In-situ profile data

Observational data from three high density expendable bathythermograph (XBT) transects (AX08, AX18 and AX97) and Argo profiling floats in the South Atlantic Ocean are used to build a transbasin transect near 22.5°S (Figure 1). The XBT probes measure temperature

(T) along fixed transects from surface to depths of about 800 m, and Argo floats measure T and salinity (S) down to 2000 m. The AX08 transect crosses the Atlantic Ocean from Cape Town (South Africa) to New York (USA), spanning through the eastern part of the South Atlantic subtropical gyre. The AX18 transect monitors the AMOC and MHT with two cross-basin zonal transects at approximately 34.5°S, and some of its realizations go further north to ~24°S in the western side of the basin depending on the availability of merchant ships. The AX97 monitors the BC at 22°S from Rio de Janeiro (Brazil) to Trindade Island (~30°W). The average temporal sampling frequency of AX08 and AX18 transects is 3 months/year and 2 months/year for the AX97. The average horizontal resolution ranges from 18 to 27 km. T data from XBT probes are obtained from the NOAA/AOML database. S profiles are derived from XBT-based T profiles using a seasonal regression method proposed by Goes et al. (2018). Delayed mode Argo profile data (Argo 2020) are used from the Global Argo Data Repository of the National Centers for Environmental Information (NCEI). Only Argo T-S profiles flagged as good or potentially good are used. The disparity found in some profiles, for which the available S data were fewer than the T data, was circumvented by applying the same regression methodology to estimate S for the XBT profiles.

To complete the profiles for the full water column, i.e., below 800 m for XBT data and below 2000 m for Argo data, the 0.25º horizontal resolution NCEI World Ocean Atlas 2018 (WOA18) T-S climatology is used, at monthly averages between 800 and 1500 m, and seasonal averages below 1500 m (Garcia et al., 2019; Locarnini et al., 2018; Zweng et al., 2018). Monthly WOA18 data have 57 vertical levels from 0 to 1500 m, and seasonal data have 112 vertical levels from 0 to 5500 m. Sensitivity tests performed with Argo data showed that the effect of padding from 800-1600 m is negligible relative to uncertainties that arise from the sampling strategies and from the methodologies of heat and volume transports calculation.

Each T-S profile is linearly interpolated to 140 pre-defined depths, starting from 5 m at 10 m intervals until 750 m, 50 m intervals until 2000 m, and 100 m intervals until a maximum depth of 6000 m.

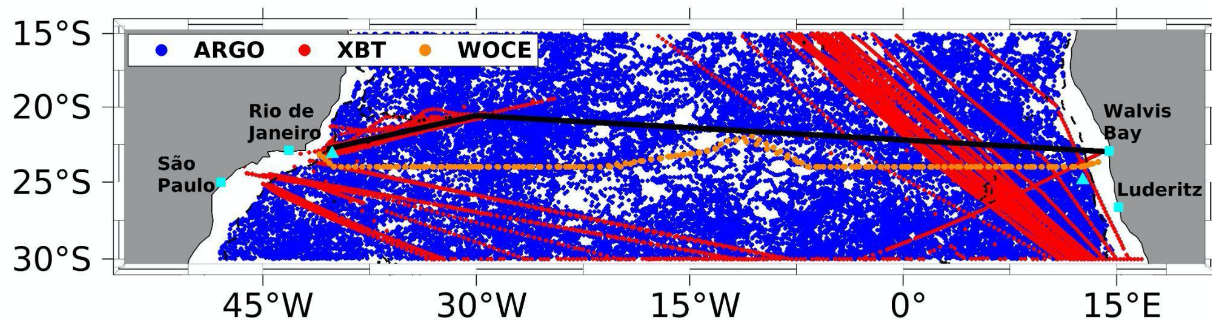

Figure 1. Spatial distribution of in situ data used in this work. Location of Argo (XBT) profilers are represented by blue (red) dots, and yellow dots represent the location of T-S profilers acquired at WOCE cruises in 2009 and 2018. The reference transect is represented by the black line. The location of coastal tide gauges is represented by cyan squares. Cyan triangles represent

the coordinates of sea level data from altimetry dataset compared to AXMOC data at the boundaries. Dashed black lines represent the 1000 m isobath.

2.2 Auxiliary data

To estimate the Ekman component of the AMOC, we use the monthly zonal wind stress from the ERA5 atmospheric reanalysis (Hersbach et al., 2020), which is available at a 0.25º horizontal grid since 1979. We linearly interpolated ERA5 wind stress to the reference section for the period 2007-2020.

For data validation, comparison, and water mass analysis, we used the Argo T-S 0.5° x 0.5° gridded monthly climatology (RG Argo- Roemmich & Gilson, 2009) from 2007-2020, and the World Ocean Circulation Experiment (WOCE) hydrographic profiles (Koltermann et al., 2011). The WOCE T-S data from transect A9.5 located close to 24°S from South America to Africa were acquired by two different scientific cruise surveys in 2009 and 2018 (740H20090307 and 740H20180228, respectively). A total of 238 CTD/O_2 stations were collected in those 2 periods, and 214 of those stations were used in this study (Figure 1). WOCE data are interpolated to the same 140 pre-defined depths used in the XBT and Argo profiles. WOCE data are used as independent measurements to evaluate the methodology adopted by this study in obtaining high-resolution T-S sections at 22.5°S. We also used the T-S from ECCO version 4 release 4 (ECCOv4r4), covering the period 1992-2017 at a 0.5° x 0.5° horizontal resolution. This product is an updated edition to that described by Forget et al. (2015). Finally, for the in situ profile data mapping calibration and validation, we use monthly gridded sea level anomaly (SLA) from January 1993 to December 2020 from a multi-satellite altimetry mission, processed and distributed by the Copernicus Marine and Environment Monitoring Service (CMEMS). The SLA maps are filtered, bias corrected, and corrected for atmospheric pressure effects and tides using the method of Pujol et al. (2016). Monthly maps of a 20-yr mean dynamic topography (Rio et al., 2011) are added to SLA to obtain the sea surface height (SSH) fields. The global mean sea level rose on a rate of 3.35±0.4 $mm\ yr^{-1}$ from 1993 to 2017 (Ablain et al., 2019), which was ~1.95 $mm\ yr^{-1}$ higher than the calculated in situ dynamic height (DH) trends. To avoid time varying biases during the mapping optimization phase, linear trends are removed from the fields at each longitude of the reference transect.

2.3 High-Resolution T-S Reference Section mapping methodology

A high-resolution reference section based on Argo and XBT data at 22.5°S, hereafter AXMOC, was defined in order to maximize the data availability along the section. Therefore, on the western side of the basin, the section follows the AX97 XBT transect from Rio de Janeiro to Trindade Island (~30°W), and from 30°W to Walvis Bay in Namibia. Long-record tide gauges are located on both ends of the reference transect (Figure 1). Data from two other XBT transects, the AX08 and AX18 are used to improve data coverage locally along their tracks. The coverage of Argo profiles is greater where bathymetry is deeper than 1000 m, and it has improved after 2007 in the South Atlantic following the initial spinup of the program since 2004 (Roemmich et al., 2009).

The mapping methodology used to reconstruct the reference section consists in weighted averages (Goes et al., 2010; Goes et al., 2020) using a normalized separable exponential function in space and time, given by:

$$W = exp\left(-\frac{\sqrt{x^2+y^2}}{\Delta R}\right) * \exp\left(-\frac{\delta t^2}{\Delta t}\right) \qquad (1),$$

where ΔR is a spatial radius, Δt is a time window, δt is the time difference between the profile and the reference time (15th of each month), and x and y are the zonal and meridional distance between the profile location and the referenced coordinate position, respectively. A set of 20 reference sections is generated considering a combination of weight values obtained varying ΔR (0.25°, 0.50°, 1°, 3° and 5° radius) and Δt (30, 60, 90 and 180 days). The search radius at the boundaries (<30°W and >0°) are enlarged in the y-direction by a factor of 3 with a cut off of 5° in order to minimize data gaps, assuming the features are more coherent along the boundaries than across.

The optimal T-S section is obtained by optimizing the mapping parameters ΔR and Δt locally by reducing the root mean squared error (RMSE; used as a cost function) between absolute DH and the SSH data interpolated to the reference section (Figure 2). The absolute DH of each parameter subset is referenced to 1000 m, and the absolute geopotential field from a blended Argo/altimetry climatology product is added to the reference level, similar to Goes et al. (2019). During calibration, both data are detrended in time to avoid misfits due to the mass and barotropic components of the variability in altimetry data.

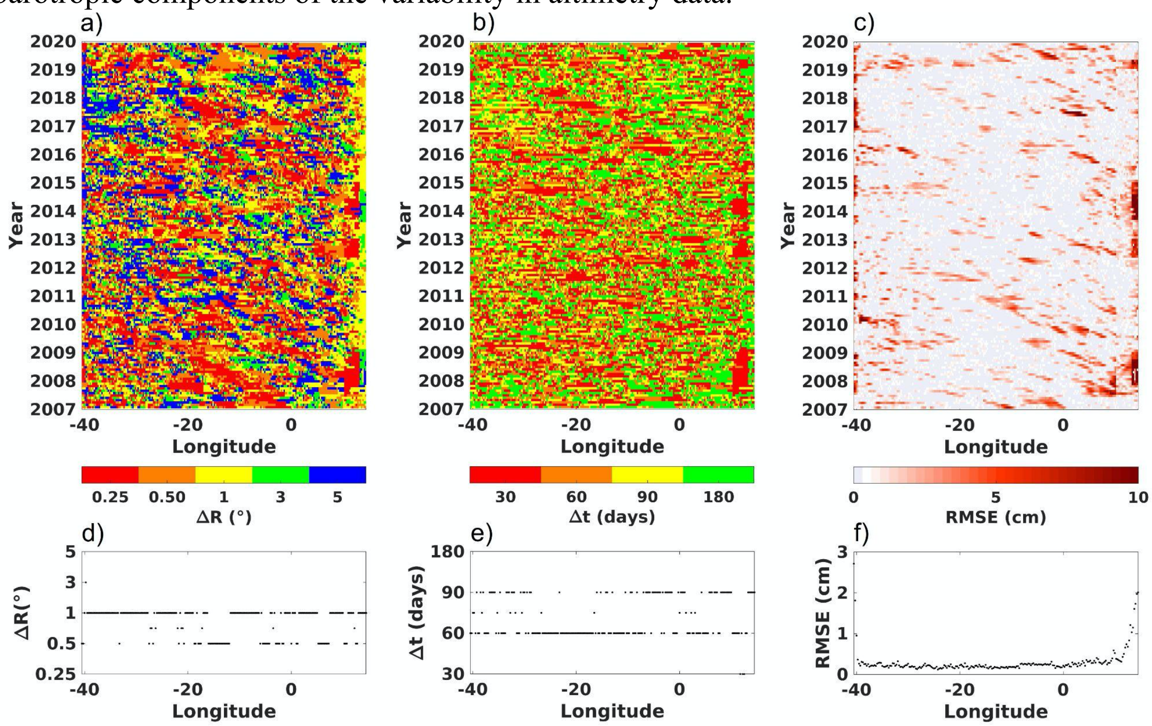

Figure 2. Values of spatial (a) and temporal (b) ranges used on the optimized mapping methodology to minimize the Root Mean Square Error (c). Median values for each longitude are presented for spatial range (d), temporal range (e) and RMSE (f).

The optimal ΔR and Δt parameter selection is generally noisy (Figure 2), which reflects the variable data coverage along the section, suggesting that small differences in the RMSE can influence the choice of the mapping parameters, and contribute to this variability. A possible solution to this issue is to include a prior probability distribution in the parameters to prioritize ΔR and Δt with higher resolution when RMSE variability is small among the different parameters (e.g., Goes et al., 2010). From sensitivity experiments, the impact of this approach in the final AMOC and MHT time series is small, even for higher ΔR and Δt values, since our methodology guarantees that greater weight is given to data closer in time and space to the referenced transect at a given time (Equation 1). The median ΔR (Δt) values fall between 0.50° and 1° (60 and 90 days) for every point of latitude (Figure 2d-e). Therefore, the median RMSE value between absolute HD and SSH is 0.79±1.40 cm, and increases to ~2 cm in the eastern boundary (Figure 2f). These values fall well within previously published RMSE values of 6.2 cm for areas between 5°S and 15°S, and up to 14 cm at the boundaries (Arnault et al., 1992; Strub et al., 2015).

2.4 AMOC and MHT time series

The AMOC and MHT across the reference section are calculated following published methodologies for the South Atlantic (e.g., Dong et al., 2015, 2021; Goes et al., 2015, 2020). The AMOC and MHT are divided into geostrophic and Ekman components. The geostrophic velocity field is computed from the gridded T-S data, using 3700 m as reference level, since it is approximately the depth of the neutral density γ=28.1 kg/m3, usually considered as the boundary between North Atlantic Deep Water (NADW) and Antarctic Bottom Water (AABW) at 22.5°S (see Section 3.3). This reference depth is similar to the one defined for 34.5°S (Goes et al., 2015). A zero net volume transport constraint is applied to the section at each month by adjusting the velocity field with a constant, calculated from the integrated transport across the section divided by the area of the section. The geostrophic AMOC streamfunction is estimated from the adjusted velocities, and its strength is defined as the maximum streamfunction at each timestep. The geostrophic time series is smoothed with a 3-month low-pass gaussian filter in order to remove high-frequency signals. The Ekman component, estimated using the ERA5 reanalysis, is integrated to the depth of the Ekman layer, which is considered to be 50 m deep. Both the AMOC and MHT represent the sum of Ekman end geostrophic components. The time series of the AMOC and MHT span from 2007 to 2020, since the AX97 transect started in 2004 and the Argo data has been more widely available across the South Atlantic basin after 2007.

3 Results

In this section, sea level, boundary currents, and water mass characterization are presented to evaluate the AXMOC product. The AMOC and MHT time series are decomposed into the seasonal, interannual (low-pass filtered with a 13-month Gaussian), as well as Ekman and geostrophic components.

3.1 Sea level

Here, the SLA calculated along the AXMOC transect from 2007 to 2020 is compared with the ones obtained from satellite altimetry and from the RG Argo data (Figure 3). Westward propagating signals are observed in satellite altimetry. These signals take between 2 to 4 years to cross the basin from east to west, generally without significant energy loss along their path, showing the importance of wave generation near the eastern boundary. An average phase speed of 5.9 ± 1.6 km/day is estimated for these propagations following the method of Barron et al. (2009), which corresponds to the period of the 1st baroclinic Rossby wave mode near 22.5°S (Polito and Liu, 2003). This westward propagation is not seen in the RG Argo product due to a rather coarse spatial and temporal mapping resolution. Nevertheless, our optimized mapping methodology calibrated to the SLA altimetry data allows detecting these propagation patterns reliably, in a good agreement with satellite altimetry data (Figure 3a, b).

A basin-wide, multi-year SLA pattern is observed in all three products, characterized by positive anomalies from 2007 to Jun/2010, negative between Jun/2010 and Apr/2015, and again positive from Apr/2015 to Dec/2020. As this variability pattern is characteristic for the entire basin, it could be linked to large-scale climate modes.

The proposed mapping methodology (AXMOC) also adequately reproduces the strong SLA variability near the boundaries, particularly near the western boundary due to the higher density of XBT data in the region. Near the eastern boundary, both satellite altimetry and AXMOC products capture some strong SLA signals, such as the negative anomalies in 2012-2013 and the positive anomalies in 2008-2009, 2017 and 2018-2019.

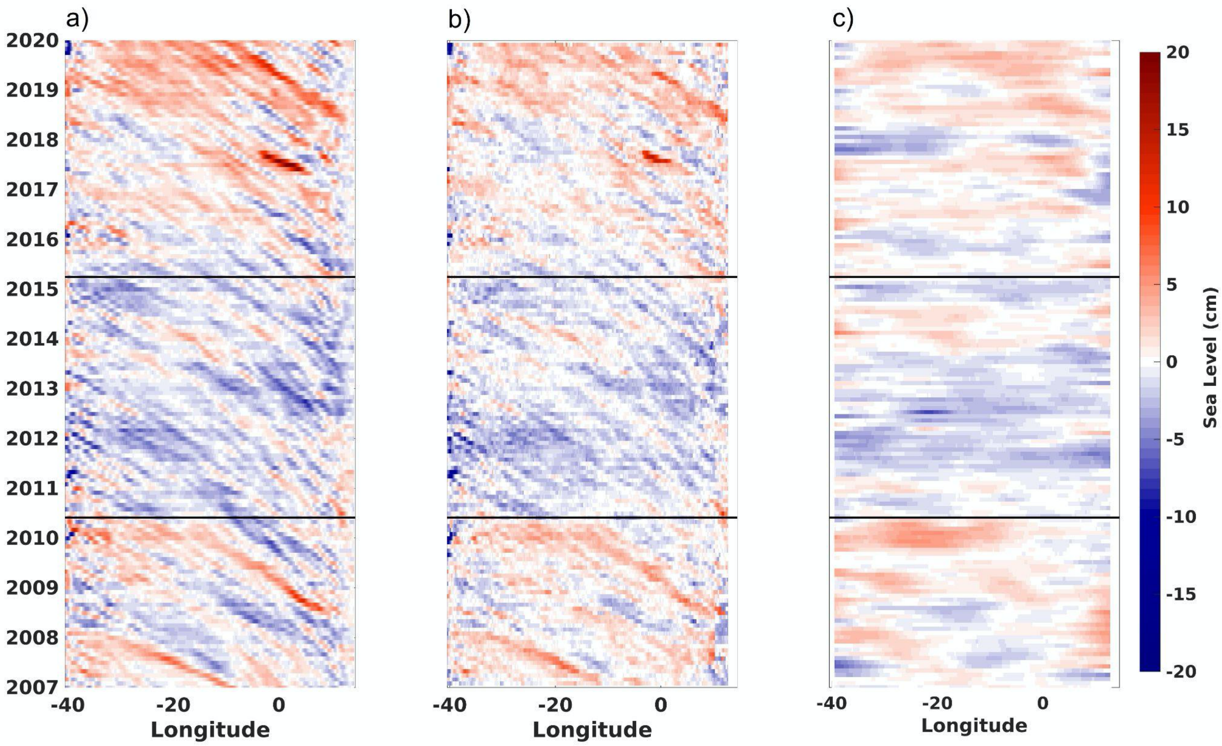

Figure 3. Hovmoller plot of the sea level obtained by altimetry (a), AXMOC (b) and RG Argo (c) datasets. Black horizontal lines indicate dates of 06/2010 and 04/2015. All datasets are de-seasoned and detrended to focus on the interannual variability.

The comparison of SLA time series from satellite altimetry and the AXMOC data near the western (40°W) and eastern boundaries (12.5°E) also validates the proposed methodology and provides valuable insight of the boundary currents variability (Figure 4). Since satellite SSH has other contributions than steric sea level, particularly in coastal areas, we selected for the boundary sea level height comparison with AXMOC the location of the satellite altimetry time series with higher correlation within 3° from the boundaries. The selected locations for the altimetry product are 40.12°W, 23.12°S (western boundary), and 12.62°E 24.87°S (eastern boundary), shown in light blue triangles in Figure 1. Overall, the region near the western boundary has greater variability compared to the eastern boundary (Figure 4). The standard deviation (used as a proxy of variability) of the SSH near the western boundary was 5.7 cm

(Figure 4a), and 3.4 cm (Figure 4b) near the eastern boundary. The AXMOC data show similar values to SSH near the western (4.9 cm) and eastern (3.1 cm) boundaries.

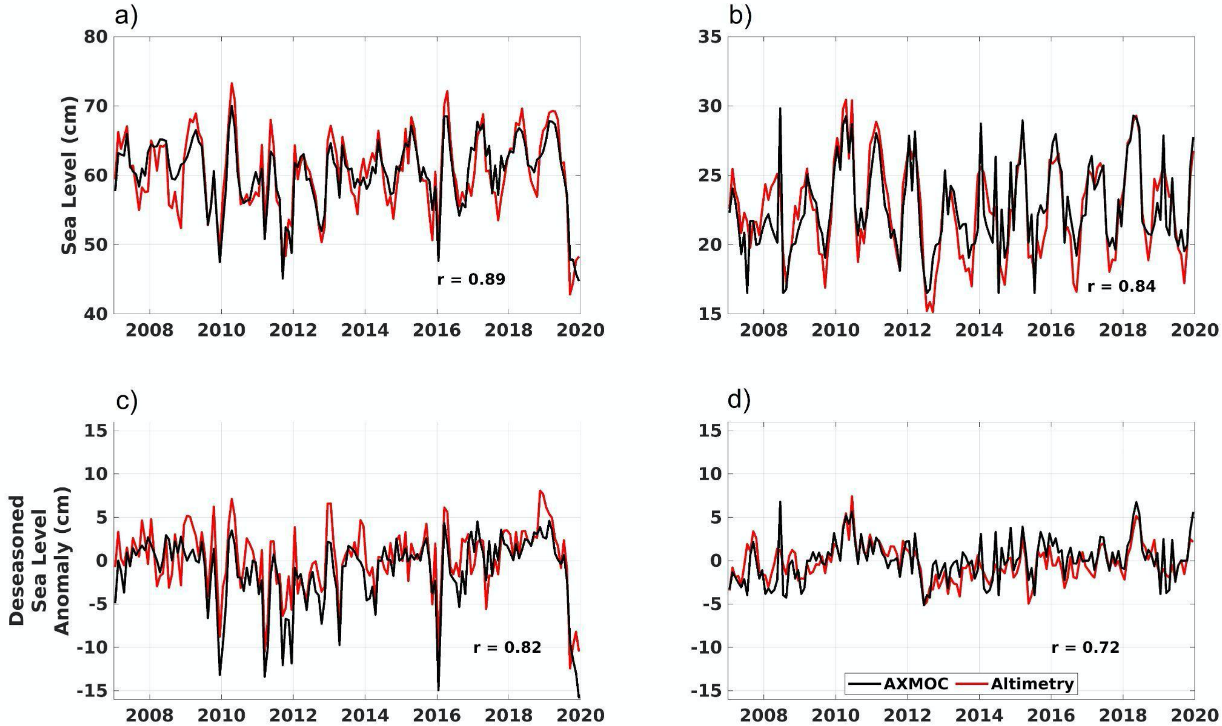

Figure 4. Absolute (a and b) and de-seasoned (c and d) SSH at the western (a and c) and eastern (b and d) boundaries of the section. Red is for altimetry data, and black is for the AXMOC estimates. The associated correlation values are shown in each panel.

A good correlation of sea level from AXMOC with altimetry data was obtained at both boundaries (0.89 at the western and 0.84 at the eastern boundary). When considering the de-seasoned sea level anomaly, the correlation at both boundaries remained robust (0.82 for the western and 0.72 for the eastern boundary). Most of the SLA extreme events that arise in the altimetry data also appeared in the AXMOC data (e.g., extreme values at the end of 2009, 2011, 2016, and end of 2019 at the western boundary, and the extreme values early 2010, mid 2012 and mid 2018 at the eastern boundary). The robust correlations observed on both ends of the section, even though the western boundary is densely sampled by XBTs and the eastern boundary is only sparsely sampled by Argo floats, indicate that the use of a sea level-oriented mapping methodology is appropriate to monitor the evolution of near-coastal features.

3.2 Boundary currents

Here, we compare boundary currents derived from the AXMOC with those derived from the RG Argo and simulated by the ECCOv4r4 state estimate. At 22.5°S, the BC is a shallow and narrow southward flow along the Brazilian coast placed on top of the northward inflow of the Intermediate Western Boundary Current (Calado et al., 2008). In the AXMOC data, the mean BC is located west of 39°W in the top 500 m (Figure 5). In the RG Argo, the BC is constrained to the west of 39.75°W, and a strong northward core appears east of 39.75°W, which is an artifact caused by the reverse DH gradient created from the lack of in situ data near the western boundary (Goes et al., 2020). In ECCOv4r4, the BC appears shallower and wider (west of 38°W) than in the AXMOC data. To analyze its volume transport in the three data products, we define the BC as the southward flow in the upper 500 m between the western boundary and 38°W. The 10-year (2007 to 2017) averaged and standard deviation of the volume transport is higher (-3.74±1.92 Sv) for the AXMOC, compared to -1.95±0.62 Sv for the RG Argo and -3.23±1.03 Sv for the ECCOv4r4. The mean BC core speed is also higher in the AXMOC data (-0.19±0.10 $m\ s^{-1}$) than in the RG Argo (-0.15±0.04 $m\ s^{-1}$) and ECCOv4r4 data (-0.10±0.02 $m\ s^{-1}$). The BC transport mean and standard deviation are better represented by AXMOC data when compared to previous regional studies (e.g., da Silveira et al. 2008; Lima et al., 2016; Mata et al., 2012; Pereira et al., 2014; Pita et al., 2020). This increased variance of the AXMOC is caused by a stronger BC interannual variability, which captures the strong event in the summer of 2009/2010, analyzed in Goes et al. (2019), as well as other events such as 2014 and 2016 which were also observed in that study. This interannual variability is dampened in the other two products.

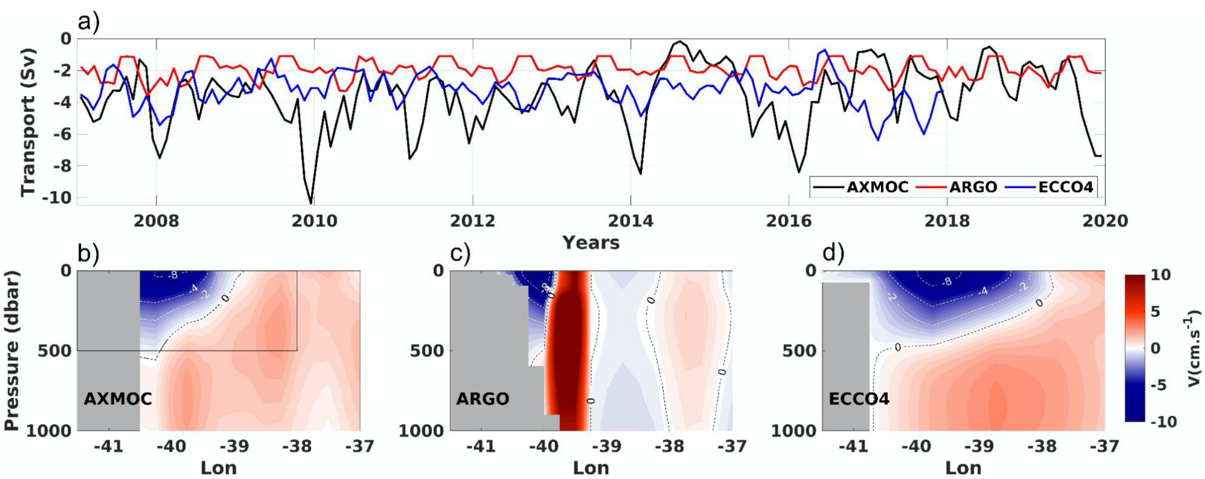

Figure 5. Evolution of the Brazil Current (BC) transport from 3 different data (a): AXMOC (black line), RG Argo (red line) and ECCOv4r4 (blue line). Mean velocity section focused on western boundary is shown for AXMOC (b), RG Argo (c) and ECCOv4r4 (d) datasets. The black rectangle indicates the region where the BC transport is being calculated.

Close to 22°S, the Benguela Current (BeC) is the eastern boundary current, which flows equatorward between the coast to 3°E, limited by the Walvis ridge (Garzoli et al., 1996; Majumder and Schmid, 2018). The AXMOC data capture the BeC as an equatorward flow from surface down to 500 m with a core located between 10 and 12°E (Figure 6). The poleward flow east of 12°E is the expression of the Poleward Undercurrent (PU), an ocean current derived from the sinking of the Angola Current at the Angola Benguela Frontal Zone (ABFZ - Berger et al., 1998). On the other hand, the RG Argo data shows a strong equatorward flow along the edge of continental shelf, due to the lack of data near the coast. The BeC transport of 12.57±2.58 Sv observed in AXMOC is greater than the ones in the RG Argo (9.99±1.95 Sv) and ECCOv4r4 data (3.43±0.68 Sv). AXMOC data perceive a more intense and variable BeC if compared to other products. The ECCOv4r4 estimate of BeC transport is lower than the AXMOC and RG Argo data. The ECCOv4r4 data capture a smoother BeC, with smaller interannual variability. The AXMOC results are in accordance with Majumder and Schmid (2018), which also reported a decreasing mean BeC volume transport on lower latitudes, varying from 23 Sv at 31°S to approximately 9 Sv at 25°S.

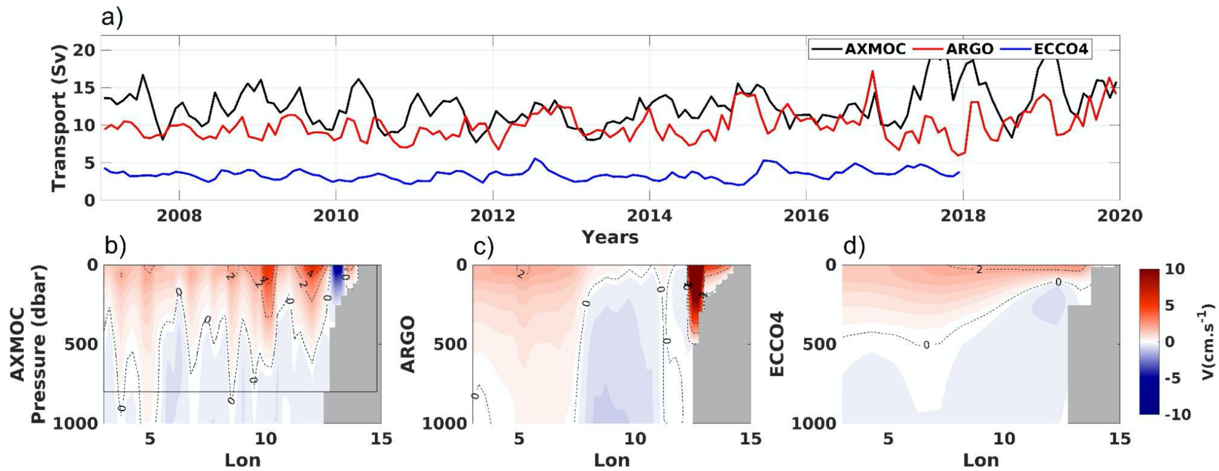

Figure 6. Evolution of the Benguela Current (BeC) transport from 3 different data (a): AXMOC (black line), RG Argo (red line) and ECCOv4r4 (blue line). Mean velocity section focused on the eastern boundary is shown for AXMOC (b), RG Argo (c) and ECCOv4r4 (d) datasets. The black rectangle indicates the region where the BeC transport is being calculated.

3.3 Water masses

This subsection covers the water masses captured by the AXMOC data and compares its results with alternative independent in situ data from WOCE. The transbasin section at 22.5°S is characterized by more intense circulation on both boundaries in comparison to the interior of the section (Figure 7). Most of the variability along the section is concentrated in the upper ocean and near the boundaries (Figure 7b).

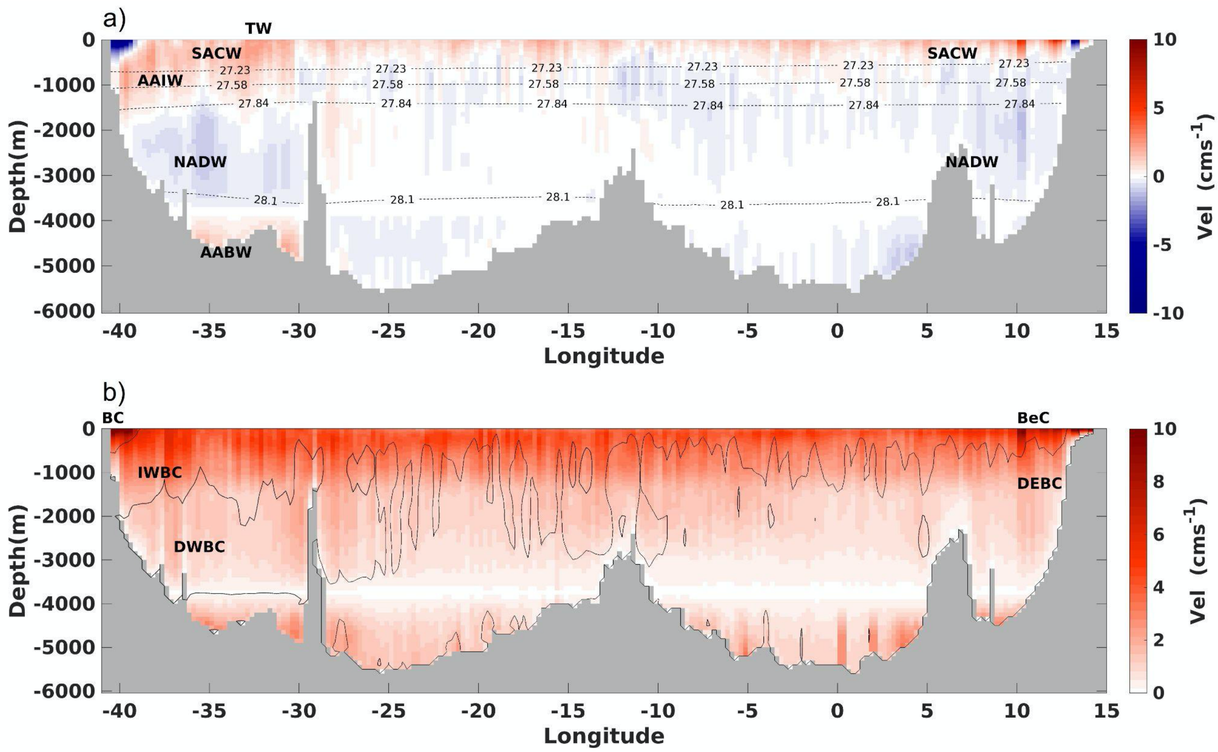

Figure 7. Mean northward velocity (a) and its standard deviation (b) computed from the AXMOC data. Main water masses (a) and ocean currents (b) are indicated: Tropical Water (TW), South Atlantic Central Water (SACW), Antarctic Intermediate Water (AAIW), North Atlantic Deep Water (NADW), Antarctic Bottom Water (AABW), Brazil Current (BC), Benguela Current (BeC), Intermediate Western Boundary Current (IWBC), Deep Western Boundary Current (DWBC) and Deep Eastern Boundary Current (DEBC). Neutral density isopycnals are represented by dashed lines (a). Solid lines indicate contour of no meridional velocity (b).

The AABW is the deep equatorward flow (>4000 m) confined in the western boundary west of 30°W, constrained by the Trindade Island topography, and its mean flow reaches speeds of 0.02 ± 0.01 $m\ s^{-1}$ at 22.5°S (Figure 7). The AABW is characterized by T < 2°C, S < 34.8 and reduced dissolved oxygen levels ($O_2 \simeq 220\ \mu mol\ kg^{-1}$) relative to NADW (Figures 8 and S1), which is in agreement with Reid et al. (1989). Between 50°S and the equator, the AABW flows along neutral density lines $\boldsymbol{\gamma}$> 28.10 $kg\ m^{-3}$ (Liu & Tanhua, 20219).

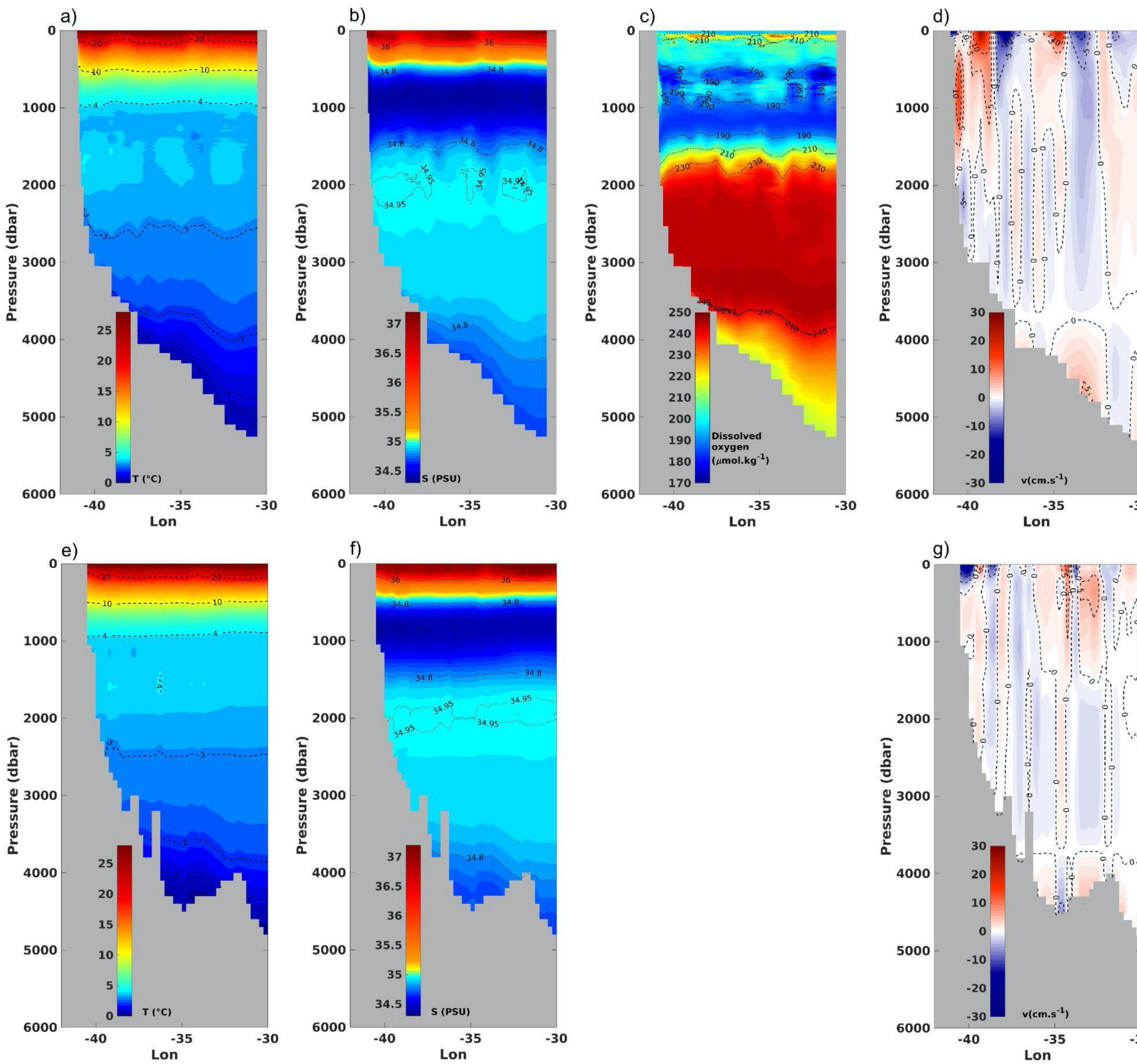

Figure 8. Ocean tracers and velocity section focused on western boundary for April 2009 at 24 and 22.5°S. A-d (e-g) panels represent WOCE (AXMOC) dataset. Temperature (T), salinity (S), dissolved oxygen and velocity (v) are shown between western boundary and 30°W.

Similar to the AABW, the NADW is also confined by local topography near the western boundary. Near the eastern boundary (Figure 7), a secondary southward NADW branch is also visible. Indeed, the NADW has been reported to split into two branches before crossing 22°S: one branch remains flowing southward near the western boundary and another branch flows eastward along the equator (Talley, 2011). Both branches are located between 1700 and 3600 m and the western branch is more intense, reaching up to -0.01 ± 0.01 $m\ s^{-1}$ at 22.5°S (Figure 7). In the tropics, the NADW is usually divided vertically into the upper (uNADW) and lower NADW (lNADW - Talley 2011) cores. As it flows southward, vertical mixing slowly merges this two-lobed water mass into one main core flowing between neutral density surfaces of 27.84 and 28.10 $kg\ m^{-3}$ (e.g., Hernandez-Guerra et al., 2019; Liu & Tanhua, 2021; Stramma et al., 2004). This single core signal is observed on both branches of the NADW (Figure 7), which is characterized by a local maximum in salinity (S >34.85) and a maximum in dissolved oxygen (O_2 > 240 $\mu mol\ kg^{-1}$) near the western boundary (Figure 8).

The Upper Circumpolar Deep Water (UCDW) is defined as a fresh (core S around 34.6), low oxygen water mass with neutral density between 27.58 and 27.84 $kg\ m^{-3}$ and located between 1150 and 1550 m deep (e.g., Hernandez-Guerra et al., 2019). It is characterized by low salinity (S<34.8) and poor oxygen levels (O_2 < 190 $\mu mol\ kg^{-1}$; Figure 8). Located above the UCDW, at depths varying from 700 and 1150 m, the Antarctic Intermediate Water (AAIW) is characterized by a minimum salinity at its core (S < 34.5) located around 800 m, and relatively high oxygen levels, flowing along neutral densities between 27.23 and 27.58 $kg\ m^{-3}$. Both UCDW and AAIW form the Intermediate Western Boundary Current system (IWBC) at 22.5°S (Figure 7), which is characterized by an equatorward flow near 38°W between about 600 and 1700 m depth (Figure 7).

The isolines of T, S and dissolved oxygen in the AXMOC and WOCE data are located at similar depths (Figure 8 and S1). The isolines of the WOCE data are more variable, while the AXMOC isolines are smoother because of the time and space averaging applied during the mapping procedure. The WOCE data is based on CTD casts, and has not been smoothed.

A direct comparison of volume transport per neutral density intervals is an important step to evaluate the mapping methodology applied here (Figure 9). While AXMOC and WOCE estimations are calculated from their respective T-S profiles, Cainzos et al. (2022) employ an inverse box model to compute decadal AMOC estimates from WOCE transects. The top layer (from surface to $\boldsymbol{\gamma}$= 26.45 $kg\ m^{-3}$) is composed by the geostrophic transport and the Ekman transport, while the remaining intervals are composed solely by the geostrophic transport. A good agreement exists between AXMOC and WOCE volume transport estimates in the upper 1000 m, characterized by $\boldsymbol{\gamma}$< 27.58 $kg\ m^{-3}$. The AXMOC data show a transport of 20.60 Sv and 20.48 Sv for Apr/2009 and Mar/2018, respectively. The volume transports in the WOCE data are 22.78 Sv and 18.95 Sv for Apr/2009 and Mar/2018, respectively. The difference between the WOCE and the AXMOC data in the upper ocean ($\boldsymbol{\gamma}$< 27.58 $kg\ m^{-3}$) is generally within the uncertainty interval estimated by Cainzos et al. (2022).

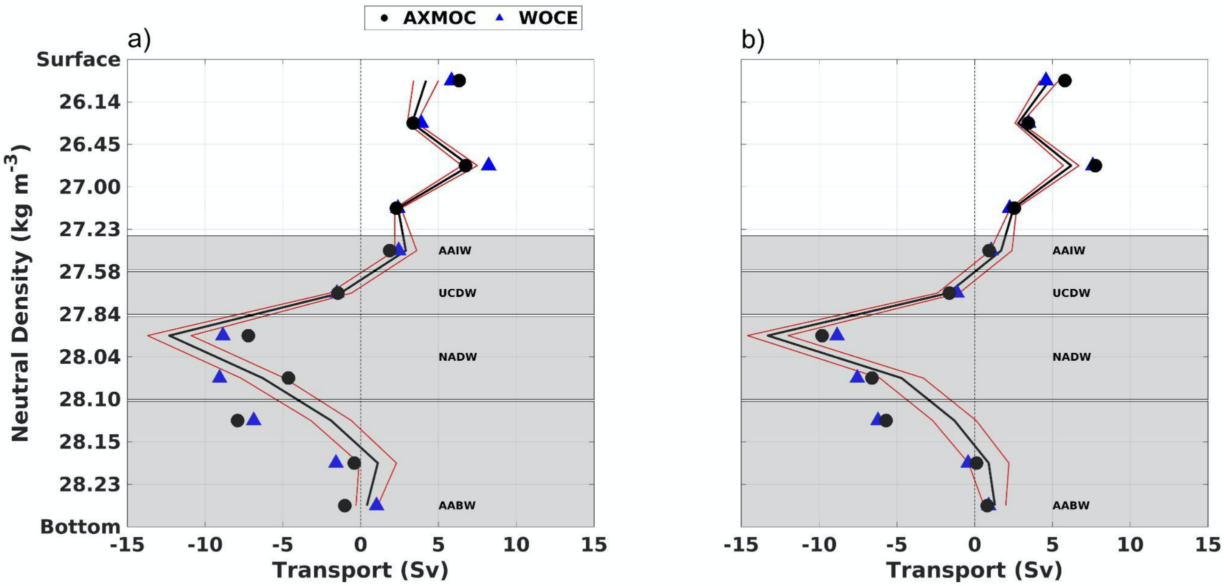

Figure 9. Volume transport at different neutral density levels for two different months: Apr/2009 (left panel) and Mar/2018 (right panel). AXMOC data is represented by black circles and WOCE data by blue triangles. Black line and red lines represent the volume transport and its uncertainties estimated by the inverse model of Cainzos et al. (2022) for the decades of (left) 2000s and (right) 2010s decades. The gray areas represent the density ranges of the main water masses across the section: Antarctic Intermediate Water (AAIW), Upper Circumpolar Deep Water (uCDW), North Atlantic Deep Water (NADW) and Antarctic Bottom Water (AABW).

The area encompassing upper layer boundary currents ($\boldsymbol{\gamma} < 27.23\ kg\ m^{-3}$), i.e., BC and BeC, has a positive net volume transport of 18.74 Sv and 19.55 Sv for Apr/2009 and Mar/2018, respectively (Figure 9). For WOCE data, the volume transports are 20.34 Sv and 17.89 Sv for Apr/2009 and Mar/2018, respectively. AXMOC and WOCE results are similar in every level for both periods analyzed (Apr/2009 and Mar/2018), and this similarity is also observed with the decadal results from Cainzos et al. (2022). At 22.5°S, the upper AMOC cell is located from surface to $\boldsymbol{\gamma}$=27.58 $kg\ m^{-3}$, and the lower AMOC cell is located from $\boldsymbol{\gamma}$=27.58 $kg\ m^{-3}$ to the bottom. Considering the layer encompassing the UCDW, the resulting AXMOC-based transport is slightly negative of -1.47 Sv and –1.62 Sv for Apr/2009 and Mar/2018, respectively (Figure 9), because the more intense intermediate equatorward currents are limited to the western boundary, while the interior and eastern boundary have poleward flow (Figure 7). In both periods analyzed, the NADW is the main conduit of the lower AMOC cell from neutral density of 27.84 to 28.10 $kg\ m^{-3}$ (Figure 9). Finally, the resulting transport on the layer encompassing the AABW turns back poleward mainly because of the influence of the deep western boundary current. The mapping methodology is robust considering that most of its estimates fall within 2 times the uncertainty levels of the independent study performed by Cainzos et al. (2022), especially in the upper ocean. It is important to highlight that both sections, AXMOC and WOCE (also used as reference in Cainzos et al., 2022), are not located at the same latitude. WOCE section is located around 24°S and AXMOC transect location varies between 20.5 and 23°S. Greater differences from AXMOC, WOCE and Cainzos et al. (2022) are observed in areas with $\boldsymbol{\gamma} > 27.84\ kg\ m^{-3}$, because of uncertainties inherent in the methodology and use of WOA18 climatology data on the AXMOC section in areas without XB and Argo observations.

3.4 AMOC and MHT time series

In this subsection, the newly produced AMOC and MHT time series from AXMOC data are presented along with their contributions from geostrophic and Ekman components. The correlations of AMOC and MHT with each component and with estimates from other datasets are also discussed and presented in the supplementary material (Figures S2-S4). Finally, the influence of western and eastern boundaries, and the interior region of the ocean is addressed.

3.4.1 Mean and Seasonal cycle

The estimated mean AMOC (MHT) transport from AXMOC data is 16.34±3.20 Sv (0.73±0.20 PW) between 2007 and 2020. The total AMOC (MHT) transport from AXMOC is composed by an intense equatorward geostrophic transport of 21.74±2.85 Sv (1.15±0.17 PW) and a significant poleward AMOC (MHT) Ekman component of -5.41±1.49 Sv (-0.43±0.11 PW - Figure 10 and Table 1). On a seasonal time scale, the AMOC is stronger in June and weaker in September, and the MHT is more intense in May and weaker in September (Figure 10).

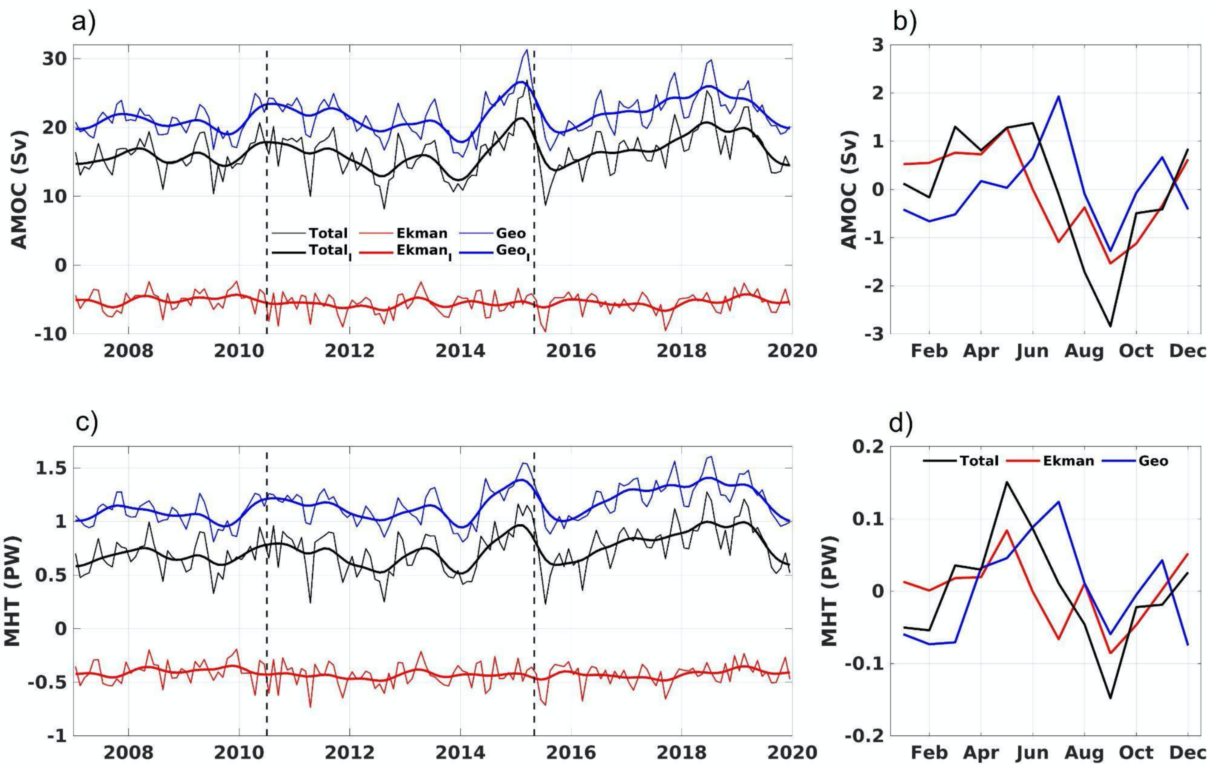

Figure 10. AMOC and MHT time series (left) and associated seasonal cycles (right). AMOC (a, c) and MHT (d, f) time series are divided into Geostrophic (blue lines), Ekman (red lines) and total components (black lines). Solid lines represent the 13-month gaussian filtered component of AMOC and MHT (a and c, respectively). Vertical black dashed lines indicate dates of 06/2010 and 04/2015.

	Total	Geostrophic	Ekman

	AMOC	MHT	AMOC	MHT	AMOC	MHT
AXMOC	**16.34±3.20**	**0.72±0.20**	**21.74±2.85**	**1.15±0.17**	**-5.41±1.49**	**-0.42±0.10**
Dong - 20°S	**16.45±2.13**	**0.62±0.17**	**22.70±1.49**	**1.20±0.09**	**-6.26±1.66**	**-0.58±0.14**
Dong - 25°S	**19.30±2.20**	**0.68±0.17**	**23.00±1.64**	**1.01±0.12**	**-3.70±1.42**	**-0.33±0.13**
ECCOv4r4	**14.11±2.55**	**0.48±0.16**	**19.13±1.84**	**0.87±0.10**	**-5.01±1.38**	**-0.39±0.10**

Table 1. Mean and std values for AMOC (Sv) and MHT (PW) between 2007 and 2019. Total, geostrophic and Ekman components are represented in separated columns.

A comparison of the AMOC (MHT) from AXMOC with that from Dong et al. (2021) synthetic product and the ECCOv4r4 state estimate is shown in the Supplementary Material (Figures S2-S4). The seasonal variations in the AMOC and MHT also have similar patterns to other products which present positive values from April until July and negative values between August and October (Figure S3). Overall, the mean values from AXMOC are within the uncertainty ranges of the other products for both AMOC and MHT (Table 1 and Figure S2). Correlations between AXMOC and individual products are higher for the MHT than for the AMOC: r=0.40 (Dong et al., 2021 - 20°S), r= 0.35 (Dong et al., 2021 - 25°S), and r=0.29 (ECCOv4r4) for the AMOC and r=0.59 (Dong et al., 2021 - 20°S), r= 0.51 (Dong et al., 2021 - 25°S) and r=0.44 (ECCOv4r4) for the MHT. This relatively low correlation between the AXMOC and the other datasets can be related to the amount of variance explained by the geostrophic component of the AMOC/MHT. The variance explained by the geostrophic and Ekman components of the AMOC are similar in Dong et al. (2021) and in the ECCOv4r4 data, approximately 40-60% for each component (Table 2). For the AXMOC, however, the geostrophic component is responsible for most (83%) of the total transport variance. The geostrophic component can also explain the stronger variability of the AMOC/MHT in the AXMOC time series (Table 1).

	AXMOC	Dong - 20°S	Dong - 25°S	ECCOv4r4
Geostrophic	**0.83 (0.77)**	**0.41 (0.33)**	**0.60 (0.44)**	**0.51 (0.58)**
Ekman	**0.17 (0.23)**	**0.59 (0.67)**	**0.40 (0.56)**	**0.49 (0.42)**

Table 2. AMOC variance explained by its geostrophic/Ekman components. The MHT variance explained by its geostrophic/Ekman components are presented in parenthesis.

3.4.2 Interannual variability

The low-pass filtered geostrophic component shows a strong correlation with the total component for both AMOC and MHT (r=0.96 and r=0.97, respectively), thus most of the AMOC and MHT variability in the interannual band is explained by the geostrophic transport (Figure 10). The AMOC decreases significantly when there are intense BC events (Figure 4), as observed during years 2011, 2014, 2015 and 2019. Previous studies indicate that the dominance of geostrophic and Ekman components on the AMOC varies at different latitudes in the South Atlantic. At 35°S, the relative dominance of Ekman and geostrophic components on AMOC and

MHT alternates throughout the time (Dong et al., 2015, 2021). Ekman dominance is also observed at 20°S, but a greater contribution of the geostrophic component is reported at 25°S (Dong et al., 2015). Results from the AXMOC transect corroborate with Dong et al. (2015, 2021) 25°S estimates on the overall dominance of the geostrophic component (correlations of 0.94/0.92) over the Ekman contribution (correlations of 0.15/0.21) for AMOC/MHT transports. In addition, high correlations (r > 0.95) are observed between the total AMOC and MHT time series at 22.5°S, as well as for the geostrophic and Ekman components. Other studies have also observed high correlations between the AMOC and MHT time series at various latitudes in both the North and South Atlantic (Dong et al., 2009, 2015, 2021; Johns et al., 2011), showing the dominance of velocity variability over temperature variability in the MHT time series.

The variability observed in the AXMOC time series appears to have changed since 2014, when the interannual to decadal variability strengthened, driving an increase in the AMOC by approximately 2 Sv (Figure 10). Dong et al. (2021) also observed a moderate interannual AMOC increase at 25°S on both total and geostrophic transports but only after 2017 (Figure S4). Due to the short extent of our time series we cannot draw any conclusion about the long term changes of the AMOC. Next, we will compare AXMOC time series with the decadal estimates of Cainzos et al. (2022), Dong et al. (2021) and ECCOv4r4, analyze it in the context of decadal variability.

3.4.3 Decadal variability

We estimated the AMOC transport using the WOCE/GO-SHIP data applying the same methodology used in the AXMOC. For the two WOCE sections of Apr/2009 and Mar/2018, the AMOC strength was 22.00 Sv and 18.59 Sv, respectively. The corresponding AMOC transports from the AXMOC data are 24.8 Sv and 19.96 Sv. The AXMOC estimates differ from WOCE estimates by +2.80 Sv and -0.63 Sv, respectively. Therefore, we estimate the error due to spatial mapping and data availability to be of ~ 2 Sv. To compare the decadal variability of AXMOC and other products, we used the 2010-2019 mean AMOC. The AXMOC mean of 2010-2019 AMOC value is 16.58±3.41 Sv, in comparison to 16.29±2.14 Sv (20°S) and 19.26±2.30 Sv (25°S) for Dong et al. (2021) and significantly smaller value for ECCOv4r4 of 13.75±2.39 Sv. Relative to the previous decade, Dong et al. (2021) observed contrasting changes such as a slight increase (0.19 Sv) in 25°S and a slight decrease (-0.58 Sv) in 20°S, while ECCOv4r4 showed an AMOC decrease of 1.19 Sv between the two periods.

Results from the Cainzos et al. (2022) adjoint model show a mean AMOC decrease of ~ 1.6 Sv from 2000-2009 to 2010-2019, 19.70±1.20 Sv to 18.10±1.10 Sv, respectively, which falls within the uncertainties of the methodology applied. The difference from Cainzos et al. (2022) and the AXMOC decadal means is also within 2 Sv. In addition, Cainzos et al. (2022) estimated a slightly higher mean AMOC of 19.80±1.00 Sv for the 1990-1999 decade. Therefore, our results corroborate to the conclusions drawn by Cainzos et al. (2022) that no significant changes were observed in the AMOC near 22.5S in the past three decades.

3.4.4 Boundary and Interior contributions

Finally, to understand if the specific areas of the AXMOC transect influence the AMOC at 22.5°S, we compare its geostrophic component to the transport in the upper 1000 m near the western boundary (from western coast to 38°W), interior of the section (from 39°W to 3°E), and near the eastern boundary (from 3°E to eastern coast). The AMOC geostrophic transport has a higher correlation with the western (r=0.69) than with the eastern boundary (r=0.41) (Figure 11).

This is different to what was observed at 34.5°S, where the eastern boundary contributes more to the AMOC variability than the western boundary (Meinen et al., 2018). A possible explanation for this difference is the increased influence of the Agulhas leakage in the eastern boundary close to 34.5°S. In addition, the interior and eastern boundary transports show a significant inverse relationship (r= -0.62) and compensation between the two regions (Figure 10). The anomalous strengthening of the AMOC in 2015 (Figure 10a), where the geostrophic contribution reached values close to 25 Sv, is due to a concurrent intensification of equatorward circulation on both boundaries (Figure 11). Apart from that, most of the AMOC anomalous intensification events are caused by the changes in only one of the boundaries.

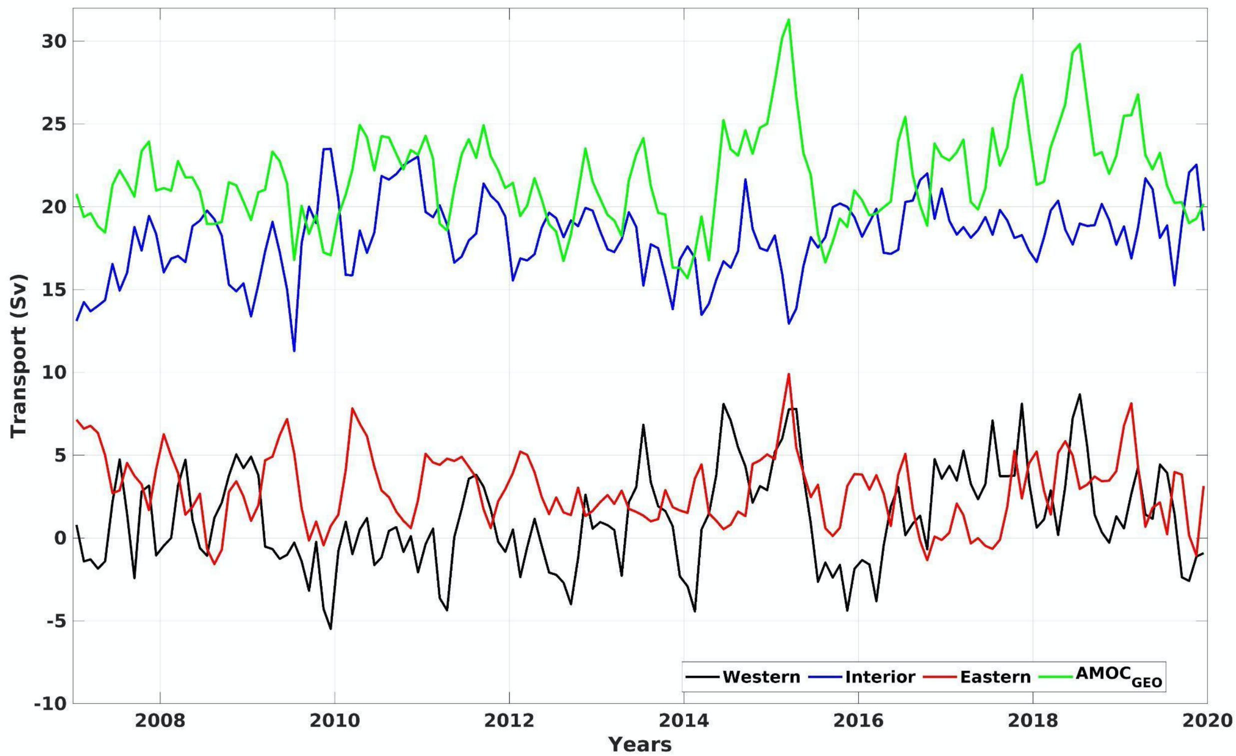

Figure 11. Upper 1000 m volume transport for western boundary (black), eastern boundary (red) and interior (blue) from the AXMOC data. The geostrophic AMOC transport is shown by a green line.

4 Conclusions

We use a combination of Argo and XBT data to produce the first estimate of the AMOC and MHT at 22.5°S. The current in situ coverage composed by Argo and XBT data is sufficient for the calculation of AMOC and MHT at 22.5°S from 2007 onwards. The altimetry optimized mapping methodology proved to be efficient in capturing westward wave propagation, boundary currents, AMOC and MHT. Near the western boundary, the first continuous long-term monthly transport of the highly variable BC was produced due to the good coverage by the high-density XBT transect implemented since 2004. BC volume transport anomalies observed in 2009/2010 are consistent with Goes et al. (2019). These and other BC anomalies (e.g., 2014 and 2016) are captured by AXMOC data and observed in the SLA time series at the western boundary.

Some physical properties (T, S and $\boldsymbol{\gamma}$) of the main water masses in the South Atlantic were also analyzed here, and are consistent with earlier studies (Hernandez-Guerra et al., 2019; Liu & Tanhua, 2021; Stramma et al., 2004 and Talley, 2011). The AABW is limited by neutral density lines $\boldsymbol{\gamma}> 28.10\ kg\ m^{-3}$, while the NADW flows between 27.84 and 28.10 $kg\ m^{-3}$. At 22.5°S, both AABW and NADW are constrained west of 30°W by local topography and the latter is divided into two cores flowing along the western and eastern boundaries near depths of 2500 m. In the uppermost isopycnal layer ($\boldsymbol{\gamma} < 27.23\ kg\ m^{-3}$), an important area for AMOC variability, AXMOC and WOCE data have a good agreement. The AXMOC data yields volume transports of 18.74 Sv and 19.55 Sv for Apr/2009 and Mar/2018, respectively, while WOCE data yields volume transports of 20.34 Sv and 17.89 Sv for the same period, respectively. The integrated isopycnal transport obtained by AXMOC is robust and an uncertainty of ~2 Sv in the AMOC transport due to the mapping errors is estimated from independent observations.

Seasonality in the AMOC and MHT time series shows a good agreement between all the products considered, with annual amplitudes of 4 Sv and 0.3 PW, respectively. Stronger AMOC/MHT values are observed in Jan-Jul and weaker values are observed in Aug-Dec. The geostrophic and Ekman contributions are in-phase and reinforce this variability. The interannual variability in the geostrophic component of the AMOC from AXMOC is more intense than those from other products, probably because of the improved resolution near the western boundary. The western boundary currents appear to have the largest contribution to the AMOC/MHT variability (r=0.62). Our results show sharp declines in the AMOC and MHT during positive BC anomalies (intense southward transport), such as in 2014, end of 2015 and 2019. Also, a period of more frequent negative values of total and geostrophic transports in both AMOC and MHT is observed between 2010 and 2015. Further analysis is needed, but the basin wide extent of this event suggests that they are related to large scale modes of variability in the South Atlantic. Finally, AXMOC data could also be used to assess freshwater flux anomalies in the South Atlantic and link it to a possible bi-stability of the AMOC (Rahmstorf et al., 1996; Stommel, 1961).

The observed AMOC (MHT) mean transport was 16.34±3.20 Sv (0.73±0.20 PW) between 2007 and 2020, and positive anomalies became more frequent after 2015 (Figures 10 and S4), although this trend was not statistically significant given the uncertainty of our estimates. The AMOC is projected to weaken according to the IPCC projections for the 21st century (Collins et al., 2019; Fox-Kemper et al., 2021; Lee et al., 2021). The future AMOC weakening has been linked to a BC intensification (Marcello et al., 2023), and our results corroborate with this link between the BC and the AMOC at 22.5°S, thus the continuation of this monitoring effort at 22.5°S might provide early evidence for changes in the AMOC in the Northern Hemisphere.

The availability of multi-decadal data of tide gauges on both sides of the basin can in the future be used to complement, validate, and extend the DH field on the boundaries. Deep Argo profilers and/or PIES stations have the potential to improve data availability in the South Atlantic deep ocean (>2000 m), and could replace climatological data in the deep ocean, since their spatial and temporal coverage has been increasing significantly. The proposed methodology can be replicated to include other latitudes in the Atlantic basin where the Argo and XBT coverage would permit a long term AMOC and MHT estimations. This expansion to other latitudes would be beneficial for the scientific community once an integrated assessment of the long-term variability of AMOC and MHT can be performed using a single methodology. Currently, the

AMOC has been monitored at different latitudes, however, each program has different limitations and uncertainties, which impacts the comparison and integration of different time series (Chidichimo et al., 2023). In addition, our methodology allows more frequent updates of the AMOC since Argo and XBT data are publicly available in near-real time, as opposed to mooring data from existing AMOC arrays. Therefore, our methodology, if expanded in time and space, could positively impact the prediction capability of different events (e.g., coastal sea level and hurricane season outlook).

Acknowledgments

This research was carried out in part under the auspices of the Cooperative Institute for Marine and Atmospheric Studies, a cooperative institute of the University of Miami and the National Oceanic and Atmospheric Administration (NOAA), cooperative agreement NA 20OAR4320472, and was supported by the Ocean Observing and Monitoring Division of the NOAA Climate Program Office and by NOAA's Atlantic Oceanographic and Meteorological Laboratory (AOML). MG and DLV were also supported by the National Oceanic and Atmospheric Administration (NOAA) Climate Variability and Predictability program (grant number NA20OAR4310407).

Open Research

The following data used for this study can be downloaded from: XBT transect data (http://www.aoml.noaa.gov/phod/hdenxbt/); Argo profile data (https://www.nodc.noaa.gov/argo/ and https://www.seanoe.org/data/00311/42182/ - http://doi.org/10.17882/42182); Argo/altimetry climatological ADT product (http://apdrc.soest.hawaii.edu/projects/argo/); the delayed-time satellite altimetry maps (http://marine.copernicus.eu); ERA5 atmospheric reanalysis (https://cds.climate.copernicus.eu); MOC and MHT synthetic time series (https://www.aoml.noaa.gov/phod/samoc_argo_altimetry/data_moc.php); WOA18 (https://www.ncei.noaa.gov/access/world-ocean-atlas-2018/); RG Argo (https://sio-argo.ucsd.edu/RG_Climatology.htm); ECCOv4r4 (https://www.ecco-group.org/products-ECCO-V4r4.html); WOCE (https://cchdo.ucsd.edu) for cruises A095 in 2009 (https://cchdo.ucsd.edu/cruise/740H20090307) and in 2018 (https://cchdo.ucsd.edu/cruise/740H20180228).

References

Ablain, M., Meyssignac, B., Zawadzki, L., Jugier, R., Ribes, A., Spada, G., et al. (2019). Uncertainty in satellite estimates of global mean sea-level changes, trend and acceleration. *Earth Syst. Sci. Data*, 11, 1189–1202. doi:10.5194/essd-11-1189-2019.

Argo (2020). Argo float data and metadata from Global Data Assembly Centre (Argo GDAC). SEANOE. doi:10.17882/42182

Arnault, S., Gourdeau, L., & Menard, Y. (1992). Comparison of the altimetric signal with in situ measurements in the tropical Atlantic Ocean. Deep Sea Research Part A. Oceanographic Research Papers, 39(3-4), 481-499. doi:10.1016/0198-0149(92)90084-7

Barron, C. N., Kara, A. B., & Jacobs, G. A. (2009). Objective estimates of westward Rossby wave and eddy propagation from sea surface height analyses. Journal of Geophysical Research Oceans, 114(C3), 496-510. doi:10.1029/2008JC005044

Bellomo, K., Angeloni, M., Corti, S., & von Hardenberg, J. (2021). Future climate change shaped by inter-model differences in Atlantic meridional overturning circulation response. Nature Communications, 12(1), 1-10. doi:10.1038/s41467-021-24015-w

Berger, W. H., Wefer, G., Richter, C., Lange, C. B., Giraudeau, J., Hermelin, O., & Party, S. S. (1998). 17. The Angola-Benguela upwelling system: Paleoceanographic synthesis of shipboard results from leg 1751. In Proceedings Ocean Drilling Program, Initial Reports (Vol. 175, pp. 505-531). doi:10.2973/odp.proc.ir.175.117.1998

Biastoch, A., Böning, C. W., Schwarzkopf, F. U. & Lutjeharms, J. R. E. (2009), Increase in Agulhas leakage due to poleward shift of Southern Hemisphere westerlies, Nature, 462(7272), 495-498. doi:10.1038/nature08519.

Broecker, W. S. (2003). Does the trigger for abrupt climate change reside in the ocean or in the atmosphere? Science, 300(5625), 1519-1522. doi:10.1126/science.1083797

Buckley, M. W., & Marshall, J. (2016). Observations, inferences, and mechanisms of the Atlantic Meridional Overturning Circulation: A review. Reviews of Geophysics, 54(1), 5-63. doi:10.1002/2015RG000493

Caínzos, V., Hernández-Guerra, A., McCarthy, G. D., McDonagh, E. L., Cubas Armas, M., & Pérez-Hernández, M. D. (2022). Thirty years of GOSHIP and WOCE data: Atlantic overturning of mass, heat, and freshwater transport. Geophysical Research Letters, 49(4), e2021GL096527. doi:10.1029/2021GL096527

Calado, L., Gangopadhyay, A., & Da Silveira, I. C. A. (2008). Feature-oriented regional modeling and simulations (FORMS) for the western South Atlantic: Southeastern Brazil region. Ocean Modelling, 25(1-2), 48-64. doi:10.1016/j.ocemod.2008.06.007

Chang, P., Zhang, R., Hazeleger, W., Wen, C., Wan, X., Ji, L., et al. (2008), Oceanic link between abrupt changes in the North Atlantic Ocean and the African monsoon, Nature Geoscience, 1(7), 444-448. doi:10.1038/ngeo218.

Chidichimo, M.P., Perez, R.C., Speich, S., Kersalé, M., Sprintall, J., Dong, S., et al. (2023), Energetic overturning flows, dynamic interocean exchanges, and ocean warming observed in the South Atlantic. Communications Earth Environment 4, 10. doi:.1038/s43247-022-00644-x

Collins, M., Sutherland, M., Bouwer L., Cheong, S. M., Frölicher, T., Jacot Des Combes, H., et al. (2019). Extremes, Abrupt Changes and Managing Risk. In Pörtner H. O., Roberts, D. C., Masson-Delmotte, V., Zhai, P., Tignor, M., Poloczanska, E., et al. (eds.), IPCC Special Report on the Ocean and Cryosphere in a Changing Climate. Cambridge University Press, Cambridge, UK and New York, NY, pp. 589-655. doi:10.1017/9781009157964.008.

Conway, T. M., Palter, J. B., & de Souza, G. F. (2018). Gulf Stream rings as a source of iron to the North Atlantic subtropical gyre. Nature Geoscience, 11(8), 594-598. doi:10.1038/s41561-018-0162-0

Da Silveira, I. C. A., Lima, J. A. M., Schmidt, A. C. K., Ceccopieri, W., Sartori, A., Francisco, C. P. F., & Fontes, R. F. C. (2008). Is the meander growth in the Brazil Current system off Southeast Brazil due to baroclinic instability? Dynamics of Atmospheres and Oceans, 45(3-4), 187-207. doi:10.1016/j.dynatmoce.2008.01.002

Desbruyères, D., Chafik, L. & Maze, G. (2021). A shift in the ocean circulation has warmed the subpolar North Atlantic Ocean since 2016. Commun Earth Environ 2, 48. doi:/10.1038/s43247-021-00120-y.

de Vries, P., & Weber, S. L. (2005). The Atlantic freshwater budget as a diagnostic for the existence of a stable shut down of the meridional overturning circulation. Geophysical Research Letters, 32(9), L09606. doi:10.1029/2004GL021450

Dong, S., Garzoli, S., Baringer, M., Meinen, C., & Goni, G. (2009). Interannual variations in the Atlantic meridional overturning circulation and its relationship with the net northward heat transport in the South Atlantic. Geophysical Research Letters, 36(20). doi: 10.1029/2009GL039356

Dong, S., Goni, G., & Bringas, F. (2015). Temporal variability of the South Atlantic meridional overturning circulation between 20 S and 35 S. Geophysical Research Letters, 42(18), 7655-7662. doi:10.1002/2015GL065603

Dong, S., Goni, G., Domingues, R., Bringas, F., Goes, M., Christophersen, J., & Baringer, M. (2021). Synergy of in situ and satellite ocean observations in determining meridional heat transport in the Atlantic Ocean. Journal of Geophysical Research: Oceans, 126(4). doi: 10.1029/2020JC017073

Durgadoo, J. V., Loveday, B. R., Reason, C. J., Penven, P. & Biastoch, A. (2013), Agulhas leakage predominantly responds to the Southern Hemisphere westerlies, Journal of Physical Oceanography, 43(10), 2113-2131. doi:10.1175/JPO-D-13-047.1.

Forget, G., Campin, J.-M., Heimbach, P., Hill, C. N., Ponte, R. M. & Wunsch, C. (2015). ECCO version 4: An integrated framework for non-linear inverse modeling and global ocean state estimation. Geoscientific Model Development, 8. 3071-3104. doi:10.5194/gmd-8-3071-2015

Fox-Kemper, B., Hewitt, H.T., Xiao, C., Aðalgeirsdóttir, G., Drijfhout, S.S., Edwards, T.L., et al. (2021). Ocean, Cryosphere and Sea Level Change. In Masson-Delmotte, V., P. Zhai, A. Pirani, S.L. Connors, C. Péan, S. Berger, et al. (eds.), Climate Change 2021: The Physical Science Basis. Contribution of Working Group I to the Sixth Assessment Report of the Intergovernmental Panel on Climate Change. Cambridge University Press, Cambridge, United Kingdom and New York, NY, USA, pp. 1211–1362. doi:10.1017/9781009157896.011

Frajka-Williams, E., Ansorge, I. J., Baehr, J., Bryden, H. L., Chidichimo, M. P., Cunningham, S. A., et al. (2019), Atlantic Meridional Overturning Circulation: Observed Transport and Variability, Frontiers in Marine Science, 6(260). doi:10.3389/fmars.2019.00260.

Garcia H.E., Boyer, T.P., Baranova, O.K., Locarnini, R.A., Mishonov, A.V., Grodsky, A., et al. (2019). World Ocean Atlas 2018: Product Documentation. A. Mishonov, Technical Editor. Retrieved from https://www.ncei.noaa.gov/sites/default/files/2020-04/woa18documentation.pdf

Garzoli, S. L., & Gordon, A. L. (1996). Origins and variability of the Benguela Current. Journal of Geophysical Research: Oceans, 101(C1), 897-906. doi:10.1029/95JC03221

Garzoli, S., Baringer, M., Dong, S., Perez, R. & Yao, Q. (2013), South Atlantic meridional fluxes, Deep Sea Res., Part I, 71, 21–32. doi:10.1016/ j.dsr.2012.09.003

Goes, M., Urban, N. M., Tonkonojenkov, R., Haran, M., Schmittner, A., & Keller, K. (2010). What is the skill of ocean tracers in reducing uncertainties about ocean diapycnal mixing and projections of the Atlantic Meridional Overturning Circulation? Journal of Geophysical Research: Oceans, 115(C12). doi:10.1029/2010JC006407

Goes, M., Wainer, I. & Signorelli, N. (2014). Investigation of the causes of historical changes in the subsurface salinity minimum of the South Atlantic. Journal of Geophysical Research-Oceans, 119(9), 5654-5675. doi:10.1002/2014JC009812.

Goes, M., Goni, G., & Dong, S. (2015). An optimal XBT-based monitoring system for the South Atlantic meridional overturning circulation at 34° S. Journal of Geophysical Research: Oceans, 120(1), 161-181. doi:10.1002/2014JC010202

Goes, M., Christophersen, J., Dong, S., Goni, G., & Baringer, M. O. (2018). An updated estimate of salinity for the Atlantic ocean sector using temperature–salinity relationships. Journal of Atmospheric and Oceanic Technology, 35(9), 1771-1784. doi:10.1175/JTECH-D-18-0029.1

Goes, M., Cirano, M., Mata, M. M., & Majumder, S. (2019). Long-Term Monitoring of the Brazil Current Transport at 22° S From XBT and Altimetry Data: Seasonal, Interannual, and Extreme Variability. Journal of Geophysical Research: Oceans, 124(6), 3645-3663. doi:10.1029/2018JC014809

Goes, M., Murphy, L. N. & Clement, A.C. (2019b). The stability of the AMOC during Heinrich events is not dependent on the AMOC strength in an Intermediate Complexity Earth System model ensemble. Paleoceanography and Paleoclimatology, 34(8),1359-1374. doi:10.1029/2019PA003580.

Goes, M., Goni, G., Dong, S., Boyer, T., & Baringer, M. (2020). The complementary value of XBT and Argo observations to monitor ocean boundary currents and meridional heat and volume transports: A case study in the Atlantic Ocean. Journal of Atmospheric and Oceanic Technology, 37(12), 2267-2282. doi:10.1175/JTECH-D-20-0027.1

Hernández-Guerra, A., Talley, L. D., Pelegrí, J. L., Vélez-Belchí, P., Baringer, M. O., Macdonald, A. M., & McDonagh, E. L. (2019). The upper, deep, abyssal and overturning circulation in the Atlantic Ocean at 30 S in 2003 and 2011. Progress in Oceanography, 176, 102136. doi:10.1016/j.pocean.2019.102136

Herrford, J., Brandt, P., Kanzow, T., Hummels, R., Araujo, M., & Durgadoo, J. V. (2021). Seasonal variability of the Atlantic Meridional Overturning Circulation at 11 S inferred from bottom pressure measurements. Ocean Science, 17(1), 265-284. doi:10.5194/os-17-265-2021

Hersbach, H, Bell, B, Berrisford, P, et al. (2020). The ERA5 global reanalysis, Q J R Meteorol Soc., 146, 1999– 2049. doi:10.1002/qj.3803

Hummels, R., Brandt, P., Dengler, M., Fischer, J., Araujo, M., Veleda, D. & Durgadoo, J. V. (2015), Interannual to decadal changes in the western boundary circulation in the Atlantic at 11°S, Geophysical Research Letters, 42(18), 7615-7622. doi:10.1002/2015GL065254.

Johns, W. E., Baringer, M. O., Beal, L. M., Cunningham, S. A., Kanzow, T., Bryden, H. L., ... & Curry, R. (2011). Continuous, array-based estimates of Atlantic Ocean heat transport at 26.5 N. Journal of Climate, 24(10), 2429-2449. doi:10.1175/2010JCLI3997.1

Kersalé, M., Meinen, C. S., Perez, R. C., Le Henaff, M., Valla, D., Lamont, T., et al. (2020). Highly Variable Upper and Abyssal Overturning Cells in the South Atlantic, Science Advances, 6(32). doi:10.1126/sciadv.aba7573.

Koltermann, K.P., Gouretski, V.V. & Jancke, K. (2011). Hydrographic Atlas of the World Ocean Circulation Experiment (WOCE). Volume 3: Atlantic Ocean (eds. M. Sparrow, P. Chapman and J. Gould). International WOCE Project Office, Southampton, UK, ISBN 090417557X.

Koseki, S., Giordani, H., & Goubanova, K. (2019). Frontogenesis of the Angola–Benguela frontal zone. Ocean Science, 15(1), 83-96. doi:10.5194/os-15-83-2019

Lee, J.-Y., Marotzke, J., Bala, G., Cao, L., Corti, S., Dunne, J.P., et al. (2021). Future Global Climate: Scenario-Based Projections and Near- Term Information. In Masson-Delmotte, V., Zhai, P., Pirani, A., Connors, S.L., Péan, C., Berger, S., et al. (eds.), Climate Change 2021: The Physical Science Basis. Contribution of Working Group I to the Sixth Assessment Report of the Intergovernmental Panel on Climate Change. Cambridge University Press, Cambridge, United Kingdom and New York, NY, USA, pp. 553–672. doi:10.1017/9781009157896.006

Lima, M. O., Cirano, M., Mata, M. M., Goes, M., Goni, G., & Baringer, M. (2016). An assessment of the Brazil Current baroclinic structure and variability near 22° S in Distinct Ocean Forecasting and Analysis Systems. Ocean Dynamics, 66(6), 893-916. doi:10.1007/s10236-016-0959-6

Little, C. M., Piecuch, C. G., & Ponte, R. M. (2017), On the relationship between the meridional overturning circulation, alongshore wind stress, and United States East Coast sea level in the Community Earth System Model Large Ensemble. J. Geophys. Res., 112, 4554–4568. doi:10.1002/2017JC012713

Liu, M., & Tanhua, T. (2021). Water masses in the Atlantic Ocean: characteristics and distributions. Ocean Science, 17(2), 463-486. doi:10.5194/os-17-463-2021

Locarnini, M. M., Mishonov, A. V., Baranova, O. K., Boyer, T. P., Zweng, M. M., Garcia, H. E., et al. (2018). World ocean atlas 2018, volume 1: Temperature. A. Mishonov, Technical Editor.

NOAA Atlas NESDIS 81, 52pp. Retrieved from https://www.ncei.noaa.gov/sites/default/files/2020-04/woa18_vol1.pdf

Lopez, H., Dong, S., Lee, S.-K., & Goni, G. (2016). Decadal Modulations of Interhemispheric Global Atmospheric Circulations and Monsoons by the South Atlantic Meridional Overturning Circulation. J. Clim., 29(5), 1831-1851. doi:10.1175/JCLI-D-15-0491.1

Majumder, S., & Schmid, C. (2018). A study of the variability in the Benguela Current volume transport, Ocean Sci., 14, 273–283. doi:10.5194/os-14-273-2018.

Marcello, F., Tonelli, M., Ferrero, B., & Wainer, I. (2023). Projected Atlantic overturning slow-down is to be compensated by a strengthened South Atlantic subtropical gyre. Commun Earth Environ. 4, 92. doi:10.1038/s43247-023-00750-4

Mata, M. M., Cirano, M., Caspel, M. R. V., Fonteles, C. S., Gõni, G., & Baringer, M. (2012). Observations of Brazil Current baroclinic transport near 22 S: variability from the AX97 XBT transect. Exchanges, 58, 5-10.

McCarthy, G. D., Brown, P. J., Flagg, C. N., Goni, G., Houpert, L., Hughes, C. W., et al. (2020), Sustainable Observations of the AMOC: Methodology and Technology, Reviews of Geophysics, 58(1). doi:10.1029/2019RG000654.

Meinen, C. S., Speich, S., Piola, A. R., Ansorge, I., Campos, E., Kersalé, M., et al. (2018). Meridional overturning circulation transport variability at 34.5 S during 2009–2017: Baroclinic and barotropic flows and the dueling influence of the boundaries. Geophysical Research Letters, 45, 4180-4188. doi:10.1029/2018GL077408

Pereira, J., Gabioux, M., Almeida, M. M., Cirano, M., Paiva, A. M., & Aguiar, A. L. (2014). The bifurcation of the western boundary current system of the South Atlantic Ocean. Brazilian Journal of Geophysics, 32(2), 241-257. doi:10.22564/rbgf.v32i2.456

Pita, I. I., Cirano, M., & Mata, M. M. (2020). An assessment of Brazil Current surface velocity and associated transport near 22° S: XBT and altimetry data. Regional Studies in Marine Science, 35, 101197. doi:10.1016/j.rsma.2020.101197

Polito, P. S., & Liu, W. T. (2003). Global characterization of Rossby waves at several spectral bands. Journal of Geophysical Research: Oceans, 108(C1). doi:10.1029/2000JC000607

Pujol, M. I., Faugère, Y., Taburet, G., Dupuy, S., Pelloquin, C., Ablain, M., & Picot, N. (2016). DUACS DT2014: the new multi-mission altimeter data set reprocessed over 20 years. Ocean Science, 12(5), 1067-1090. doi:10.5194/os-12-1067-2016

Rahmstorf, S. (1996). On the freshwater forcing and transport of the Atlantic thermohaline circulation. Climate Dynamics, 12(12), 799–811. doi:10.1007/s003820050144

Reid, J.L., 1989. On the total geostrophic circulation of the South Atlantic Ocean: Flow patterns, tracers, and transports. Prog. Oceanogr. 23, 149–244. doi:10.1016/0079-6611(89)90001-3

Rhein, M. (2019). Taking a close look at ocean circulation. Science, 363(6426), 456-457. doi:10.1126/science.aaw3111

Roemmich, D. & Gilson, J. (2009) The 2004-2008 mean and annual cycle of temperature, salinity, and steric height in the global ocean from the Argo Program. Progress in Oceanography, 82, 81-100. doi:10.1016/j.pocean.2009.03.004

Roemmich, D., Johnson, G.C., Riser, S., Davis, R., Gilson, J., Owens, W.B., Garzoli, S.L., Schmid, C., & Ignaszewski, M. (2009). The Argo Program: Observing the global ocean with profiling floats. Oceanography, 22(2), 34–43. doi:10.5670/oceanog.2009.36.

Stommel, H. (1961), Thermohaline Convection with Two Stable Regimes of Flow, Tellus, 13(2), 224-230. doi:10.1111/j.2153-3490.1961.tb00079.x.

Stramma, L., & England, M. (1999). On the water masses and mean circulation of the South Atlantic Ocean. Journal of Geophysical Research: Oceans, 104(C9), 20863-20883. doi:10.1029/1999JC900139

Stramma, L., Kieke, D., Rhein, M., Schott, F., Yashayaev, I., & Koltermann, K. P. (2004). Deep water changes at the western boundary of the subpolar North Atlantic during 1996 to 2001, Deep Sea Res., 51, 1033–1056. doi:10.1016/j.dsr.2004.04.001

Strub, P. T., James, C., Combes, V., Matano, R. P., Piola, A. R., Palma, E. D., et al. (2015). Altimeter-derived seasonal circulation on the southwest Atlantic shelf: 27°–43° S. Journal of Geophysical Research: Oceans, 120(5), 3391-3418. doi:10.1002/2015JC010769.

Talley, L. D. (2011). Descriptive physical oceanography: an introduction. Academic press. 6th ed, pp. 560.

Todd, R. E., Chavez, F. P., Clayton, S., Cravatte, S., Goes, M., Graco, M., et al. (2019). Global perspectives on observing ocean boundary current systems. Frontiers in Marine Science, 6(423). doi: 10.3389/fmars.2019.00423.

Veitch, J. A., Florenchie, P., & Shillington, F. A. (2006). Seasonal and interannual fluctuations of the Angola–Benguela Frontal Zone (ABFZ) using 4.5 km resolution satellite imagery from 1982 to 1999. International Journal of Remote Sensing, 27(05), 987-998. doi:10.1080/01431160500127914

Volkov, D. L., Baringer, M., Smeed, D., Johns, W., & Landerer, F. W. (2019). Teleconnection between the Atlantic meridional overturning circulation and sea level in the Mediterranean Sea. Journal of climate, 32(3), 935-955. doi:10.1175/JCLI-D-18-0474.1

Weijer, W., Cheng, W., Drijfhout, S. S., Fedorov, A. V., Hu, A., Jackson, L. C., et al. (2019). Stability of the Atlantic meridional overturning circulation: A review and synthesis. Journal of Geophysical Research: Oceans, 124(8), 5336–5375. doi:10.1029/2019JC015083

Zweng, M. M., Seidov, D., Boyer, T. P., Locarnini, M., Garcia, H. E., Mishonov, A. V., et al. (2019). World ocean atlas 2018, volume 2: Salinity. A. Mishonov, Technical Editor, NOAA Atlas NESDIS 82, 50pp. Retrieved from https://www.ncei.noaa.gov/sites/default/files/2022-06/woa18_vol2.pdf

AGU PUBLICATIONS

Journal of Geophysical Research

Supporting Information for

An ARGO and XBT observing system for the Atlantic Meridional Overturning Circulation and Meridional Heat Transport (AXMOC) at 22.5ºS

I. Pita[1,2,3], M. Goes[2,3], D. L. Volkov[2,3], S. Dong[3], G. Goni[3] and M. Cirano[4]

[1]Rosenstiel School, University of Miami, Miami, Fl, United States of America.

[2]Cooperative Institute for Marine and Atmospheric Studies, University of Miami, Miami, Fl, United States of America.

[3]Atlantic Ocean and Metrorological Laboratory, NOAA, United States of America.

[4]Department of Meteorology, Institude of Geosciences, Federal university of Rio de Janeiro (UDRJ), Brazil

Corresponding author: Ivenis Pita (ivenis.pita@noaa.gov)

Contents of this file

Text S1 to S4
Figures S1 to S4

Introduction

The supplementary material could be divided in 2 parts. The figure S1 is an extension of Figure 8 analysis, where WOCE data is compared to AXMOC data for a similar period, and the Figures S2-S4 compares the AMOC and MHT at 22.5°S between AXMOC and other databases (synthetic estimations and model reanalysis).

Text S1.

Figure S1 is an extension of the Figure 8 analysis. Here, WOCE temperature, salinity, dissolved oxygen and meridional velocity sections at 24°S are compared to temperature, salinity and meridional velocity sections at 22.5°S for March 2018. Figure S1 corroborates with the conclusions drawn from Figure 8.

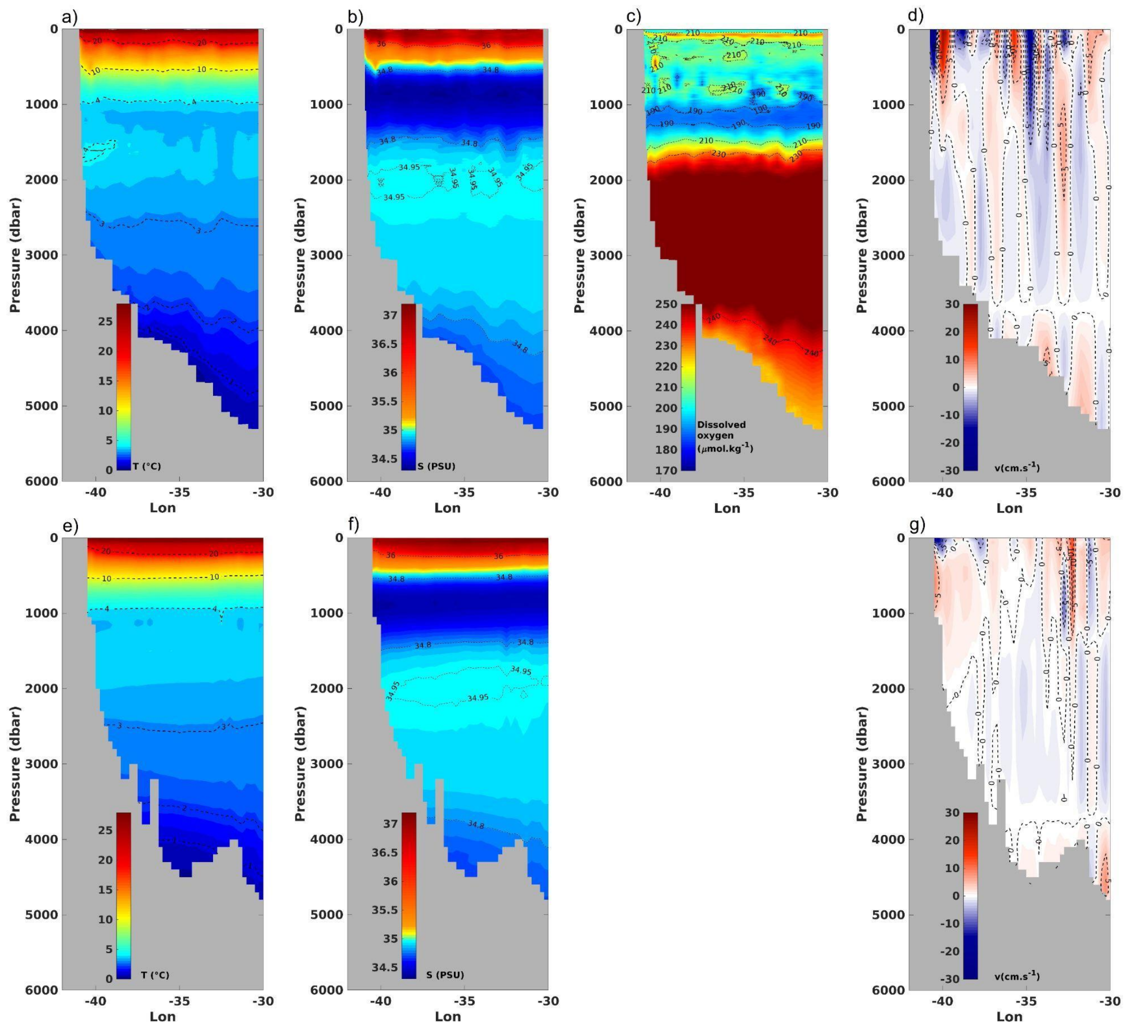

Figure S1. Ocean tracers and velocity section focused on Western boundary for March 2018 at 24 and 22.5°S. A-d (e-h) panels represent WOCE (AXMOC) dataset. Temperature (T), salinity (S), dissolved oxygen and velocity (v) are shown between Western boundary and 30°W.

Text S2-S4.

AXMOC data are compared to two synthetic observational time series from Dong et al. (2021) at 20 and 25°S and to a model reanalysis (ECCO4) at 22.5°S (Figures S2-S4). The Ekman contribution is similar among all products because consecutive versions of ECMWF products are used for Ekman contribution to AMOC transport (ERA Interim and ERA5 - Figure S2). Larger spread in geostrophic AMOC contribution is responsible for the differences in total AMOC time series among products. Dong et al. (2015) reported a decrease in the AMOC, a decrease in the Ekman transport and an increase in Geostrophic transport toward the Equator. This pattern is also observed in this study when comparing the transects from Dong et al. (2021) at 25°S the AXMOC transect at 22.5°S, and Dong et al. (2021) at 20°S for the total AMOC (19.30±2.20 Sv, 17.21±2.72 Sv and 16.45±2.13 Sv, respectively) and from Dong et al. (2021) at 25°S, ECCO4 at 22.75°S, AXMOC transect at 22.5°S and Dong et al. (2021) at 20°S for the Ekman (-3.70±1.42 Sv, -5.01±1.38 Sv, -5.41±1.49 Sv and -6.26±1.66 Sv, respectively) transports (Figure S2 and Table 1). Overall, the meridional dependence is also observed when considering both the Ekman and the Geostrophic components. The ECCO4 product has a weaker AMOC time mean transport (14.11±2.55 Sv) than the other products (>16.45 Sv). This is because of a smaller contribution of Geostrophic transport (Figure S2 and Table 1). The total AXMOC time mean AMOC strength is 17.21±2.2.72 Sv, while in Dong et al., (2021) data the AMOC strength is 16.45±2.13 Sv and 19.30±2.20 Sv at 20 and 25°S, respectively. Therefore, the AXMOC data has higher AMOC variability than the other products. This result highlights the importance of in situ data, especially at the Western boundary, which samples the highly variable BC. Table 1 also describes the mean MHT and their variability (using the standard deviation metric as a proxy). The Ekman contribution to the MHT follows the same latitudinal dependence as the AMOC, whereas the MHT values decrease towards equator (intensification of poleward transport): -0.33±0.13 PW, -0.39±0.10 PW, -0.42±0.10 PW, -0.58±0.14 PW for Dong et al., (2021) (25°S), ECCO4 (22.75°S), AXMOC (22.5°S) and Dong et al., (2021) (20°S), respectively. The MHT Geostrophic component is 1.21±0.16 for the AXMOC product, 1.20±0.09 PW and 1.01±0.12 PW for Dong et al., (2021) at 20 and 25°S, respectively, and the weaker MHT is represented by ECCO4 reanalysis (0.87±0.10 PW). The less intense total MHT is also observed in ECCO4 data (0.48±0.16 PW), followed by Dong et al., (2021) at 20°S and 25°S (0.62±0.17 PW and 0.68±0.17 PW, respectively) and AXMOC (0.79±0.18 PW).

The monthly climatological averages of the in situ based AMOC and MHT show a multiple peak pattern, with intense transports in May and December, and a negative value in September, considering the period between 2007 and end of 2019 (Figure S3). The same pattern is observed for Dong et al., (2021) data in the period analyzed but for different peak months, with positive peaks in April and December (May and December) and a negative peak in August (October) for 20°S (25°S). For the total period analyzed in Dong et al., (2021), from 1994 to 2020, the MHT monthly climatology has a positive peak in April and a negative peak in August. The ECCO4 monthly climatological averages show a positive peak in May and two negative peaks in February and October, considering the period between 2007 and 2017. The Ekman transport contributes positively for the AMOC from December to June and negatively from July to November in every data analyzed. The Ekman component influences the total AMOC seasonality in the second semester by weakening the total transport for AXMOC and Dong et al., (2021) data. The AXMOC AMOC seasonal component presents a greater correlation to Dong et al. (2021) at 25°S than at 20°S (r= 0.80 and r=0.46, respectively).

The auxiliary data also agrees with AXMOC in the interannual signal (Figure S4). Similar to what is observed in the AXMOC dataset, most of the variability of the AMOC is explained by the geostrophic component in interannual frequencies on the synthetic observations and ECCO4 datasets. Synthetic observations presented a significant correlation between the total and geostrophic AMOC components on the interannual signal, however, the correlation found at 25°S is similar to what it is observed for the AXMOC data (r=0.93), while the correlation at 20°S is slightly lower (r=0.65). Therefore, on both seasonal and interannual time series, the AXMOC dataset had similar correlations to the ones observed at 25°S by Dong et al., (2021) synthetic observations.

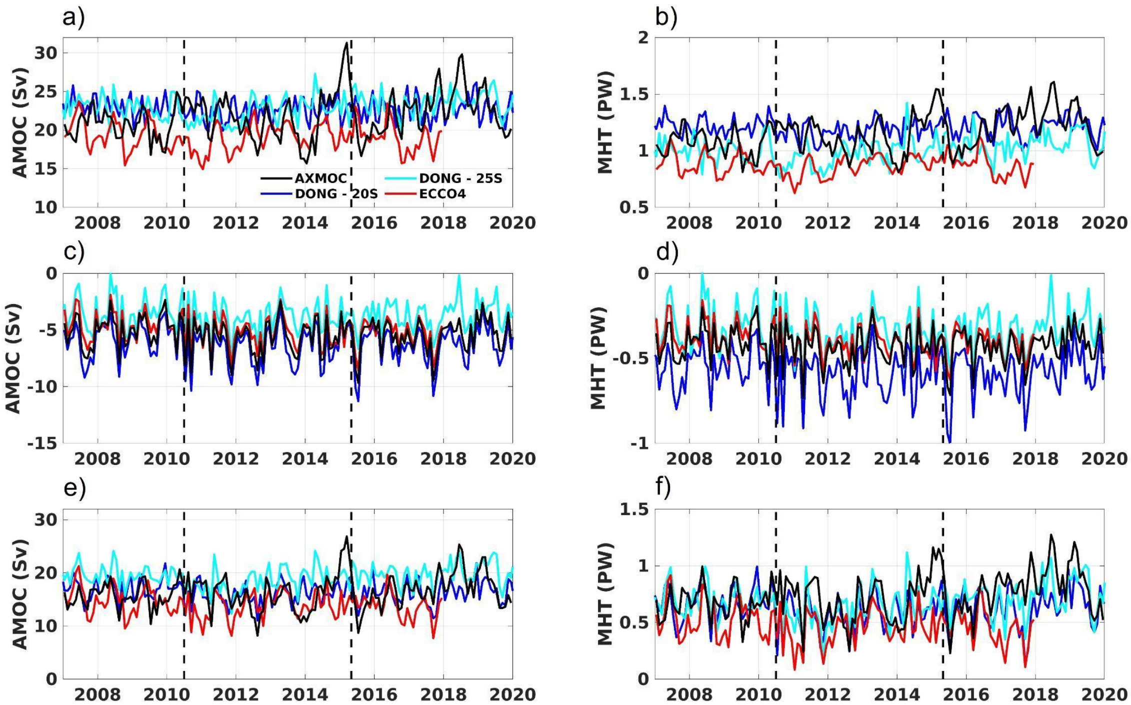

Figure S2. AMOC (a, c and e) and MHT (b, d and f) time series are divided into Geostrophic (a and b), Ekman (c and d) and total components (e and f). Black line represents AXMOC data. Synthetic data from Dong et al., (2021) are shown in blue (20°S) and cyan (25°S) lines. ECCO4 data is represented by the red line. Black dashed lines indicate dates of 06/2010 and 04/2015.

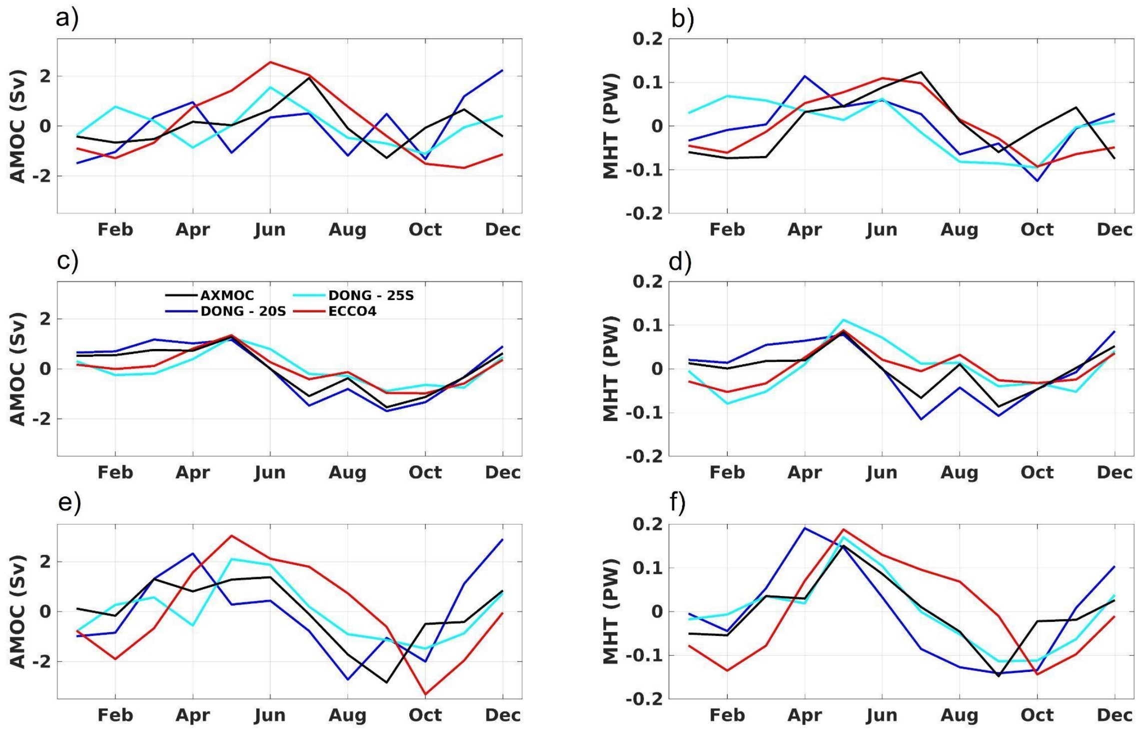

Figure S3. Same as Figure S2 but for the seasonal cycle. The annual mean was removed for better visualization.

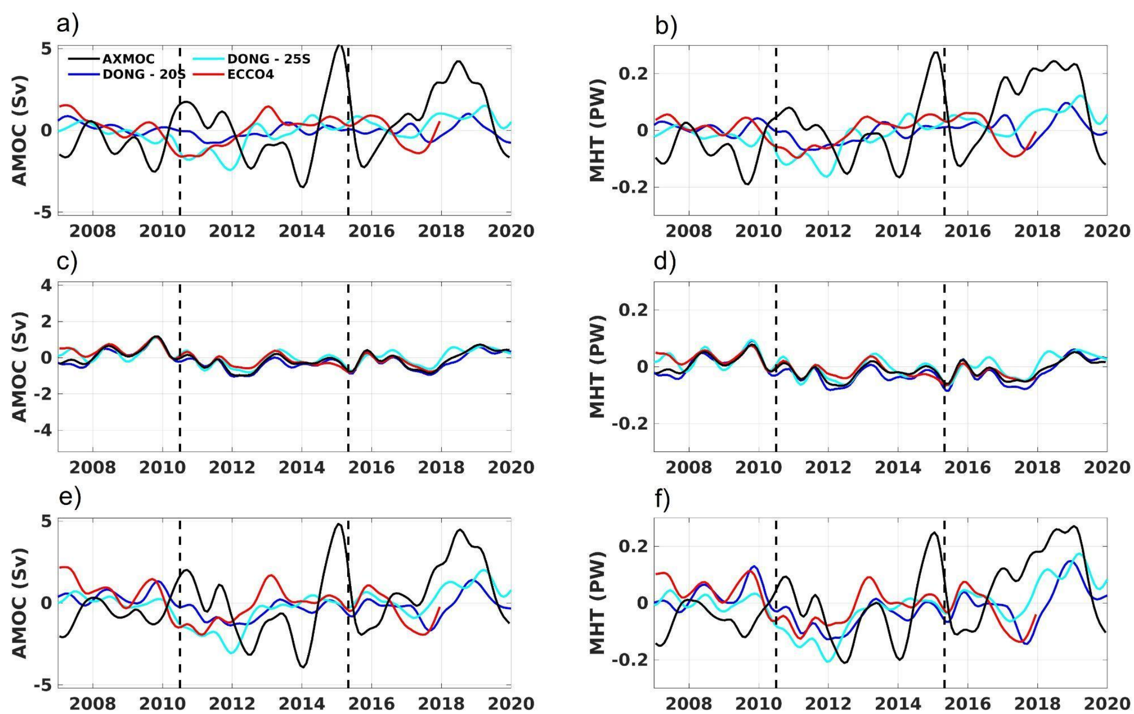

Figure S4. Same as Figure S2, but for the interannual component.